Optimising thermal expansion in 3D printed mortars

Diogo Alexandre Rodrigues dos Santos
M. Sc. In Engineering Physics
Department of Physics and Astronomy
2023

Supervisor
João Horta Belo, Junior Researcher, Faculty of Sciences of University of Porto

Co-supervisor
Ana Sofia Guimarães, Associate Professor, Faculty of Engeneering of University of Porto


U.PORTO
FACULDADE DE CIÊNCIAS
UNIVERSIDADE DO PORTO

Acknowledgements

First of all, I would like to thank the group at the Department of Civil Engineering (DEC) of University of Porto and IFIMUP, the Institute of Physics for Advanced Materials, Nanotechnology and Photonics of the University of Porto for providing me with the tools and support necessary to finish this project.

To Dr. João Horta Belo, for the amazing constant support, for everything he taught me, and who was always there for guidance and motivation. Without him, this work would have not been possible and I am immensely grateful.

To Prof. Ana Guimarães, for the availability, and for always providing valuable knowledge and insight.

To Dr. Aleksey Yaremchenko, for conducting the dilatometry measurements, and to professor John Evans for providing the ZrW_2O_8 powder.

To Rafael Almeida for all the advice and help with the strain gauge measurements, and to Sofia Pessoa and Manuel Jesus for providing help with the mortars and 3D printing information.

To my pillar Filipa, who accompanied me along this journey, and provided all the support I needed to finish this chapter in my live.

To my parents, who have always supported me, even from afar, and to whom I will always be grateful.

Finally, to all my friends, for being my companions during the good and bad moments.

UNIVERSITY OF PORTO

Abstract

Faculty of Sciences of University of Porto
Department of Physics and Astronomy

M. Sc. Engineering Physics

Optimising thermal expansion in 3D printed mortars

by Diogo SANTOS

As opposed to the conventional positive thermal expansion materials (PTE), some materials expand upon cooling, exhibiting a negative thermal expansion (NTE). Their technological potential relies on their combination (as fillers) with a PTE material to produce composites with near zero thermal expansion (ZTE), which finds practical application in large telescopes, micro-devices, or cookware. This concept needs to be introduced in the construction sector, as microcracks induced by natural cooling and heating cycles are a concern for long term infrastructure integrity. By combining 3D printed structures, which is an emerging technology in the sector, this work aims to provide a preliminary approach and introduce NTE materials (as fillers) in mortar mixes (aimed for 3D printing) to tailor their coefficient of thermal expansion (CTE) and produce a ZTE composite. In this work, for the fillers, we focused on NTE LaFeSi based materials and ZrW_2O_8, and a silica powder as a low cost, low PTE alternative. The composition and morphology of the fillers and mortars were analysed using various characterisation methods. We utilised analytical models, Finite Element Analysis (FEA), and the Taguchi method to investigate the impact of different factors on the compensated mortar's CTE. Using the strain gauge method, we measured the CTE of 3D printed, non-compensated mortar (33 ppm/K), and reduced CTE values by introducing the NTE fillers. However, the CTEs of the silica compensated mortars were higher, and dilatometry measurements yielded CTEs around 6.5 ppm/K for all samples. The fabrication method and curing conditions of the mortars could be behind these discrepancies. Nonetheless, this preliminary study and the methodologies therein discussed proved useful for future thermal expansion measurements and ZTE applications on mortars.

Keywords: Zero thermal expansion, mortar, composite, 3D printing

UNIVERSIDADE DO PORTO

Resumo

Faculdade de Ciências da Universidade do Porto
Departamento de Física e Astronomia

Mestrado em Engenharia Física

Otimização da expansão térmica de argamassas para impressão em 3D

por Diogo SANTOS

Ao contrário dos materiais convencionais de expansão térmica positiva (PTE), alguns materiais expandem após serem arrefecidos, e exibem uma expansão térmica negativa (NTE). O seu potencial tecnológico assenta na sua combinação (como compensadores) com um material PTE para produzir compósitos com expansão térmica quase nula (ZTE), que são usados em microdispositivos ou utensílios de cozinha. Este conceito tem de ser introduzido no setor da construção, uma vez que as microfissuras induzidas por ciclos térmicos são uma preocupação para a integridade das infraestruturas a longo prazo. Ao combinar estruturas impressas em 3D (uma tecnologia emergente no sector), pretende-se fornecer uma abordagem preliminar e introduzir materiais NTE em argamassas (para impressão 3D) para reduzir o seu coeficiente de expansão térmica (CTE). Neste trabalho, como compensadores, concentrou-se em materiais NTE à base de LaFeSi e ZrW_2O_8, e um pó de sílica como alternativa de baixo custo e baixo PTE. A composição e a morfologia das argamassas foram analisadas utilizando vários métodos de caraterização. Utilizou-se modelos analíticos, análise de elementos finitos (FEA) e o método Taguchi para investigar o impacto de diferentes factores no CTE das argamassa. Utilizando o método do extensómetro, mediu-se o CTE da argamassa não compensada, impressa em 3D (33 ppm/K), e reduziu-se os valores de CTE ao introduzir os compensadores NTE. No entanto, os CTE das argamassas compensadas com sílica foram mais elevados, e as medições de dilatometria deram CTEs à volta de 6.5 ppm/K para todas as amostras. O método de fabrico e as condições de cura podem estar na origem destas discrepâncias. No entanto, este estudo preliminar e as metodologias nele discutidas revelaram-se úteis para futuras medições de expansão térmica e aplicações ZTE em argamassas.

Palavras-chave: Expansão térmica nula, argamassa, compósito, impressão 3D

Contents

Acknowledgements i

Abstract iii

Resumo v

Contents vii

List of Figures xi

List of Tables xiii

Symbols xv

Glossary xvii

1 Motivation 1
- 1.1 Infrastructure thermal cracking . . . 1
- 1.2 Near zero thermal expansion materials and applications . . . 2
- 1.3 Additive manufacturing . . . 3

2 Theory and literature review 5
- 2.1 Mortar composition and properties . . . 5
  - 2.1.1 Mortar composition . . . 5
  - 2.1.2 Cement hydration . . . 6
  - 2.1.3 Curing and other considerations . . . 7
- 2.2 Negative thermal expansion mechanisms . . . 8
  - 2.2.1 Thermal expansion . . . 8
  - 2.2.2 Transverse vibrations . . . 10
  - 2.2.3 Rigid unit modes (RUMs) . . . 11
  - 2.2.4 Phase transitions . . . 11
  - 2.2.5 Size-confinement NTE . . . 12
- 2.3 Thermal expansion compensators . . . 12
  - 2.3.1 White micro silica powder . . . 13
  - 2.3.2 LaFeSi-based compounds . . . 14
  - 2.3.3 Zirconium Tungstate . . . 15
  - 2.3.4 Fine oxide ceramic powder . . . 15

2.3.5 Price comparison . . . 16
2.4 Predictive models for the coefficient of thermal expansion of composites . . 17
2.4.1 Analytical models . . . 17
2.4.2 Finite element analysis (FEA) . . . 18

3 Experimental Section **19**
3.1 FEA of the mortar's thermal expansion . . . 19
3.1.1 Modelling setup . . . 19
3.1.2 Materials used and their properties . . . 21
3.1.3 Composite geometry and filler distribution . . . 21
3.1.4 Model analysis . . . 23
3.2 Taguchi method implementation . . . 23
3.3 Mortar fabrication . . . 25
3.4 X-ray diffraction . . . 26
3.5 Scanning electron microscopy . . . 29
3.6 Ball Milling . . . 31
3.7 Strain Gauge sensor . . . 32
3.8 Thermal expansion measurements . . . 35
3.9 Dilatometry . . . 37

4 Results and discussion **39**
4.1 Material composition and morphology . . . 39
4.1.1 White micro silica powder . . . 39
4.1.2 Non-compensated mortar powder . . . 40
4.1.3 Hydrated non-compensated mortar . . . 42
4.1.4 Silica compensated mortar . . . 43
4.1.5 LaFeSi compensated mortar . . . 44
4.2 Finite element analysis . . . 46
4.2.1 Analytical model predictions and FEA simulations . . . 46
4.2.2 Taguchi analysis on the mortar's CTE . . . 48
4.2.3 Stress analysis . . . 49
4.3 Thermal expansion measurements . . . 51
4.3.1 Initial 3D printed mortar sample . . . 51
4.3.2 Micro silica compensated mortars . . . 52
4.3.3 LaFeSi compensated mortars . . . 54
4.3.4 Zirconium Tungstate compensated mortars . . . 55
4.3.5 Manually produced (MP) mortars . . . 56
4.3.6 Dilatometry measurements . . . 57
4.3.7 Discussion . . . 59

5 Conclusion and future work **63**

A Mortar fabrication process and samples **67**
A.1 Fabrication process . . . 67
A.2 Fillers and manually produced samples . . . 68

B Thermal expansion complementary calculations **71**

C EDS data examples **75**

D Thermal expansion measurements additional information **77**
D.1 Temperature lag between thermocouple readings and actual sample temperature 77
D.2 Dilatometry additional data 79

Bibliography **81**

List of Figures

1.1 Overall concept of the work . . . 3
1.2 Example of 3D printed mortar . . . 4

2.1 Mortar microstructure and ITZ . . . 8
2.2 2D comparison between the effects of a temperature increase on a PTE and NTE material . . . 9
2.3 Typical anharmonic potential energy as a function of interatomic distance . 10
2.4 Classification of negative thermal expansion materials and mechanisms . . 11
2.5 2D representation of different vibrational modes and Rigid unit modes . . . 12
2.6 CTE values of typical NTE and PTE materials . . . 13
2.7 LaFeSi graphical data regarding its CTE as a function of temperature and ball milling times . . . 14
2.8 ZrW_2O_8 structure . . . 15
2.9 Representative volume elements (RVEs) with different mesh element sizes . 18

3.1 2D and 3D COMSOL Multiphysics models comparison . . . 20
3.2 2D composite geometries with different number of particles and same filler volume fraction . . . 22
3.3 2D composite geometries with different filler volume fractions and same number of particles . . . 23
3.4 Factors and levels used and the corresponding implemented orthogonal array in the Taguchi design . . . 24
3.5 Moulds used in the mortar fabrication . . . 25
3.6 Schematic representation of x-ray diffraction . . . 27
3.7 Identification of the composition of a composite by comparing the individual "fingerprints" of known materials . . . 28
3.8 SEM instrumentation and working principles . . . 29
3.9 Different interactions between the incident electron beam and the sample . 30
3.10 Ball Milling Schematic . . . 31
3.11 Comparison of the as prepared LaFeSi powder and the final 180 min grinded powder . . . 32
3.12 Strain gauge schematic . . . 33
3.13 Wheatstone bridge schematic diagram . . . 34
3.14 Schematic of a closed cycle cryocooler . . . 35
3.15 Individual components of a cryostat . . . 36
3.16 Experimental setup for the thermal expansion measurements . . . 37
3.17 Simple schematic of a dilatometer . . . 38

4.1 SEM micrograph of the silica powder and size distribution . . . 40
4.2 SEM micrographs of the mortar powder . . . 41
4.3 XRD diffractogram data on the mortar powder and hydrated mortar . . . 41
4.4 SEM micrographs of the hydrated mortar . . . 42
4.5 SEM micrograph of the silica compensated mortar . . . 43
4.6 SEM micrograph of the non-grinded superficial layer of the LaFeSi compensated mortar and size distribution . . . 45
4.7 SEM micrograph of the LaFeSi compensated mortar . . . 45
4.8 Compensated mortars analytical and numerical model comparison . . . 47
4.9 FEA comparison of different compensated mortar's CTE for different filler volume fractions . . . 48
4.10 Comparison between the multivariate least square fitting of the mortar's CTE and the measured CTE, and correlation matrix . . . 49
4.11 Stress comparison for different mortar compositions . . . 49
4.12 Stress comparison for different amount of particle inclusions in the 15% LaFeSi compensated mortar . . . 50
4.13 Stress comparison for different filler volume fractions in the LaFeSi compensated mortar with 27 particle inclusions . . . 50
4.14 Representation and comparison between the slope and extremities methods 52
4.15 Strain versus temperature measurements of the original 3D printed mortar 53
4.16 Strain versus temperature measurements of the SiO_2 compensated mortars for different heating rates . . . 54
4.17 Strain versus temperature measurements of the LaFeSi compensated mortars for different heating rates . . . 55
4.18 Strain versus temperature measurements of the ZrW_2O_8 compensated mortars for different heating rates and filler volume fractions . . . 56
4.19 Strain versus temperature measurements of the MP mortars for different heating rates and strain gauges applied . . . 57
4.20 Strain versus temperature measurements using the dilatometry method . . . 58
4.21 Summary of the thermal expansion measurements of all samples . . . 60

A.1 Mortar fabrication process . . . 67
A.2 Fillers used in the work . . . 68
A.3 Samples used in the work . . . 68
A.4 Samples used in the work and brittle produced mortar . . . 68
A.5 SEM micrographs showing a comparison between the superficial layer and the bulk mortar . . . 69

B.1 Implemented Wheatstone bridge circuit . . . 73

C.1 EDS of some compensated mortars . . . 75

D.1 Temperature lag between thermocouple readings and actual sample temperature . . . 78
D.2 Dilatometric CTE measurements for each sample . . . 79

List of Tables

2.1 Filler and cement prices, and material cost to build a wall 16

3.1 Materials used and their properties 21

Symbols

θ	Angle of diffraction
A	Area
$< d >$	Average particle size
K	Bulk modulus
α_v	Coefficient of volumetric thermal expansion
T_C	Curie temperature
ρ	Density
I	Electrical current
V	Electrical potential
n	Integer number of the wavelength
K_α	K-alpha x-ray emission
K_β	K-beta x-ray emission
a	Lattice parameter
d	Lattice planes separation distance
L	Length
m	Mass
n	Number of inclusions
σ	Particle size standard deviation
π	Pi
μ	Poisson's ratio
P	Pressure

r	Radius
R	Resistance
ρ_m	Resistivity
G	Shear modulus
ϵ	Strain
T	Temperature
C	Vector with initial particle coordinates
V	Volume
ϕ	Volume fraction
λ	Wavelength
E	Young's modulus

Glossary

BSE	Backscattered Electrons
BM	Ball Milling
CH	Calcium Hydroxide
C-S-H	Calcium Silicate Hydrate
CNN	Cement Chemist Notation
CTE	Coefficient of linear Thermal Expansion
C2S	Dicalcium Silicate
EDS	Energy Dispersive x-ray Spectroscopy
FEA	Finite Element Analysis
GF	Gauge Factor
ITZ	Interfacial Transition Zone
LVDT	Linear Variable Differential Transformer
MP	Manually produced
MBT	Model Builder Tree
NTE	Negative Thermal Expansion
ppm	Parts Per Million
PTE	Positive Thermal Expansion
PE	Primary Electrons
PID	Proportional-Integral-Derivative
RVE	Representative Volume Element
RUM	Rigid Unit Modes

ROM	Rule Of Mixtures
SEM	Scanning Electron Microscopy
SE	Secondary Electrons
SQUID	Superconducting Quantum Interference Device
C4AF	Tetracalcium Ferroaluminate
C3A	Tricalcium Aluminate
C3S	Tricalcium Silicate
XRD	X-Ray Diffraction
ZTE	Zero Thermal Expansion

Chapter 1

Motivation

In this opening chapter, we will establish the foundations of this project: from the discussion of the problems arising from thermal cracking in infrastructure, to the introduction of an optimised mortar that could mitigate those challenges. We will cover the fundamentals and mechanisms of the latter, discuss similar works that tried to implement it and convey some alternatives to solve the same problem. Finally, as the mortars used were targeted for additive manufacturing, we will briefly mention the advantages of implementing this rising technology in the construction sector.

1.1 Infrastructure thermal cracking

Concrete is one of the most widely used construction materials in the world due to its versatility, durability, and cost-effectiveness, serving as the backbone of modern infrastructure. [1] It is then important to understand, study and improve the properties of this indispensable material.

Materials used in construction, such as concrete and mortar, expand and contract at different rates as temperature changes, causing internal stress and strain within the infrastructure, that over time, may lead to the formation of cracks and fissures. [2] Thermal cycling might become an issue in regions where there are high temperature fluctuations between day and night, between seasons or potentially from global warming. [3–5] This poses a structural integrity risk for structures, such as roads, bridges, damns, and buildings. [6, 7] Effective design, material selection, and maintenance strategies are essential to mitigate the risks of infrastructure thermal cracking and ensure the longevity of vital built assets. For example, in recent years, one of the main challenges to design the Burj

Al-Arab in Dubai, was the implementation of steel diagonal beams that were needed for the structure's integrity. They could expand up to 5 cm due to the region's weather conditions, which could lead to stress build up in the joints, compromising the infrastructure's integrity. [8]

1.2 Near zero thermal expansion materials and applications

As opposed to the conventional positive thermal expansion materials (PTE), although rare, some materials expand upon cooling and exhibit a negative thermal expansion (NTE). They are usually combined (as filler/compensators) with a PTE material to produce composites with near zero thermal expansion (ZTE), which are present in fields that require high-precision instrumentation, such as sensors, dentistry, large telescopes, cookware, and micro-devices. [9–12]

Our preliminary approach to minimise thermal cracking is to implement NTE materials in the construction sector as fillers to optimise the thermal expansion of mortars by producing a ZTE composite, as is represented in figure 1.1. Similar works have already been conducted in concrete and reported in [13–15], and we intend to complement those findings with other NTE fillers, techniques, and target mortars used for additive manufacturing, instead of concrete.

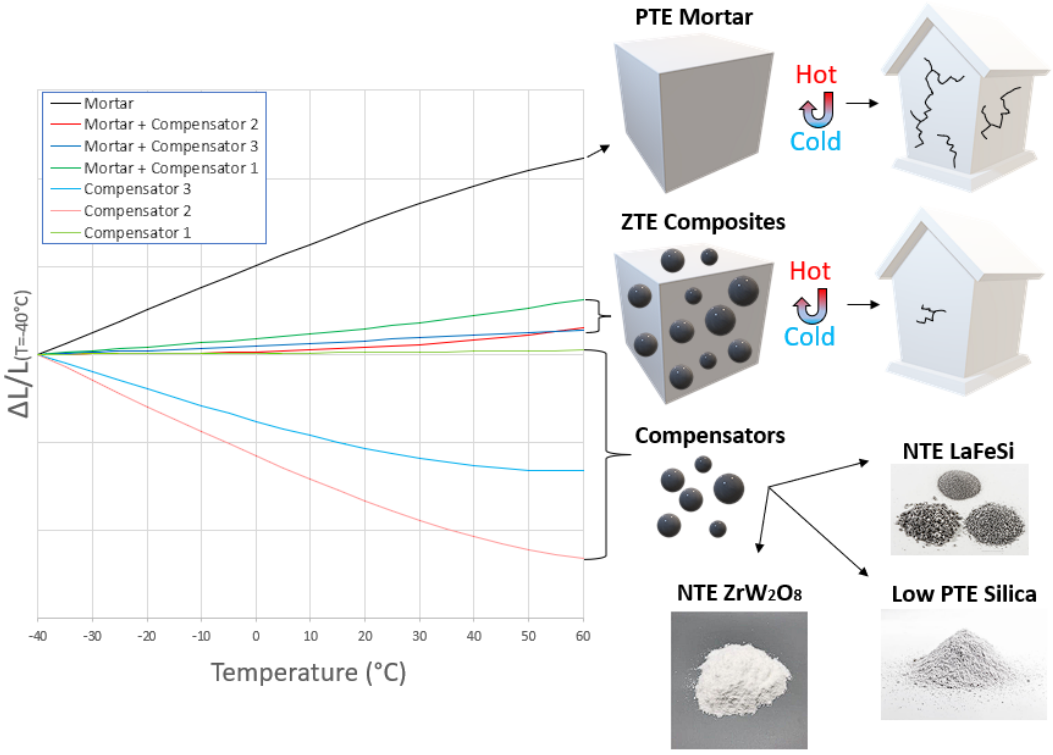


FIGURE 1.1: Overall concept of the work, where NTE materials will be implemented in PTE mortars to produce near zero thermal expansion composites, that are more resistant to thermal cycling. The graphic represents strain (or distension) as a function of temperature.

1.3 Additive manufacturing

In recent decades, there has not been a lot of progress in the innovation of building processes in the construction sector, that remains mainly based on manual labour and the same cement and aggregate mixtures. [16] Due to the extensive use of cement based materials, there is a need to reduce the negative impacts that comes from their production and use. [17] Smart materials are being introduced to cement mixes, not only to reduce these effects, but to innovate the sector by introducing materials that are responsive to changes in the environmental behaviour or sensitive to other external stimuli, thus improving the properties of the assets they are implemented in. [18] For example, piezoelectric materials can be implemented in pavement to harvest energy as people step through it. [19]

Additive manufacturing, commonly known as 3D printing, has also been introduced in the industry to further innovate its building processes and providing a more environment-friendly solution. It is a revolutionary manufacturing process that involves creating three-dimensional objects by layering material upon material, as demonstrated in figure 1.2. It

enables printing parts with a complex geometry, while reducing construction times, waste generation, manual labour, amongst other advantages. [20–22]



FIGURE 1.2: Example of 3D printed mortar. The piece is shaped layer by layer, identical to a typical 3D printer.

For the purpose of this work, mortar used for 3D printing applications was selected to reconcile this emerging new technology in the construction sector and the preliminary approach of creating a ZTE mortar composite. In this way, the expensive NTE materials introduced in the mortars may be justified for a more niche application standpoint, where thermal induced cracks are of great concern in structural design.

Chapter 2

Theory and literature review

In this section, we will convey the fundamental aspects required to understand the process of developing the ZTE mortar. We will start by detailing the composition and chemical processes involved in concrete/mortar fabrication. Then, an overview of the mechanisms behind the NTE phenomenon will be given, as well as a description of the properties and reasoning behind the selection of the fillers. Finally, we will present some analytical and numerical models that help predict the behaviour of the produced mortar.

2.1 Mortar composition and properties

The fabrication of concrete and mortar involves a series of chemical processes that play a crucial role in determining its strength, setting time, workability, and overall performance. This section aims to provide an overview of the key chemical processes involved in the fabrication of mortar, which was the main material used in this work.

To clarify, mortar is a mixture of water, cement and finer aggregates (diameters $<$4.75 mm). Concrete consists of the same materials, but also includes coarser aggregates like gravel. It has more strength and durability, and therefore is used in structural projects, whereas mortar is mainly used as a bonding agent. Nonetheless, the chemical reactions involved in both materials are the same. [1]

2.1.1 Mortar composition

The primary binding agent in mortar is cement. Primitive cement was made by combining water with crushed limestone after it was heated. Later, the Romans introduced volcanic ash (pozzolana) to the mix, which made the concrete more durable, due to the

silicates contained in the ash. [23] Today, the most commonly used mixture of cement is Portland cement, whose fabrication process involves mixing crushed limestone and silicates, and heating them in kilns to produce clinker. It is then finely grounded and combined with gypsum, and other additives. Clinker contains four main phases: [1, 24]

- C3S for $3CaO{\cdot}SiO_2$ (tricalcium silicate)
- C2S for $2CaO{\cdot}SiO_2$ (dicalcium silicate)
- C3A for $3CaO{\cdot}Al2O_3$ (tricalcium aluminate)
- C4AF for $4CaO{\cdot}Al2O_3{\cdot}Fe2O3$ (tetracalcium ferroaluminate)

Moving ahead, we will use the cement chemist notation (CNN) to refer to these phases, where C represents CaO, S is SiO_2, A is Al_2O_3, and F is Fe_2O_3.

2.1.2 Cement hydration

Cement undergoes hydration when water is added to the mix, resulting in the formation of a network of interlocking crystals. C3S and C2S react with water to form calcium silicate hydrate (C-S-H) and calcium hydroxide (CH) (commonly known as portlandite), according to the following equation: [24]

$$(C2S, C3S) + H_2O = C\text{-}S\text{-}H + CH. \tag{2.1}$$

The C-S-H is the component that contributes the most to the mortar's strength, so it is advantageous to maximise its formation. [1, 25]

C3A hydrates very rapidly in the form of hydrogarnets, so the mortar may become rigid very rapidly and cause what is called a flash set. The addition of gypsum (or calcium sulphate) is to promote the formation of a thin impervious film of ettringite at the surface of the C3A grains to slow down their hydration. In its presence, the interstitial phase (C3A + C4AF) is transformed into ettringite and monosulphoaluminate according to: [24]

$$(C3A, C4AF) + \text{gypsum} + H_2O = \text{ettringite} + \text{monosulphoaluminate}. \tag{2.2}$$

These reactions are crucial in forming the cementitious gel that binds the aggregates together, providing the necessary strength and adhesion in the mortar. [1, 24, 25]

2.1.3 Curing and other considerations

The reactions involved in the hydration process are exothermic and may not occur simultaneously. Curing is a critical process in mortar fabrication that involves maintaining adequate moisture and temperature conditions to allow cement hydration to continue efficiently. Pre-dosed mortar mixes take between 24h to 48h to cure properly and be ready for experimental testing. However it is important to note that the hydration process continues to take place as long as there is enough water to hydrate the cement particles, and therefore, the age of the mortar can impact its properties, along with various factors, such as water-cement ratio, aggregate types, porosity, temperature and moisture. [1, 26–28]

During the casting of fresh concrete, a gradient in the water-cement ratio emerges, leading to the formation of distinct microstructures within the surrounding hydrated cement paste near the aggregate particles. Represented in figure 2.1, this zone around the aggregates is called the interfacial transition zone (ITZ) and can be assumed to be an additional phase in the composite. It exhibits different properties and microstructure than the bulk, and is most significant between 15 and 20 μm around the aggregates. [29] Generally, the porosity in the ITZ is greater than the bulk, and there is a larger concentration of CH and ettringite, creating preferentially oriented crystals around the aggregates. Given these conditions, ITZs tend to be the weakest link in concrete. This leads to the formation of microcracks (predominantly in ITZs) even before loading is applied to the composite. They are also responsible for the lower tensile strength compared to the compressive strength in concrete and mortar. Additionally, the greater the aggregate size in the composite, the stronger the effects of the ITZs will be, due to the increased surface area of the particles. Considering this, finer filler particles should be used. Given that mortar has finer aggregates than concrete, they possess a more uniform composition and bonding (optimised for its bonding application), whereas concrete is engineered to withstand higher loads and structural demands. [1, 29]

One last thing to note is that cement undergoes a volumetric contraction during the first stages of hydration, when the rigid links between cement particles are not yet established. This is known as autogenous shrinkage and may lead to volumetric instability in the mortar, causing fissures and cracking, if proper moisture is not provided, and the water to cement content is too low. [30, 31]

One should take into account these phenomenons when evaluating microcracks, as

not every crack is a consequence of thermal expansion. Nonetheless, the impact of thermal cracking can become more accentuated due to these factors.

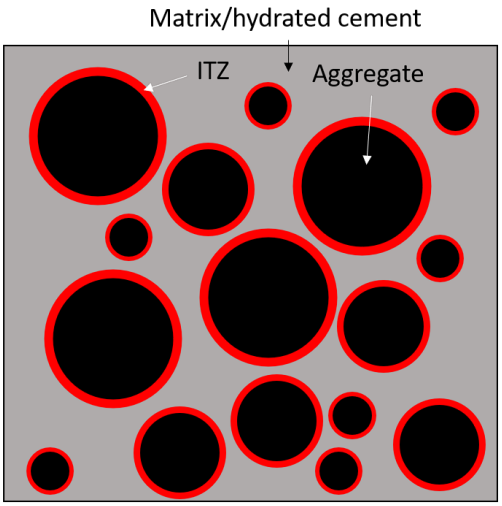


FIGURE 2.1: Mortar microstructure and ITZ.

2.2 Negative thermal expansion mechanisms

In recent years, the scientific community has witnessed a growing interest in materials that exhibit negative thermal expansion (NTE) behaviour. Unlike most conventional materials that exhibit a positive thermal expansion (PTE) and expand when heated, NTE materials contract in at least one dimension upon an increase in temperature. This unique characteristic has sparked immense curiosity and holds great promise for a wide range of applications, from precision engineering to advanced electronics. [9–12]

In this section we will start by introducing the physics behind thermal expansion, discuss the different mechanisms behind the NTE phenomena, give examples of some NTE materials, and highlight some applications. The mechanisms that give rise to NTE are well reported in a number of reviews [10–12, 32–35], so a broad description of each one will be given.

2.2.1 Thermal expansion

Based on figure 2.2, thermal expansion is quantified by the relative change in volume, $\Delta V/V$, for a given change in temperature ΔT. Thus, the volumetric coefficient of thermal expansion, α_V is given by: [33]

$$\alpha_V = \frac{\Delta V/V}{\Delta T} \tag{2.3}$$

commonly expressed in ppm/K (parts per million per Kelvin), or more precisely as (at constant pressure):

$$\alpha_V = \frac{1}{V}\left(\frac{\partial V}{\partial T}\right)_P \tag{2.4}$$

This relation holds for isotropic materials that undergo the same changes in length in all directions. For anisotropic NTE materials that exhibit NTE along specific crystallographic directions, one has to consider the coefficient of thermal expansion in every direction. For the purpose of this work, isotropic fillers were the only ones considered, as normal mortar is also isotropic, and thus, for the subsequent sections, the coefficient of linear thermal expansion will be defined as:

$$\text{CTE} = \frac{\Delta L/L}{\Delta T} \tag{2.5}$$

where $\Delta L/L$ is the relative change in length in one direction on the material. For an isotropic cubic material: [34]

$$\text{CTE} = \frac{\alpha_V}{3} \tag{2.6}$$

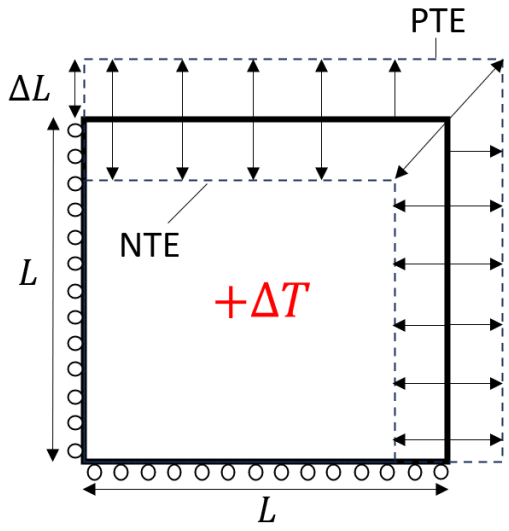


FIGURE 2.2: 2D comparison between the effects of a temperature increase on a PTE and NTE material, with initial length L.

Two atoms can be represented as being connected by an anharmonic spring that does not exactly obey Hooke's law. Pauli's exclusion principle prevents the atoms from getting too close to each other, and thus, the atoms are more likely to move towards longer interatomic distances rather than shorter ones. Therefore, with an increase in temperature, the average interatomic distance also increases, as is represented in figure 2.3. Stronger bonds

have steeper and narrower potential wells, resulting in a slower rate of increase in interatomic distances, and hence a smaller CTE. In other words, as the temperature rises, the thermal vibration of an atom intensifies, and to avoid collisions with neighbouring atoms, it naturally tries to maintain a "safe" distance from them and the mean interatomic distances increase. This expansion in distance due to high-amplitude atomic vibration is the fundamental explanation behind thermal expansion. [9] However, although rare, there are certain effects that can counteract the inherent tendency of atoms to separate as temperatures rise. These effects are responsible for the emergence of the negative thermal expansion (NTE) phenomena. These will be listed below and are summarised in figure 2.4.

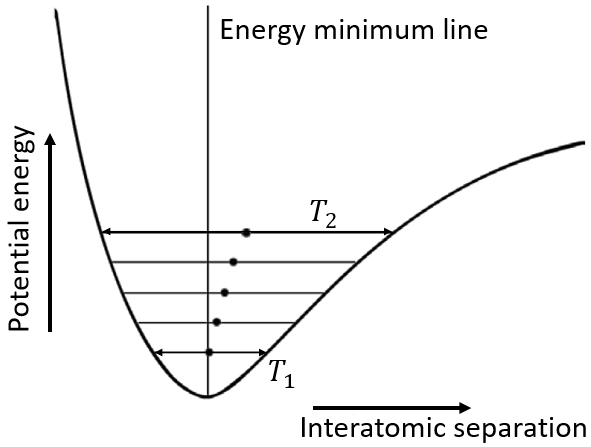


FIGURE 2.3: Typical anharmonic potential energy as a function of interatomic distance. The asymmetry of the function reflects that it will become increasingly hard to push two atoms together for small separations, and that the energy will go to zero for very large separations. The horizontal lines represent the spread of distances for a given temperature ($T_2 > T_1$), and the small circles represent the mean distance at each temperature. Adapted from [33].

2.2.2 Transverse vibrations

Earlier, it was explained that longitudinal vibrations in the direction of the bonds can lead to thermal expansion via the anharmonicity of the interatomic potential (figure 2.3). However, transverse vibrations perpendicular to the direction of the bonds, tend to shorten the chain length, and the overall vibrations can lead to NTE. This can be visualised in figure 2.5a, by different vibration modes of metal-oxygen-metal (M-O-M) links. [10, 12, 33, 34, 36]

2.2.3 Rigid unit modes (RUMs)

The conventional understanding for the NTE behaviour, can be explained by the rigid unit modes (RUM) model, that suggests that NTE arises due to the rotation or tilting of rigid structural units within the material's crystal lattice. As illustrated in figure 2.5b, as temperature increases, these units (which represent subsets of atoms) rotate, leading to a contraction along certain axes. [11, 12, 33–36]

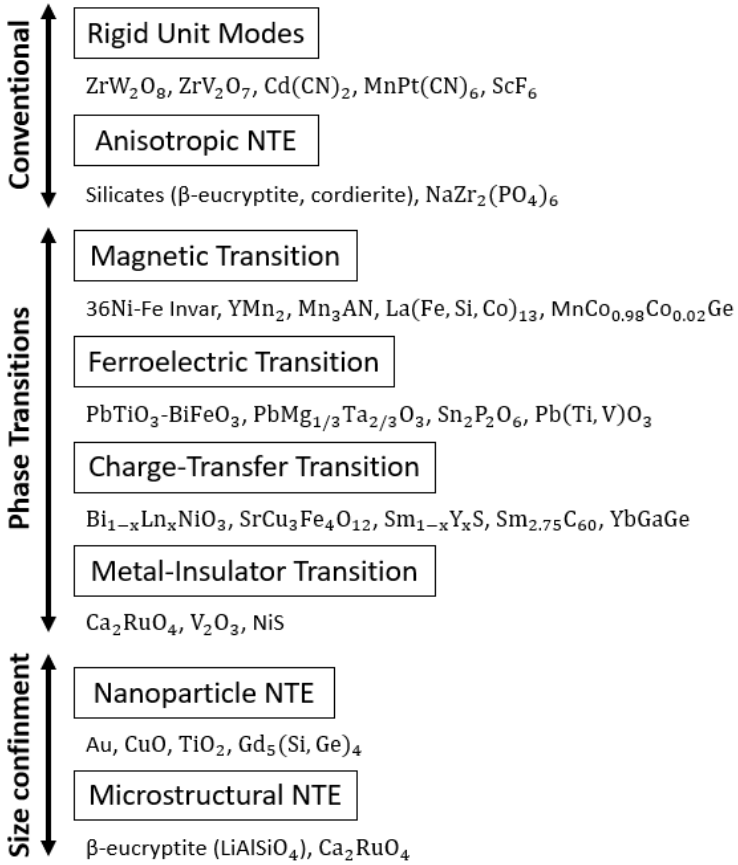
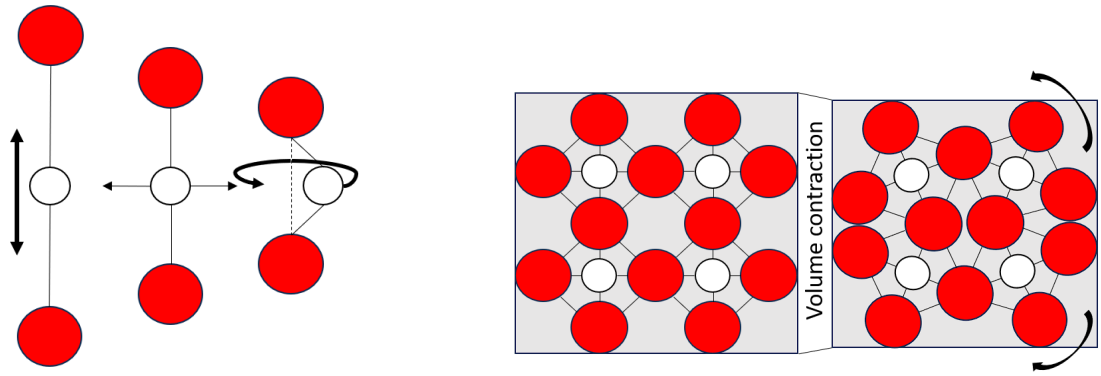


FIGURE 2.4: Classification of negative thermal expansion materials and mechanisms. Adapted from [9].

2.2.4 Phase transitions

Some structures, despite possessing rigid polyhedra, do not show this cooperative rotation of rigid units that give rise to their NTE behaviour. Instead, it is related to phase transitions where the materials undergo structural changes in certain conditions (for example at specific temperatures, external applied magnetic fields, or pressures).



(a) Longitudinal (left) and transverse (right) vibrational modes for increasing temperatures.

(b) A square lattice of rigid MO_4 units. The rigid squares rotate for increasing temperatures, leading to an overall decrease in the structure's area and being attributed to NTE.

FIGURE 2.5: 2D representation of different vibrational modes and Rigid unit modes with M-O bonds, with red dots being M, and white dots O. Adapted from [34].

In most first-order phase transitions, at the critical temperature, these materials exhibit a volume change through its structural transition, that can be associated to a magnetic transition. [9, 12, 32, 35] For example, the NTE exhibited by LaFeSi material family can be attributed to their magnetic transitions that exhibit a strong magnetovolume coupling effect [32], where the large magnetisation variation at T_C is accompanied by a large change in the crystal structure's volume across the transition. [37] Moreover, modifying the properties of these materials, by chemical substitution for example [38], is becoming a solution for controlling NTE. [9]

2.2.5 Size-confinement NTE

In some cases, there is a variation of thermal expansion compared to the standard bulk behaviour that can be attributed to distinctive size-confinement effects in the material. [10] There are examples of materials exhibiting PTE in the bulk, but NTE at the nanoscale. [39, 40] Interfaces and nanoparticles exhibit distinct structures compared to the bulk material, leading to alterations in bonding, magnetism, and elastic properties. [10, 11]

2.3 Thermal expansion compensators

In figure 2.6 we can see a comparison of the CTE values of some NTE and common PTE materials. The criteria of selection of the fillers used in the mortars was based on a

few factors such as cost, NTE temperature range, and availability . Ideally, it would have to show isotropic NTE behaviour and be suitable for moderate temperature applications around room temperature, with a constant CTE value. For industrial applications, the price would also have an impact. As NTE materials are generally more expensive compared to regular mortar and concrete fillers, a low PTE compensator could be considered, as it would also reduce the mortar's CTE, although to a lower extent. The accessibility and commercial availability would also lead to decreased experimental costs. Given these criteria, the fillers identified below were selected.

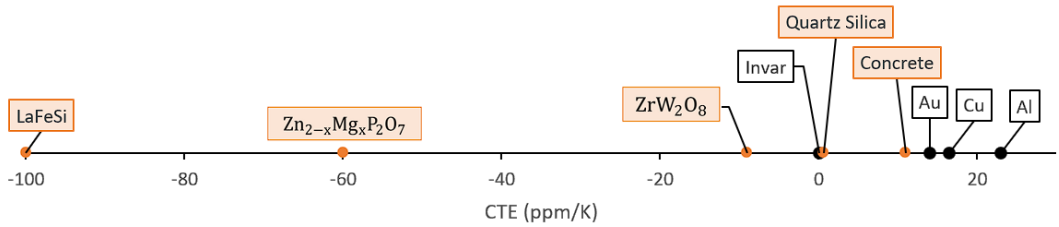


FIGURE 2.6: CTE values of typical NTE and PTE materials around 300K. Materials used in this work are highlighted in orange.

2.3.1 White micro silica powder

A fine white silica/quartz powder, SiO_2, (see figure A.2) from Sinoenergy [41] was selected as the lower cost, low PTE filler solution. Quartz powder is obtained by crushing, grinding and sieving quartz minerals. Silicate minerals such as builder's sand, found on riverbeds and beaches are already used in some mortars as fillers. We wanted to learn the influence of adding more silica, and the effects of including decreased particle sizes on the mortar's CTE. These studies were already conducted for different applications, with epoxies (instead of mortar) for example. [42, 43]

Silica actually exhibits anisotropic NTE, but with very low average values around 0.55 ppm/K. This low value is attributed to the rotation of SiO_4 tetrahedra rigid units. [44] Due to its high surface area, it provides nucleation sites for hydration products of cement, enhancing the crystallisation process (depending on the water-to-cement ratio) [45], thus improving the strength of the mortar. [25, 46–48] For these reasons, it is a good candidate as a cheap mortar filler.

2.3.2 LaFeSi-based compounds

As mentioned before, $La(Fe_{1-x}, Si_x)_{13}$-based compounds have an associated magnetovolume coupling effect, where a large magnetisation variation at T_C is accompanied by a large crystal structure volume change. This allows to tune the CTE of these first-order phase transition materials by changing their magnetic properties. [37, 49]

Downsizing this material via ball milling was conducted previously in our group by Fleming et al. [37]. They show that not only the absolute CTE value decreases for smaller particle sizes, but the temperature interval where the transition occurs, ΔT_{α_v}, also increases and makes it less sharp, meaning that the strain variation is smoothed across that temperature range and enables their implementation in room temperature ZTE applications, as is represented in figure 2.7 (average particle sizes of 1.24, 0.44, and 0.39 μm correspond to average CTEs of -112.4, -104.9, and -97.6 ppm/K, respectively) [37, 50]

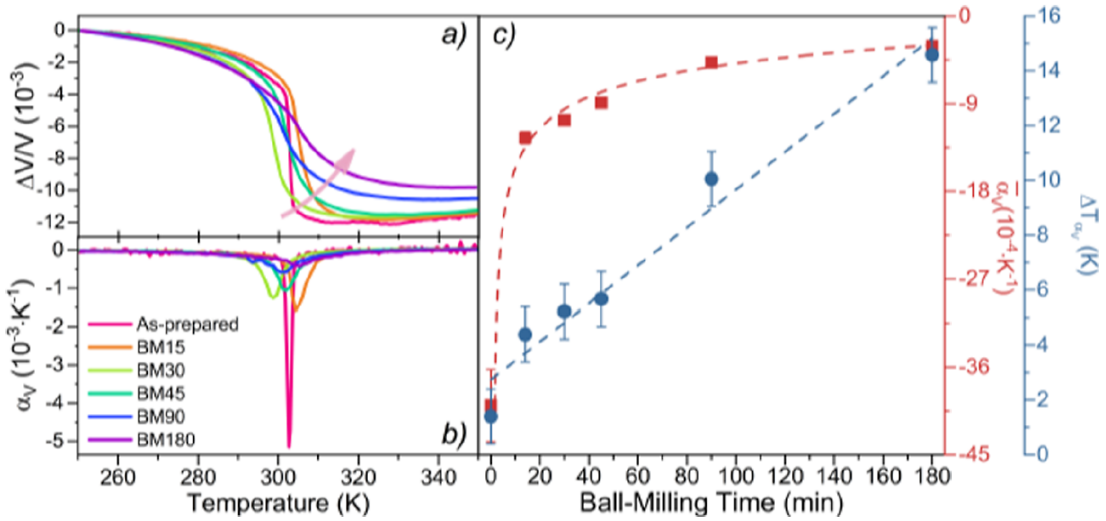


FIGURE 2.7: a) Strain as a function of temperature and (b) α_V of the as-prepared $LaFe_{11.9}Mn_{0.27}Si_{1.29}H_x$ powder and samples with different ball milling times (BM), measured in cooling as a function of temperature. (c) α_V (red dots), evaluated in ΔT_{α_V}, and the value of ΔT_{α_V} (blue dots) as a function of the ball-milling time. From [37].

They exhibit a very large NTE, which decreases the amount of material needed to have a meaningful CTE reduction in the mortar, at the cost of causing mismatch problems at the interface with other phases within the composite. Additionally, their ferromagnetic nature could lead to agglomeration, decreasing the homogeneity of the mortar, and leading to anisotropy. Nonetheless, it is important to study the introduction of these large NTE materials as composite fillers, and to analyse their behaviour experimentally.

2.3.3 Zirconium Tungstate

Zirconium Tungstate, ZrW_2O_8, is one of the most studied NTE materials and one of the first to be identified as exhibiting this phenomenon. [51] Its potential to be used in ZTE applications has already been explored in many areas, including in cements as filler. [13, 14]

As represented in figure 2.8, it has a complex cubic structure, consisting of WO_4 tetrahedra and ZrO_6 octahedra that are linked such that each ZrO_6 unit shares its corners with six different WO_4 units, and its NTE can be explained by the RUM model. [52]

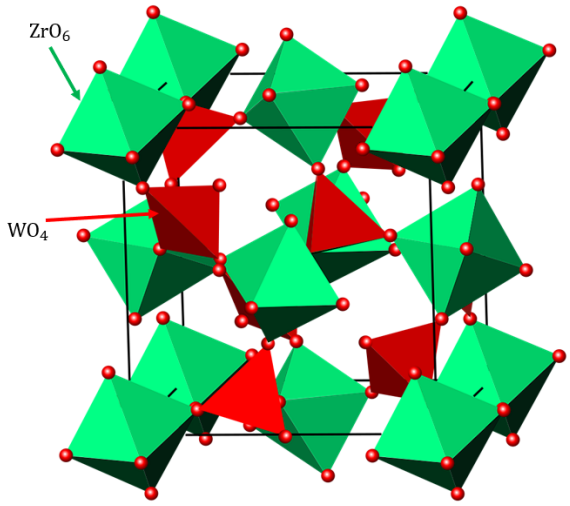


FIGURE 2.8: ZrW_2O_8 structure. Adapted from [34].

Given its isotropic NTE behaviour over a wide temperature range (-9 ppm/K for <425 K and -6 ppm/K from 425 K to 1030 K [32]), and commercial availability, it is suitable for the goals of this work and to complement previous findings (see figure A.2).

2.3.4 Fine oxide ceramic powder

Lastly, we also considered an oxide ceramic powder supplied by Misario CO., Ltd, which is a new NTE material developed at Nagoya University. The $Zn_{2-x}Mg_xP_2O_7$ has a CTE of about -60 ppm/K from 280-350 K associated to a unite cell volume contraction. [53] It shows an anistotropic expansion in the unit cell, which does not translate to microstructural effects leading to microcracks on thermal cycling, meaning that it is suitable for thermal expansion compensation at room temperature. [54] The reagents are environmentally friendly and relatively low cost, making it a cheaper NTE solution for thermal

expansion compensation applications. [53, 54] However, it was not included in the measurements due to lack of time, but should be considered and studied in future work.

2.3.5 Price comparison

To shed some insight about the costs of implementing these fillers in the industry, a price comparison between them and a regular cement bag was made. Cement is the most expensive component of concrete and mortar, so adding aggregates to the mixes help reduce construction costs, while maintaining the required strength and integrity of the composites. In table 2.1 a list of the prices of the fillers and cement is given, as well as an estimate of the cost of using compensated mortars to build a 1x1x0.1m ($0.1m^3$) wall with 10% filler. Note that these prices were converted from US dollars at current currency exchange and inflation rates (as of August, 2023). Values also vary by region, manufacturer and other factors, so a range of prices was given.

Material	price (€/Kg)	wall cost (€)
Portland Cement [55]	0.09-0.14	16-23
Silica powder [41]	0.63-2.33	37-107
LaFeSi [56]	7.44	290-297
ZrW_2O_8	200-890	6933-30811

TABLE 2.1: Filler and cement prices, and material cost to build a wall of 1x1x0.1 m (0.1 m^3) with 10% filler. ZrW_2O_8 prices were estimated based on various manufactures costs, and the price of producing it, taking into account the cost of the individual reagents, electricity and technicians time.

As we can see, adding the fillers increases the construction price by a large margin, especially with ZrW_2O_8. It is important to note that different filler volume fractions will yield different CTE reductions for each filler. This means that the amount of filler used to achieve the same CTE reduction is lower in the more expensive NTE materials, making the wall costs given above slightly exaggerated. However, as concrete is the most used material in the world, keeping the prices low is of great interest, for large scale construction. Nonetheless, for particular applications where thermal cracking is relevant and important to be avoided, these compensated mortars might be needed to increase the durability of infrastructure and to keep them mechanically stable for longer periods of time.

2.4 Predictive models for the coefficient of thermal expansion of composites

Many analytical formulas have been derived to evaluate the CTE of different types of heterogeneous composites. These will be discussed below and are revised in [57]. The ones we will be focused on are mainly for heterogeneous, isotropic, and two phase composites. Numerical models based on finite element analysis (FEA) will also be discussed as a closer representation to real applications.

2.4.1 Analytical models

The rule of mixtures (ROM) is the most simple analytical model and assumes uniform stress in the composite's structure. The CTE for the Voigt upper bound [58] is given by:

$$\text{CTE} = \frac{(1-\phi)E_m\text{CTE}_m + \phi E_f \text{CTE}_f}{(1-\phi)E_m + \phi E_f} \tag{2.7}$$

where ϕ is the filler's volume fraction in the composite, E is Young's Modulus, CTE is the coefficient of linear thermal expansion, and the subscripts m and f are used to refer to the matrix and filler, respectively.

Reuss [59] assumption of uniform stress in the composite simply gives:

$$\text{CTE} = (1-\phi)\text{CTE}_m + \phi\text{CTE}_f \tag{2.8}$$

This is the ROM formula that is going to be used for model comparison. Turner's model [60] also considers mechanical interactions between phases like 2.7, but, instead, it provides a lower bound estimation for the CTE and uses the bulk modulus instead of E:

$$\text{CTE} = \frac{(1-\phi)K_m\text{CTE}_m + \phi K_f \text{CTE}_f}{(1-\phi)K_m + \phi K_f} \tag{2.9}$$

where K is the bulk modulus.

The last model used to predict and compare the CTE of the mortar was based on the studies of Levin [61], Rosen and Hashim [62], and Schapery [63]. It considers isotropic spherical particles involved in an isotropic matrix, leading to the following equation:

$$\text{CTE} = \text{CTE}_m + (\text{CTE}_f - \text{CTE}_m)\frac{K_f(K_m - \overline{K})}{\overline{K}(K_m - K_f)} \tag{2.10}$$

where the upper and lower bounds are calculated using the Hashin-Shtrikman [64] estimate on the effective bulk modulus $\overline{K}$:

$$K_l = K_m + \frac{\phi}{\frac{1}{K_f - K_m} + \frac{3(1-\phi)}{3K_m + 4G_m}} \tag{2.11}$$

$$K_u = K_f + \frac{1-\phi}{\frac{1}{K_m - K_f} + \frac{3\phi}{3K_f + 4G_f}} \tag{2.12}$$

where the subscripts l and u are used for lower and upper bounds, respectively, and G is the shear modulus.

2.4.2 Finite element analysis (FEA)

Finite Element Analysis is a numerical technique used to approximate the behaviour of physical systems by dividing them into smaller, manageable elements. These elements are interconnected at nodes, forming a mesh that represents the overall geometry of the system. Examples of different mesh sizes can be seen in figure 2.9. The governing equations, often derived from principles of mechanics and physics, are then applied to each element, generating a system of equations that can be solved numerically. [65]

To simulate a composite's mechanical properties, an established technique involves employing a representative volume element (RVE), wherein a matrix material encapsulates one or more varieties of reinforcements such as fibers or particles (see figure 2.9). This facilitates the emulation of intricate heterogeneous composites featuring a periodic arrangement of constituents. [66] Implementing interfacial transition zones (ITZ) can further improve the accuracy of the simulated models. [29] In this work, the inclusion of ITZs was omitted for simplicity. A more thorough explanation of the implemented model will be given in section 3.1.

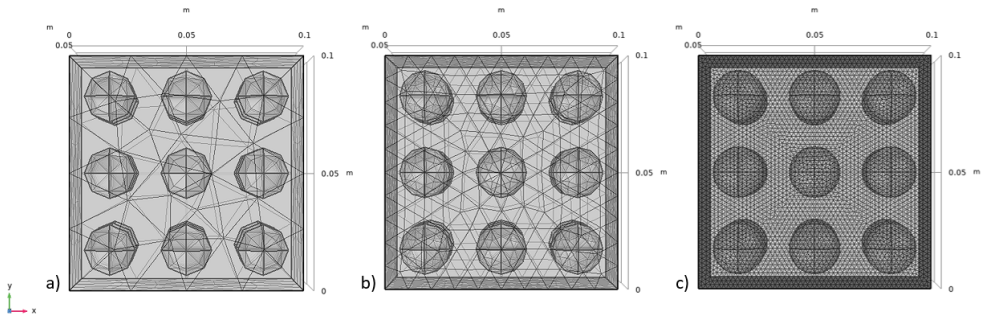


FIGURE 2.9: Representative volume elements (RVEs) meshed with elements of a) extremely coarse size (9362 elements), b) normal size (37128 elements), and c) extremely fine size (2198409 elements).

Chapter 3

Experimental Section

In this chapter, we will detail the techniques, methods and procedures used throughout the whole work, including mortar fabrication and composition characterisation, composite simulation setup and all the preparations for the thermal expansion measurements.

3.1 FEA of the mortar's thermal expansion

The goal of the finite element analysis (FEA) models was to simulate the mortar's CTE by studying the impact of various factors, including the distribution, CTE and volume fraction of the filler material in the composite.

In this section, the discussion will be focused on the setup implemented in the FEA models, including the simulated materials and their properties, the geometries and distributions of the filler materials, and the analysis methods. The software used was version 6.1 of COMSOL Multiphysics and its structural mechanics module [67].

3.1.1 Modelling setup

Before detailing the materials and composite's geometry used in the study, an overall explanation will be given regarding the initial setup and settings used in the simulations.

We used both 2D and 3D models in a stationary study environment and the solid mechanics physics within the structural mechanics module in COMSOL. The 2D models were used initially to better understand how the simulations would be conducted. Later, 3D models were used for the final modelling analysis due to the obvious closer connection to real world conditions. [68] Nonetheless, both models produced similar results, but only

the 3D models will be further discussed in the result analysis. A comparison of the same composite's geometry corresponding to each model is given in figure 3.1.

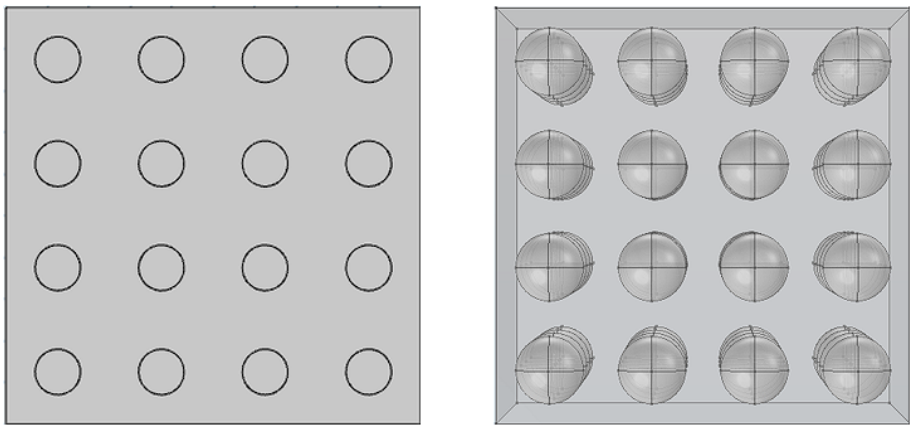


FIGURE 3.1: a) 2D and b) 3D model comparison for corresponding composite's geometry. Circles and spheres represent the filler, and the square and cube represent the matrix. Both models have the same filler distribution and concentration.

Under the model builder tree (MBT) interface, the geometry of the matrix, corresponding to the mortar, and the filler, corresponding to the added filler in the composite, are then drawn. Next, a material was assigned to each component and their properties set. As explained earlier, the mortar is already a composite with different phases, but for simplicity, it was assumed as a single homogeneous material. The details regarding material properties and composite's geometry will be further discussed in sections 3.1.2 and 3.1.3, respectively.

After establishing the composite's properties and geometry, boundary conditions were applied to the model. This was done by implementing roller supports under the solid mechanics branch in the MBT. They were fixed to the xy, yz, and zx planes (x and y axis in the case of the 2D models) to allow the composite to expand freely in the positive direction of each axis. Next, loading was applied in the form of a temperature change. Under the linear elastic material model branch of the solid mechanics in the MBT, the thermal expansion option was added, where two temperatures were defined. A reference temperature of $T_{ref} = 350$ K and a user defined temperature of $T = 220$ K were applied, giving a temperature change of $\Delta T = 130$ K, similar to the temperature range applied during the thermal expansion measurements that will be discussed on section 3.8. [68]

Next, the model was meshed, meaning that it was broken down into smaller elements,

as discussed in section 2.4.2. Finer meshes yield more accurate results at the cost of computing time. For this reason, a fine physics-controlled mesh was chosen in the MBT for the simpler models, while some of the more computing demanding models were simulated using a normal mesh.

3.1.2 Materials used and their properties

The materials used in the study had the replicated properties of the materials used in the experimental measurements. Those include the commercial non compensated mortar, a LaFeSi based compound ($LaFe_{11.9}Mn_{0.27}Si_{1.29}H_x$), white silica powder and Zirconium Tungstate, ZrW_2O_8. To run the FEA model, four material properties are required: the density, ρ, the coefficient of thermal expansion, CTE, the Young's modulus, E, and the Poisson's ratio, ν. Additionally, to calculate the CTE of the models presented in section 2.4.1, the bulk modulus, K, and the shear modulus, G, are also required. All the material properties are listed in table 3.1.

Material	E (GPa)	K (GPa)	G (GPa)	ν	ρ (g/dm^3)	CTE (ppm/K) (250-350 K)
Mortar	30 [69]	16.6 [69]	12.5 [69]	0.2 [69]	2.3 [69]	33 (this work)
Silica [70]	70	35.5	30	0.17	2.2	0.6
LaFeSi	97 [71]	80.83 [71]	37.3 [71]	0.3 [71]	5.91 [72]	-97.9, -104.9, -112.4 [37]
ZrW_2O_8 [68]	88.3	73.58	34	0.3	5.09	-9

TABLE 3.1: Materials used and their properties.

It is important to note that some of the real properties of the materials (especially the mechanical properties of LaFeSi) are rough estimations and may not match the true values. Such discrepancy will further contribute to the potential differences between the simulated results and the experimental ones.

3.1.3 Composite geometry and filler distribution

In this section we will explain how the distribution and volume fraction of the fillers were implemented in COMSOL Multiphysics, as well as the overall composite's structure.

To start, a square and a cube block (for the 2D and 3D models, respectively) of side $L = 0.1$m were created in the geometry tab to define the matrix of the composite.

The distribution of the filler was studied by adding an increasing amount of particles to the model, but with decreasing dimensions, to maintain the same volume fraction for

different configurations. Ideally, the spatial distribution of each particle should be random to mimic real applications. To simplify the model, an array of circles and spheres with a symmetrical pattern, centred in the middle of the square and cube, were used for the 2D and 3D models respectively, as can be seen in figure 3.1.

Under the geometry tab, each particle geometry can be added and an array constructed. A few parameters have to be defined in order to construct the desired configuration, those being the radius of the particles, r, the initial position of the first particle, $x_0 = y_0 = z_0 = C$, and the spacing between particles (which is simply $2C$). Those values will vary depending on the volume fraction, ϕ, and number of inclusions, n. To this end, the following equations were used to determine the radius:

$$r_{2D} = \sqrt{\frac{\phi A}{n\pi}} \qquad\qquad r_{3D} = \sqrt[3]{\frac{3\phi V}{4n\pi}} \tag{3.1}$$

where A is the area of the square matrix, and V the 3D corresponding volume.

The following equation was used to determine the initial particle coordinates $C = x_0 = y_0 = z_0$:

$$C_{2D} = \sqrt{\frac{A}{4n}} \qquad\qquad C_{3D} = \sqrt[3]{\frac{V}{8n}} \tag{3.2}$$

After defining the particle distribution, it is subtracted from the matrix. This finally leaves us with two domains, one being the matrix with holes and the other the filler inclusions.

Examples of the geometries used with fixed filler volume fraction are given in figure 3.2 and with fixed number of particles in figure 3.3.

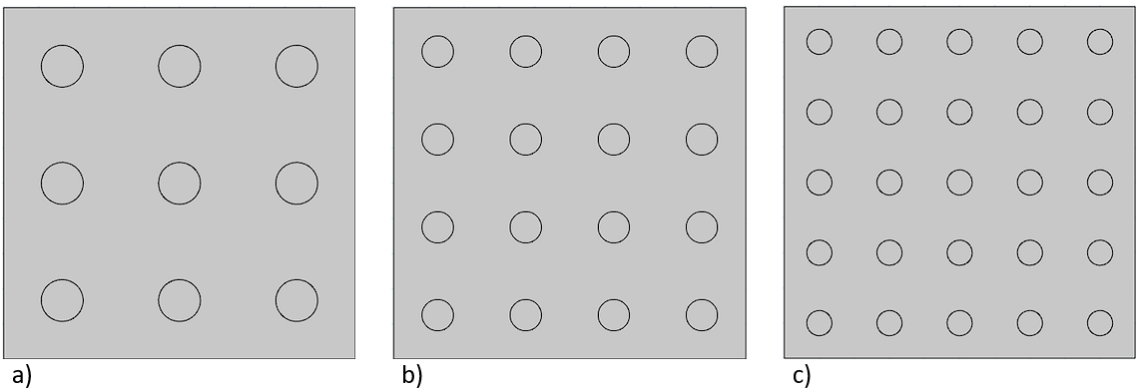


FIGURE 3.2: 2D composite geometries with different number of particles: a) 9 particles, b) 16 particles, c) 25 particles, and same filler volume fraction.

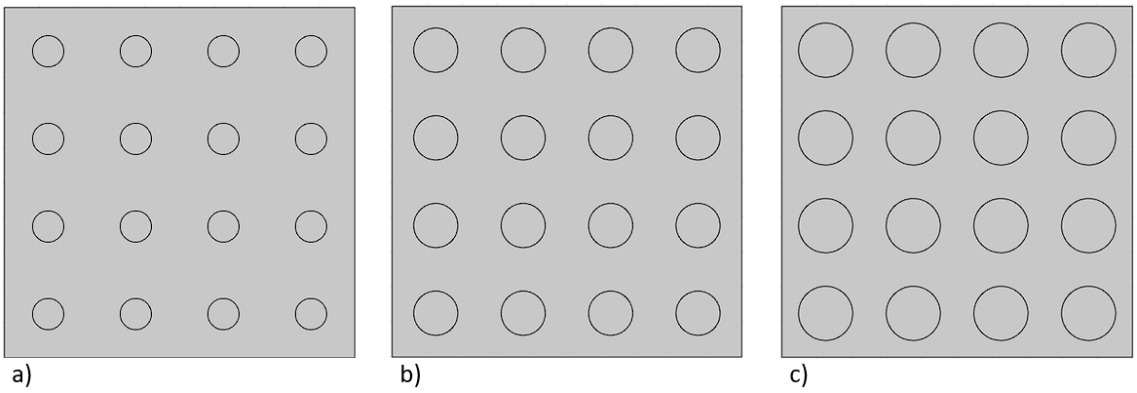


FIGURE 3.3: 2D composite geometries with different filler volume fractions: a) 10%, b) 20%, c) 30%, and same number of particles.

3.1.4 Model analysis

After the model's study is finished, displacement and von Mises stress plots are shown under the results tab in the MBT. The displacement, is represented by a deformation plot that extends the original black lines of the composite, similar to what can be seen in figure 2.2. A volume integration option was then selected in order to calculate the deformation, ΔV, of the composite. Knowing the initial volume of the cubic composite, V, with length $L = 0.1$ m, and the temperature change applied, we can obtain α_V using equation 2.3, and finally the CTE using equation 2.6.

Each material has a yield strength and if the von Mises stress surpasses that point, the material passes from an elastic behaviour to a plastic one. This stress analysis is usually implemented to understand at which point a material will yield, but is mostly used in ductile materials such as metals and is not recommended for brittle materials like mortar [73]. Nonetheless, the analysis made in this work was merely comparative and to give an overview of the magnitude and stress distributions within the composites. In that sense, the von Mises stress can be applied.

3.2 Taguchi method implementation

The Taguchi Method is a statistical technique that involves reducing the variation in a process through robust design of experiments. It enables a decreased amount of experimental runs for determining which factor is the most influential in a study, resulting in less resource and time consumption. [74] In that sense, this method was applied here to

evaluate the influence of various factors on the mortar´s CTE, while making as little time consuming FEA simulations as possible.

This experimental design involves using orthogonal arrays, which are pre-designed matrices that organise the factors affecting the "process" in study and the levels at which they should be varied. These arrays ensure that all possible combinations of the factor's levels are tested, while minimising the number of experimental runs.

In our case, the "process" we want to study is the effect of various factors on the mortar's CTE. The major factors include the amount of particles within the composite, and the CTE and volume fraction of the filler phase in the composite. We then have 3 factors and we attributed 3 levels to each one, meaning that we created a 3 factor and 3 level design. Each level attributed and the orthogonal array created are represented in figure 3.4.

These simulated results were conducted in COMSOL Multiphysics and for each simulation, the CTE of the composite was recorded. The setup was already discussed in section 3.1 and the filler used for this study was LaFeSi. The values chosen for the particle amount were based on the setup for the filler distribution discussed in section 3.1.3. The values for the filler CTE were based on the LaFeSi values listed by Fleming et al. [37] for different particle sizes. The values for the filler volume fraction were based on realistic values for application purposes.

	Factors		
level	Particle amount	Filler CTE (ppm/K)	% filler
1	27	-97.6	5
2	64	-104.9	10
3	125	-112.4	25

a)

	Factors		
Experiment	Particle amount	Filler CTE (ppm/K)	% filler
E1	27	-97.6	5
E2	27	-104.9	10
E3	27	-112.4	25
E4	64	-97.6	10
E5	64	-104.9	25
E6	64	-112.4	5
E7	125	-97.6	25
E8	125	-104.9	5
E9	125	-112.4	10

b)

FIGURE 3.4: a) Factors and levels used and the corresponding b) implemented orthogonal array in the Taguchi design.

A multivariate analysis was used to analyse and understand the relationships among the factors. In particular, a regression analysis was used to model these relationships, which allows to quantify the effect of each factor on the mortar's CTE, which is the figure of merit.

With this design, we were able to identify the most influential factors and their optimal settings with minimal experimental effort.

3.3 Mortar fabrication

In this section we will detail the process adopted for mortar fabrication. The moulds used are represented in figure 3.5. The smaller ones were designed to cast the LaFeSi mortar samples, as the quantity available of this filler was low (≈4 g). Another reason was to directly make the desired shape for the thermal expansion measurements, as the cryostat sample mounting is also small. However, some challenges arose and some of the casts produced from these moulds were mechanically unstable and very brittle (see appendix A.2). Later, slightly larger samples were produced in the larger moulds by constraining the dimensions with styrofoam involved in tape. These casts, along with the larger ones, were later grinded down to the desired shape using a 120-grit silicone carbide grinding paper. To facilitate the demoulding process, cling film was shaped into the moulds.



FIGURE 3.5: Moulds used for a) larger casts, b) intermediate casts with styrofoam to constrain dimensions, and c) smaller casts.

The fundamental materials needed to make mortar are water, cement and fine filler aggregates. As mentioned before, we used a Weber 160-1 pre-dosed mortar for 3D printing

applications [75]. It already contains a mixture of cement and aggregates and an established water demand of 12.5% by mass to be added. Mortar composition will be further detailed in section 4.1. The fillers were then added to this mortar mixture.

To produce the desired filler volume fractions in the composite, the density of each phase must be known and is given in table 3.1. With this information, the mass of the materials needed to be added in the mixture was determined by the total volume of the mortar desired, V and the volume fraction of the filler, ϕ. The following equations were used:

$$m_{mortar} = \frac{V}{\frac{1}{\rho_{mortar}}\left(1+\frac{\phi}{1-\phi}\right)+\frac{0.125}{(1-0.125)\rho_{H_2O}}\left(1+\frac{\rho_{filler}}{\rho_{mortar}}\frac{\phi}{1-\phi}\right)} \tag{3.3}$$

$$m_{filler} = \frac{\phi}{1-\phi}\frac{\rho_{filler}}{\rho_{mortar}}m_{mortar} \tag{3.4}$$

$$V_{H_2O} = \frac{0.125}{1-0.125}\frac{(m_{mortar}+m_{filler})}{\rho_{H_2O}} \tag{3.5}$$

where m_{mortar} and m_{filler} are the mass of the pre-dosed mortar and filler, respectively, V_{H_2O} is the volume of water to be added, and ρ_{mortar}, ρ_{filler} and ρ_{H_2O} are the densities of the pre-dosed mortar, filler and water, respectively.

Finally, the solid parts of the mixture were then thoroughly mixed with a flat spatula in a clean surface until homogeneity was observed. Next, the water was added and the mixture was mixed until the desired consistency was achieved (see figure A.1). The paste was then poured into the moulds, which were tapped and vibrated in order to release trapped air bubbles inside the mixture, and to also unify it. They were left to cure in ambient temperature conditions for 2 days. During this period, some samples were hydrated to maintain moisture content relatively high, as it was not being controlled. [14]

3.4 X-ray diffraction

X-Ray diffraction (XRD) is a characterisation technique used to analyse the atomic and microstructure of a material.

In general, diffraction is a phenomenon that occurs when waves bend around objects. Given the wave-like nature of light, it also produces this effect when its wavelength is of the same order as the dimensions of the objects it hits. X-rays have wavelengths in the order of the interatomic distances ($\approx 1 \times 10^{-10}$ m), and thus notably interact with the periodic structure of materials. Let us picture an x-ray beam targeting an organised array

of atoms, where diffraction occurs. As represented in figure 3.6, although the waves cancel each other in most directions through destructive interference, when x-rays are collimated in a material where the atoms are arranged symmetrically with a separation distance d, the x-ray waves will interfere constructively only where the path-length difference $2dsin\theta$ is equal to an integer multiple, n, of the wavelength, λ [76]. This produces a diffraction maximum in accordance with Bragg's law:

$$2dsin\theta = n\lambda \tag{3.6}$$

This relation is very useful to convert the measured data (intensity versus 2θ), to the interplanar distances d corresponding to each diffraction peak. It is important to note that n represents the infinite integers multiples of 2π, so a single d will rise to many diffractions. This results in diffractogram patterns where multiple peaks will represent different distances d, which are periodic. Meaning that the same pattern will repeat for higher θ for increasing integers n, according to equation 3.6.

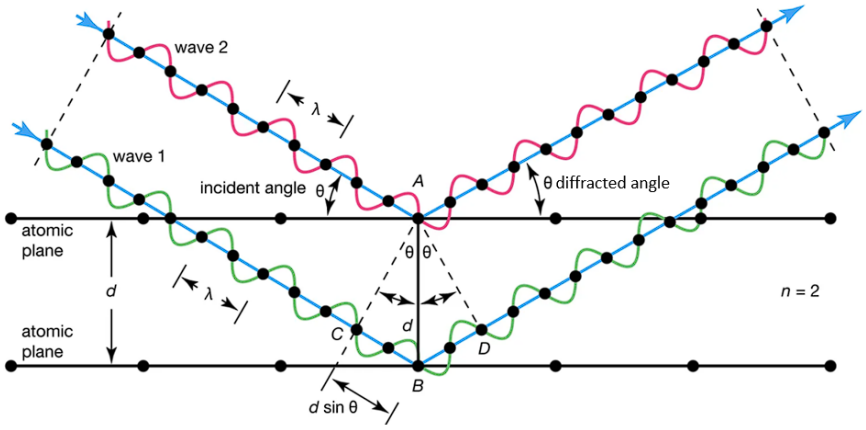


FIGURE 3.6: Schematic representation of x-ray diffraction. Adapted from [77].

The data is obtained with diffractometers which consists of an X-ray tube, a sample holder, and an X-ray detector. The x-rays can be generated in a cathode ray tube by heating a filament to produce electrons and accelerate them towards a target by applying voltage. When the electrons have sufficient energy to dislodge the inner shell electrons of the target material, characteristic X-ray spectra are produced (see figure 3.9), with the most common components being K_α and K_β radiation. This radiation is directed onto the sample by optical sub-elements, and when the Bragg's law is satisfied, constructive interference occurs and a peak in intensity is recorded in the detector.

The x-ray diffraction data acquired in this work was obtained using the Rigaku's Smartlab x-ray diffractometer [78] with a copper target ($\lambda_{K_\alpha} = 1.5406$Å) for x-ray generation, and a Bragg-Brentano $\theta - \theta$ geometry (where both the x-ray source and detector move at an angle θ and the sample is fixed).

One of the main applications of this technique is the identification and characterisation of crystalline solids, each of which produces a distinctive diffraction pattern. Both the positions (corresponding to lattice spacings) and the relative intensity of the peaks in a diffraction pattern are indicative of a particular phase and material, providing a "fingerprint" for each one. This means that it is possible to identify an unknown material or the components in a composite by comparing it to the "fingerprints" of a dataset, as shown in figure 3.7. This method was implemented to determine the composition of the mortars used and produced, alongside a scanning electron microscopy (SEM) analysis that will be discussed in the next section.

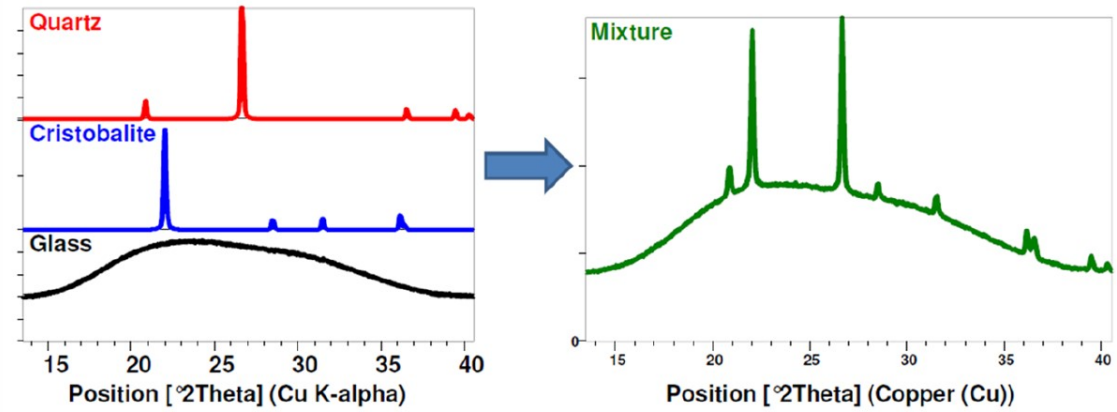


FIGURE 3.7: Identification of the composition of a composite by comparing the individual "fingerprints" of known materials.

As a side note, the diffraction peak positions can be used to calculate the unit cell dimensions and lattice parameters of a material (assuming a cubic unit cell) by:

$$d = \frac{a}{\sqrt{h^2 + k^2 + l^2}} \tag{3.7}$$

where a is the lattice parameter, and h, k, and l are the Miller indices which indicate the orientation of the periodic lattice planes separated by spacing d.

Heating or cooling said sample will change its interatomic distances, which will be reflected in a change in peak position. That means that we can accurately measure the lattice parameter (using equations and 3.6 and 3.7) as a function of temperature to determine the material's CTE. This method was not used in this work, due to lack of temperature

control in the diffractometer, and the alternative method employed will be discussed in sections 3.7 and 3.8. Nonetheless, XRD proved useful to complement the chemical and microstructural morphology analysis of the mortars and identify each phase present.

3.5 Scanning electron microscopy

Scanning Electron Microscopy (SEM) is a powerful imaging technique that enables the study of surface morphology, topography, and chemical composition of a wide range of materials at high resolution.

As we can see in figure 3.8, unlike optical microscopes that use light waves, SEM employs a beam of accelerated electrons, generated in an electron gun. These electrons are accelerated by an electric field and focused onto the sample by a system of electromagnetic lenses. As the beam interacts with the sample, which is under vacuum, it generates various signals from backscattered (BSE) and secondary electrons (SE), x-rays, amongst others [79]. These signals carry valuable information about the surface characteristics and composition, and are then amplified, processed, and converted into a visual representation on a monitor.

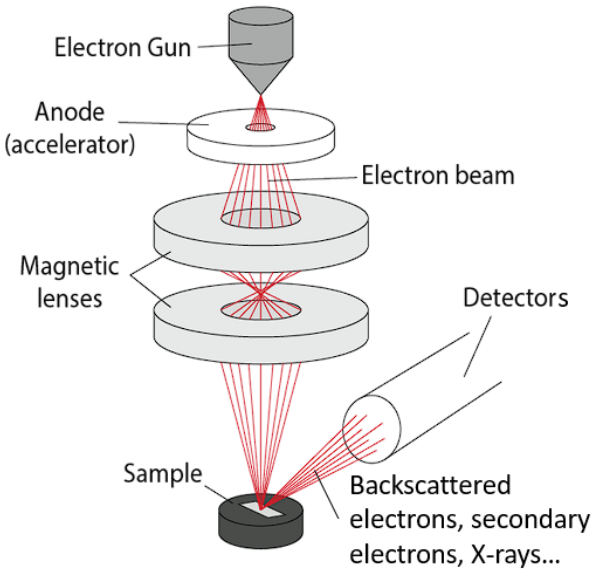


FIGURE 3.8: SEM instrumentation and working principles. Adapted from [80].

Represented in figure 3.9, are some of the electron beam interactions with the sample. Secondary electrons are a result of inelastic impact from the primary electron (PE) beam into the target's electrons. They are responsible for the high resolution images of the

sample surface due to their low energies, which makes their signal highly localised at the point of impact of the primary electron beam.

Backscattered electrons are reflected back after elastic interactions between the beam and the target. They penetrate deeper into the sample, giving different information than secondary electrons. They have high sensitivity to differences in atomic number, making heavier elements appear brighter in the image.

X-rays generation was mentioned in the XRD section 3.4. The energy of the emitted x-rays can be measured by Energy dispersive X-ray spectroscopy (EDS) detectors integrated within the SEM system. This allows to perform a chemical mapping, highlighting the distribution and abundance of different elements within the sample.

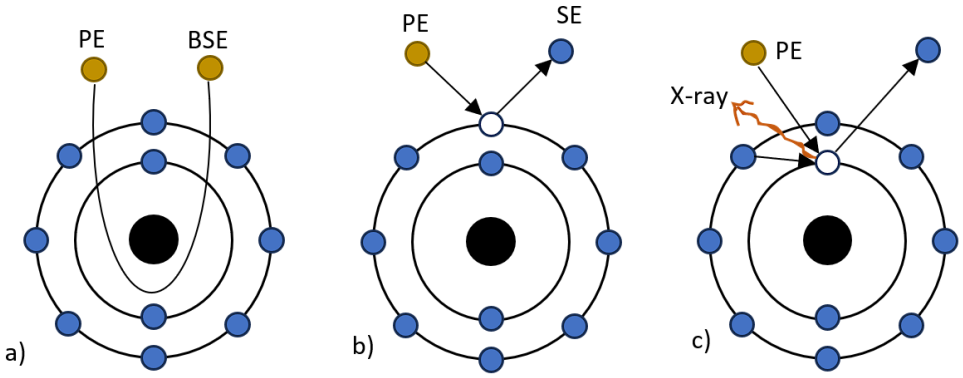


FIGURE 3.9: Different interactions between the incident primary electrons (PE) and the sample, producing different signals from a) backscatterd electrons (BSE), b) secondary electrons (SE), and c) characteristic x-rays.

Using these tools, it was possible to infer the composition of the mortars produced by highlighting a specific area in the SEM images and looking at the elements present within it. Also, the high resolution images can give details regarding homogeneity in the mortars or the presence of agglomerations and microcracks. This analysis is going to be explored in section 4.1.

The surface of the commercial mortar was smoothed with a 280-grit silicone carbide grinding paper and removed of dust. The initial brittle produced compensated mortars were not smoothed as they were too fragile. The mortars were then placed on a stub, with a conductive double sided carbon tape holding it in place. As the mortars are non-conductive, high vacuum with higher electron beam energies was not performed. Nonetheless, as the surface analysis was the most important, high magnified images were not required. The data was obtained using FEI Quanta 400FEG ESEM/EDAX Genesis

X4M equipment at the Materials Centre of the University of Porto (CEMUP), with electron beam voltages of 15 kV.

3.6 Ball Milling

As already mentioned, Fleming et al. [37] tailored the CTE of the LaFeSi compound by mechanically decreasing its particle size. This was done using the ball milling method, that involves grinding solid materials using the repetitive impact of spherical balls, as illustrated in figure 3.10.

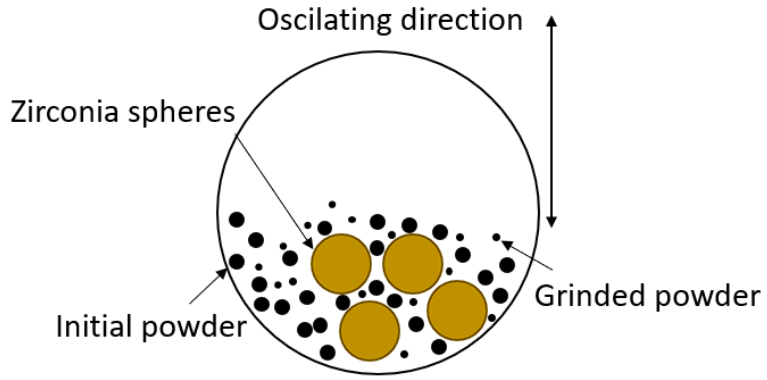


FIGURE 3.10: Ball Milling Schematic, where the zirconia spheres grind down the powder via continuous mechanical impacts.

The exact same powder from their work was used to produce the LaFeSi compensated mortars, with stoichiometry $LaFe_{11.9}Mn_{0.27}Si_{1.29}H_x$. For simplicity, this powder will be referred as "LaFeSi" throughout this work. The T_C of the initial powder was around 305 K, and the final powder was grinded for 180min, with no liquid included in the process. The same procedure was conducted for another powder ($LaFe_{11.75}Mn_{0.43}Si_{1.32}H_x$) with a T_C around 277 K. 0.71g were placed in a zirconia vessel along with 4 zirconia spheres with 5 mm and 38g each, leading to a powder-to-ball mass ratio of about 214. The vessel was installed on a FRITSCH PULVERISETTE 23 Mini Mill, and the vertical oscillating frequency was set to 50 Hz. Sets of 10 min with 10 min intervals were done to avoid overheating. After 180 min, the powder was extracted. A comparison between the initial and final powder can be visualised in figure 3.11.

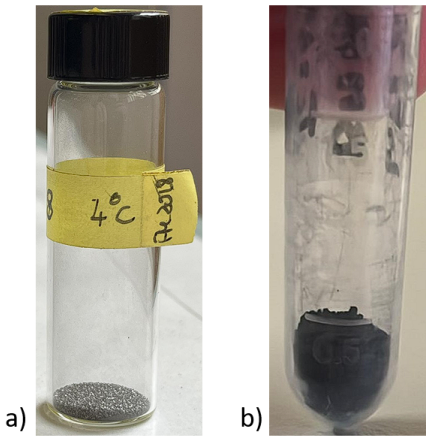


FIGURE 3.11: Comparison between the a) as prepared $LaFe_{11.75}Mn_{0.43}Si_{1.32}H_x$ powder and b) the final 180 min grinded powder.

3.7 Strain Gauge sensor

A strain gauge sensor is a device used to measure strain, ϵ, on a material, which is defined by:

$$\epsilon = \frac{\Delta L}{L} \tag{3.8}$$

where L is the material's initial length in a given direction, and ΔL its deformation.

Usually, a strain gauge is comprised of a foil of a resistive alloy with a serrated pattern deposited within a thin polymer (see figure 3.12).

Strain is sensed through a change in the strain gauge's electrical resistance. The resistance of a rectangular material of resistivity ρ_m across its longer dimension, L, is given by $R = \rho_m \frac{L}{A}$, where A is the cross-sectional area, perpendicular to the electrical current direction. As can be seen in figure 3.12, the resistive foil has a zig-zag pattern. Due to this shape, as the foil deforms, the change in the gauge length L (see figure 3.12) is much higher than the cross-sectional area change. This results in a greater base-line resistance and a bigger sensitivity to resistance changes upon deformation along the gauge length. Due to this asymmetry in sensitivity, these strain gauges are called linear pattern strain gauges, designed for measuring deformation along a single direction.

The gauge is adhered to the surface of a material via a suitable adhesive and it is expected to deform when the given material deforms. As it does, the electrical resistance of the strain gauge will change by a small amount ΔR, that can be related to the strain, ϵ, by the Gauge factor GF:

$$GF = \frac{\Delta R/R}{\epsilon} \tag{3.9}$$

where R is the initial resistance of the strain gauge.

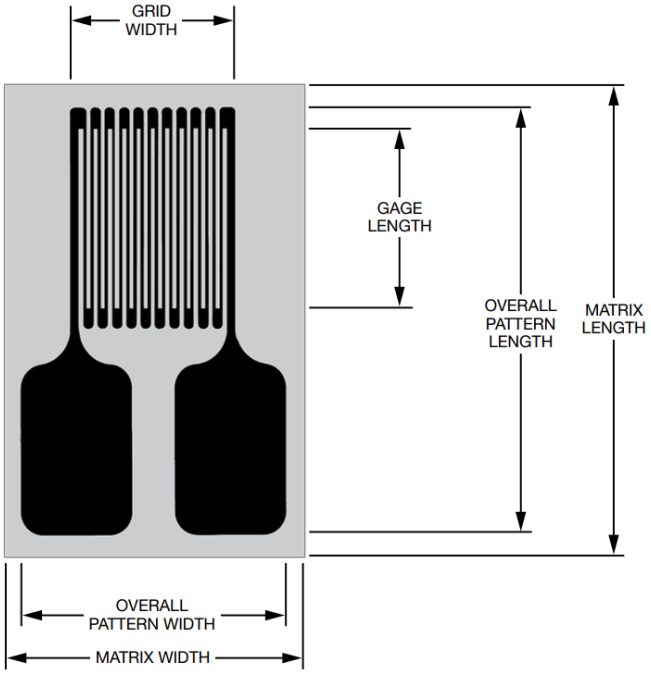


FIGURE 3.12: Strain gauge schematic. From [81]

The GF moderately depends on the temperature (≈1% relative variation over a change of 100 degrees), and was assumed constant in the calculations. However, the resistance of the strain gauge (without being adhered to a material) is also a function of temperature, owing to the temperature dependence of the grid material's resistivity. As the resistance change due to the sample's strain, ΔR_{sample}, is also small, it has to be accounted for. Thereby, the apparent change in resistance in the strain gauge, ΔR, has two contributions:

$$\Delta R = \Delta R_{sample} + \Delta R_{strain\ gauge} \tag{3.10}$$

where $\Delta R_{strain\ gauge}$ is the resistance change due to the strain gauge's temperature dependent strain (without being adhered to the material's surface).

To eliminate the $\Delta R_{strain\ gauge}$ contribution, we used two similar strain gauges, one attached to the sample and a "dummy" attached to a reference material with a well known CTE. In this work, an Alfa Aesar copper turning (99.9% purity) was used as the reference. In this way, the thermal output of both strain gauges will cancel out, and only changes in resistance due to thermal induced strain on the sample will be measured.

The strain values (and consequent changes in resistance) are typically small and are usually measured in parts per million (ppm). Experimentally, to be able to measure these

small changes in resistance, a Wheatstone bridge setup is usually implemented. The implemented circuit is represented in figure 3.13 and all the calculations are detailed in appendix B.

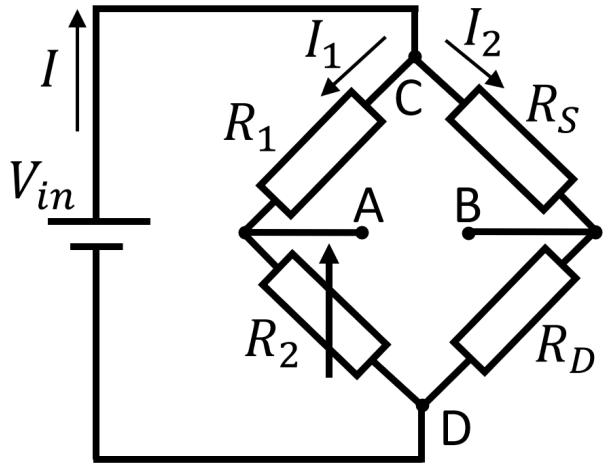


FIGURE 3.13: Wheatstone bridge schematic diagram. R_1 is a 350Ω resistance, R_2 represents the resistance of a rheostat used to achieve bridge equilibrium, R_S and R_D represent the resistances of the strain gauges mounted on the sample and dummy, respectively, and V_{in} is the supplied voltage to the circuit.

We used the micro-measurement's [82] ED-DY-031CF-350/LE (nominal resistance of 350 Ω) strain gauges for the SiO_2 samples and the initial 3D printed mortar measurements. [82] They are suitable for dynamic measurements in a wide temperature range (-195° to 205° C) and do not have self temperature compensation. One of the downsides is that its length may be too small (≈0.8 mm) and comparable to the aggregates in the mortar (up to ≈1 mm), meaning that the measurements could arise from the individual aggregates and not of the overall composite. To avoid this potential problem, the CEA-06-125UNA-350/P2 strain gauges (nominal resistance of 350Ω) were used for the rest of the samples. They have increased length (3.18 mm) and are commonly used in concrete measurements. A SK-09-031DE-350 strain gauge was also tested in one of the non-compensated mortars to assess the influence of using different strain gauge grid sizes on the mortar's CTE measurements.

The adhesive used to attach both strain gauges was the micro-measurement's M-bond AE-15. Curing was carried in a Heraeus B 5060 E incubator at 95° C for 1h and the samples had weights on top to help maintain a good bond. Due to the porosity of the mortar samples, an additional first layer of adhesive was used to fill the gaps in the samples, and subsequent abrading was carried with a 280-grit silicone carbide grinding paper to remove excess adhesive and expose the mortar's surface.

3.8 Thermal expansion measurements

The thermal expansion measurements were carried in a closed cycle cryostat from ADVANCED RESEARCH SYSTEMS [83] in The Institute of Physics for Advanced Materials, Nanotechnology and Photonics (IFIMUP), capable of reaching temperatures down to 15 K. It involves compressing and expanding helium gas based on Gifford-McMahon refrigeration cycles [84], with the help of an APD CRYOGENICS HC-4 MK1 compressor. The warmer helium exhaust vapour is recycled through the system, enabling to cut the losses of this non-renewable resource. A schematic of the system is represented in figure 3.14 and the individual components of the cryostat are represented in figure 3.15.

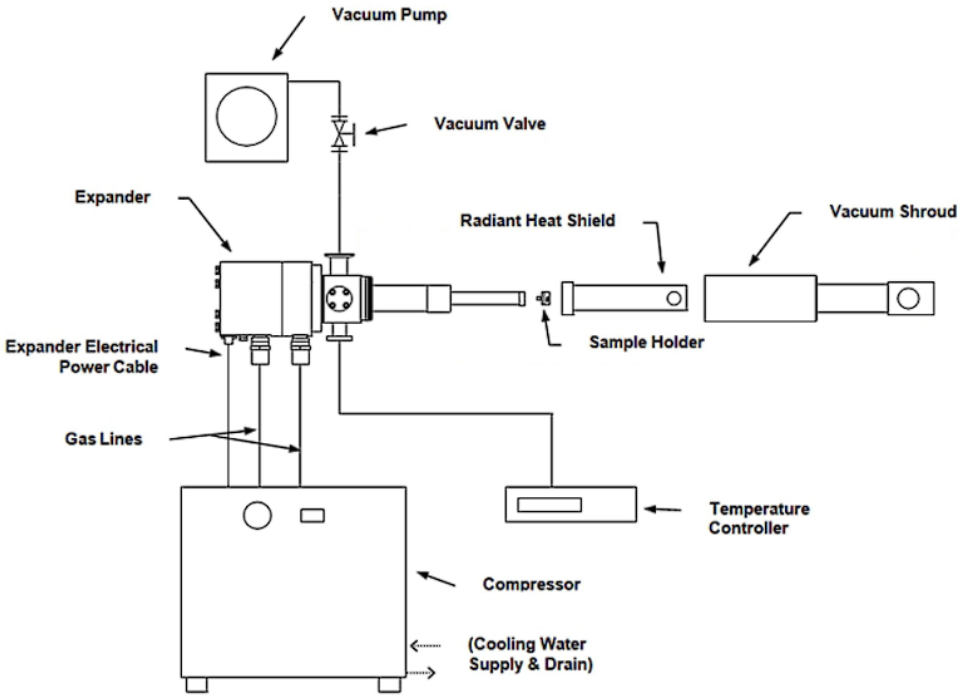


FIGURE 3.14: Schematic of a closed cycle cryocooler. Adapted from [83].

The cryogenic system contains a heater a few centimetres below the cold tip and a temperature controller with a proportional-integral-derivative (PID) controller, which balances the heating and cooling in the system by applying a corresponding voltage to the heater. Data was acquired for temperature ranges between 200 K and 340 K (-73°C to 67°C) at various sweeping rates (from 1 K/min to 10 K/min) in cooling and heating cycles.

The sample holder is a cylindrical copper block with a thread that is attached to the cryostat's cold tip. Shroud paper was placed on its surface with the help of GE-varnish,

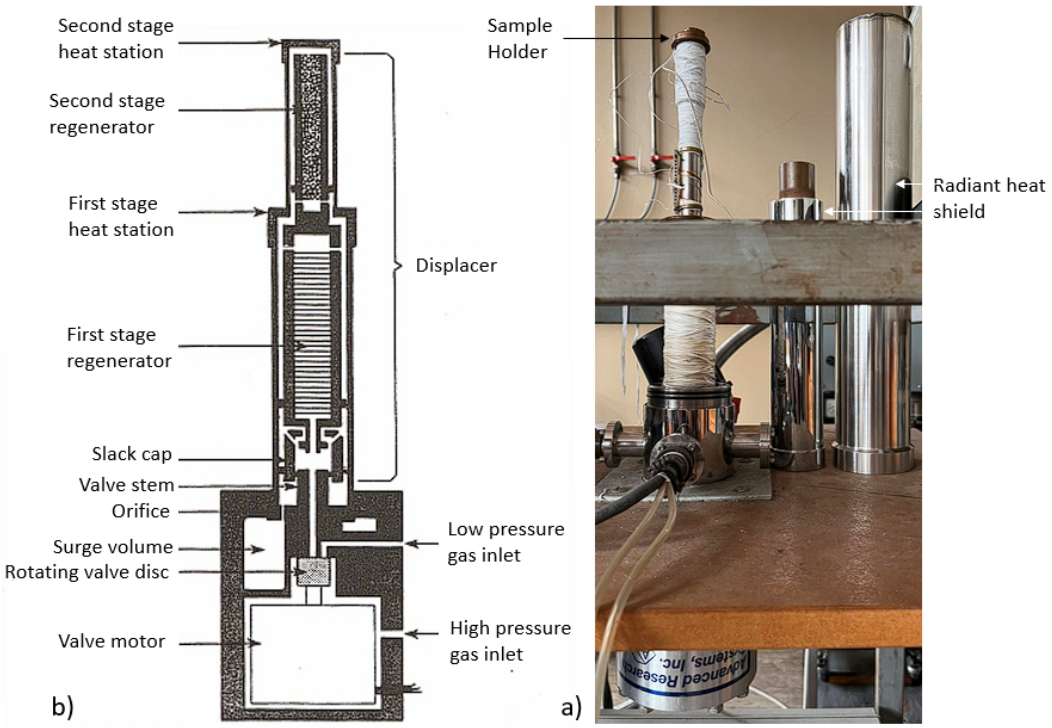


FIGURE 3.15: a) Schematic of the cryostat's individual components (adapted from [83]), and b) picture of the cryostat used.

which is a good electric insulator and good thermal conductor. The sample and Copper strip were fixated on top of the shroud paper with the same GE-varnish. On the sample holder plate, there were three connection wires to establish electrical contacts to the extremities of the strain gauges and to point B (see figure 3.13). These connections were bonded via a lead solder, including both strain gauges. A chromel-AuFe 0.07% thermocouple was sealed with indium near the sample to record its temperature. The head was then enclosed with 2 radiation shields of different dimensions and sealed under vacuum ($< 10^{-4}$ bar).

The experimental setup is schematically represented in figure 3.16. The temperature controller used was a LakeShore model 331 temperature controller. Initially an HP 34420A nanovoltmeter was used to record the voltage V_{AB} and later, a Keythley model 182 nanovoltmeter was used instead. The voltage source was supplied by a Time Electronics 5018 multi-function calibrator. The voltage in the thermocouple was measured by an Agilent 3458A digital multimeter and a calibration curve was used for temperature conversion. [85] All instruments were connected to a computer via GPIB interface and a LabView program was used to control and record all the relevant measurement parameters.

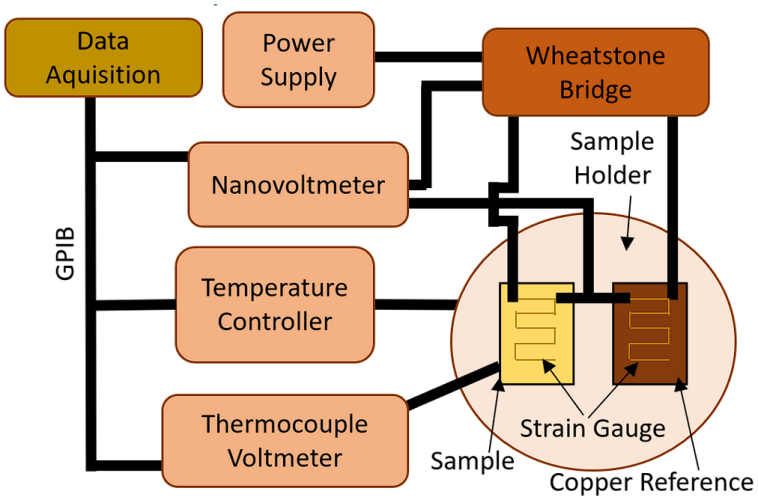


FIGURE 3.16: Experimental setup for the thermal expansion measurements.

3.9 Dilatometry

An alternative technique that is more commonly used for thermal expansion measurements is dilatometry. Strain gauges were used initially due to lack of a dilatometer, but conflicting results were obtained, as we will see in the next chapter. In hopes of explaining those results, dilatometry measurements were conducted at the University of Aveiro.

Dilatometry is a versatile and valuable technique employed in materials science and engineering to measure changes in the volume or dimensions of a material as a function of temperature, time, or applied stress. This method provides critical insights into various material properties, including thermal expansion, phase transitions, and mechanical behaviour. [86]

As is represented in figure 3.17, the core components of a dilatometer typically include a sample holder, a heating element, a temperature control system, and a displacement measurement device, such as a linear variable differential transformer (LVDT) or an interferometer. The sample is securely held within the dilatometer and subjected to a temperature change. The pushrods accompany its strain, that is monitored in the sensing region. The pushrod is typically made of invar, that has a known low CTE.

The dilatometry experiments were performed using a Linseis L75 vertical alumina dilatometer. The measurements were done between room temperature and 100 °C with a heating rate of 1K/min in flowing air (50 mL/min, relative humidity at room temperature $\approx$ 10%).

As was mentioned, between the dilatometry, XRD and strain gauge methods to measure thermal expansion, the latter was chosen because the equipment was available for

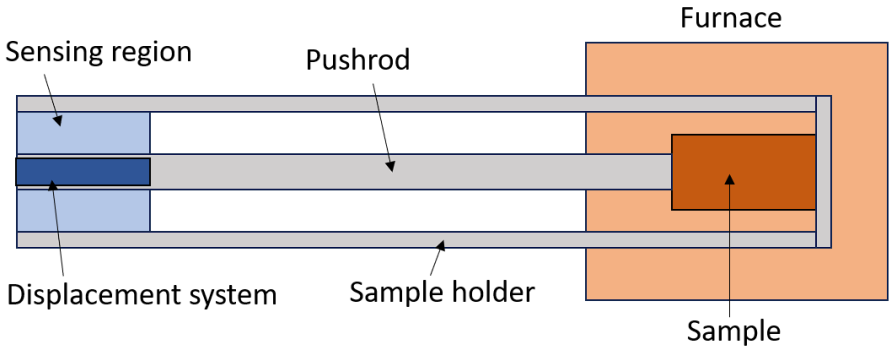


FIGURE 3.17: Simple schematic of a dilatometer, where the pushrod accompanies the sample's deformation, that is recorded by a displacement measurement device.

use, measuring in the cryostat enabled reaching sub 0°C temperatures, and it provided the required sensitivities systematically to measure the low strain values of all samples. There are a few other methods not discussed here, such as interferometry, that are discussed by Kanagaraj and Pattanayak [87]. Nonetheless, dilatometry would be preferable, due to the increased sensitivity, and direct displacement measurements. The strain gauge method implemented relies on many indirect measurements that lead to increased errors and uncertainty, as we will see in the next chapter.

Chapter 4

Results and discussion

All the results and data acquired throughout this work will be presented and discussed in this chapter. These include the composition and morphology of the the individual fillers, the non-compensated mortars, and the initial compensated mortars produced, followed by the FEA study on the factors impacting the composite's CTE, and, finally, the thermal expansion measurements of all samples.

4.1 Material composition and morphology

In this section we will layout the morphology and composition of all the samples used, obtained thorough SEM and XRD data. SEM was used to ascertain the microstructure of the materials in a more visual analysis, and to determine the chemical elements present in the samples through EDS, whereas an XRD complementary analysis allowed us to identify the distinguishable phases present in the mortar. These studies were not conducted in some samples due to lack of meaningful information that would be obtained through these analyses, because they would exhibit identical microstructures from the mortars produced manually, or simple lack of time.

4.1.1 White micro silica powder

As can be seen through the SEM micrograph in figure 4.1, the silica powder is irregular, with quartz particles exhibiting clear sharp edges. They have around 0.6 μm in size, albeit the variation is high, with some reaching up to 3.5 μm in size. An open source software, imageJ, was used for image statistical analysis, where random particles were sampled to determine the particle size distribution through a lognormal fit.

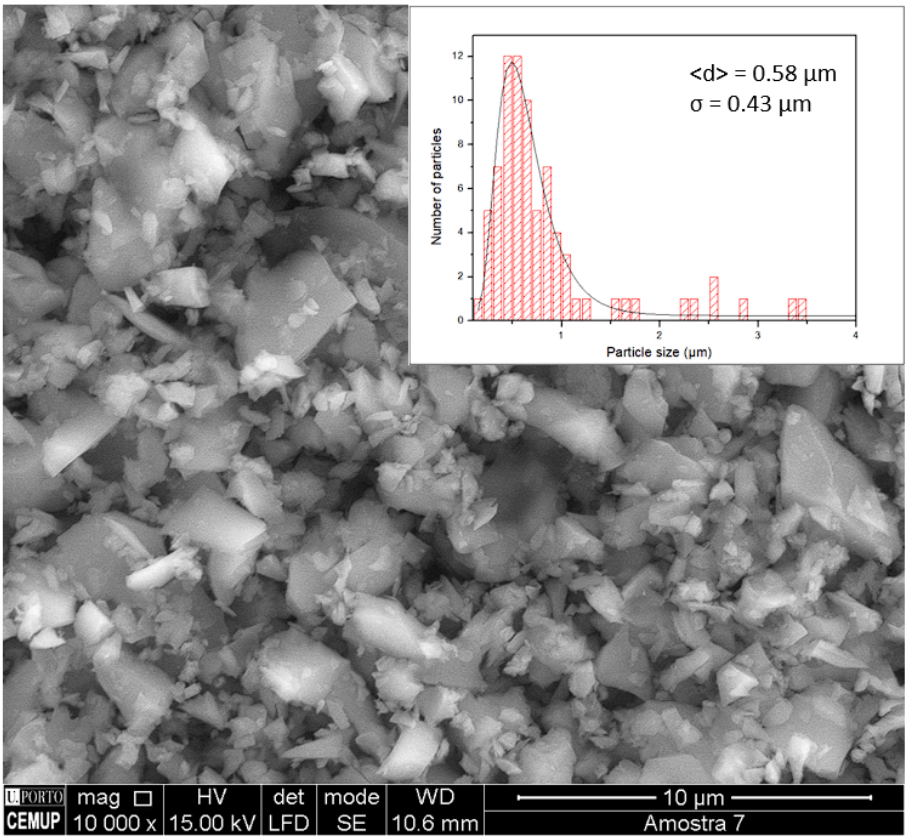


FIGURE 4.1: SEM micrograph of the silica powder and size distribution, with <d> being the average particle size, and σ the size standard deviation. Taken with a magnification of 10000x (lower left corner) using SE data.

4.1.2 Non-compensated mortar powder

We performed an XRD and SEM analysis on the non-compensated mortar, both in the non-hydrated (powder) and hydrated forms, to verify the presence of the phases and aggregates discussed in section 2.1, as well as the existence of microcracks.

SEM

Starting with the SEM analysis, it was observed from the micrographs in figure 4.2 the presence of quartz aggregates, small quantities of gypsum, and the more predominant phases C3S and C2S. Trough the EDS (see appendix C) of the overall powder sample, there was some content of aluminium and iron, suggesting the possibility of the C4A and C4AF phases being present in the mortar. Moreover, there were higher contents of carbon than usual (as the tape that holds the samples is made of carbon), possibly confirming the inclusion of some phase of calcium carbonate. This makes sense, as limestone was introduced as aggregates in this commercial mortar. [75].

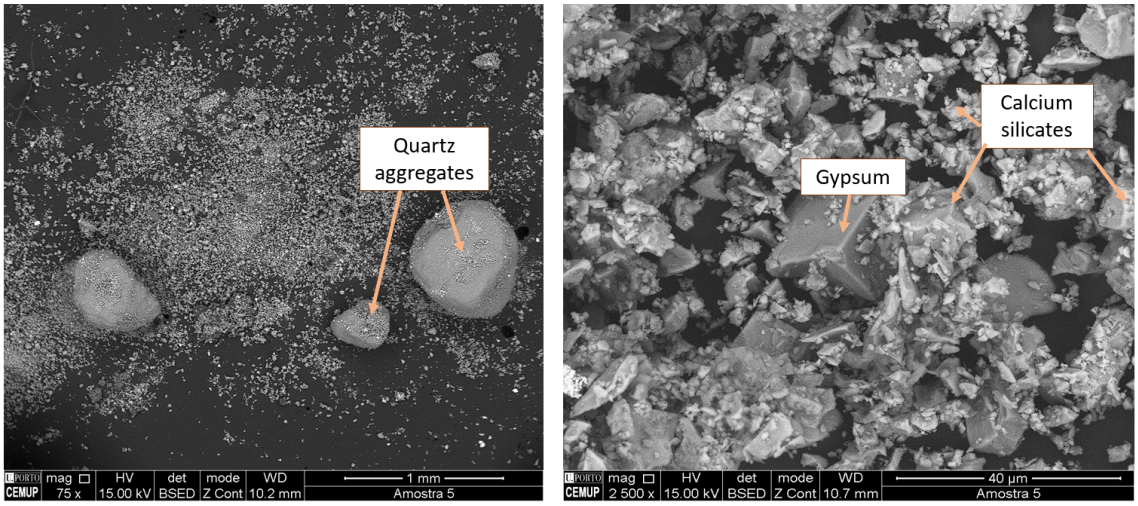


FIGURE 4.2: SEM micrographs of the mortar powder, where the calcium silicates include the C3S and C3S phases. Taken with a magnification of 75x (lower left corner) using BSE data (left) and a magnification of 2500x (lower left corner) using BSE data (right).

XRD

The XRD diffractogram of the mortar powder is present in figure 4.3a. The predominant phases C3S, C2S and quartz were identified, as well as calcium sulphate (gypsum), calcite and the other aluminate phases, with reduced content, owing to the low intensities of their corresponding peaks.

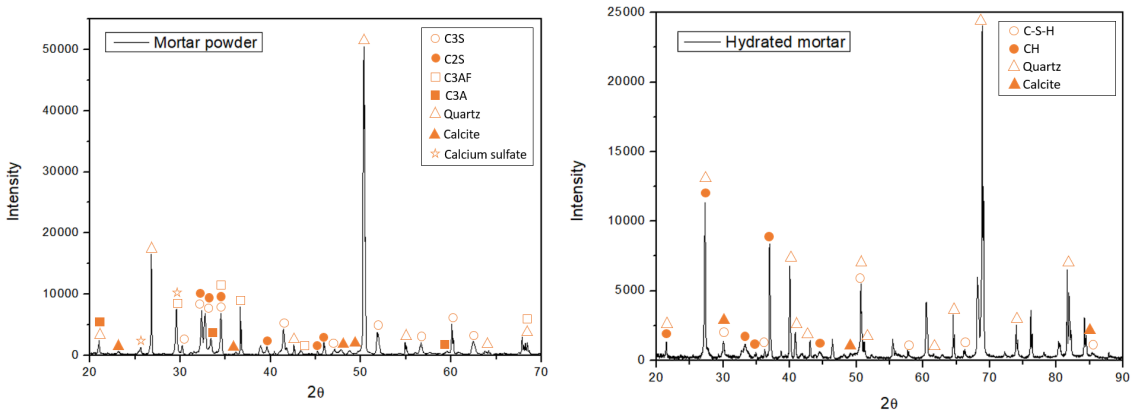


FIGURE 4.3: XRD difractograms of the a) mortar powder and b) hydrated mortar. The symbols indicate if the peak position where they are assign to matches that of the designated phases.

4.1.3 Hydrated non-compensated mortar

SEM

The SEM micrograph of figure 4.4 confirms the presence of the C-H-S and CH phases, as well as the quartz aggregates. Few quantities of calcite were also identified, as well as some unhydrated cement regions and voids. We can also clearly see microcracks, mainly in the interface between the large aggregates and the cement paste, corresponding to the ITZ. EDS showed few quantities of aluminium and sulphur, so the ettringite or mono-sulphoaluminate phases could be present, in smaller quantities.

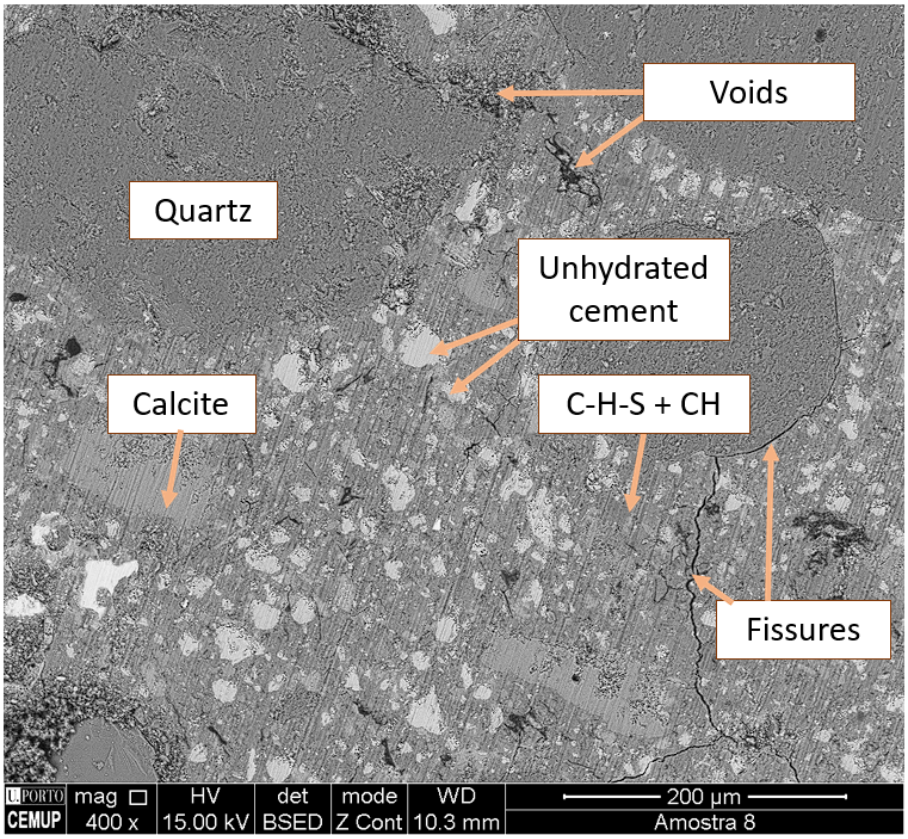


FIGURE 4.4: SEM micrographs of the hydrated mortar. Taken with a magnification of 400x (lower left corner) using BSE data.

XRD

The XRD data of figure 4.3b confirmed the presence of quartz, C-H-S, CH, and some calcite, but ettringite or monosulphoaluminate could not be clearly matched. Some peaks remained unidentified, namely at $2\theta = 61°$, $67°$ and $76.5°$.

4.1.4 Silica compensated mortar

After curing, a distinct surface layer formed around the mortar that is not representative of the bulk mortar. Thereby, this layer should be grinded if the samples are to be subjected to experimental measurements. Visual comparisons between this layer and a normal mortar sectional area can be seen in figures A.4 and A.5. The mortars compensated with silica and LaFeSi showed weak integrity and their microstructure should differ from a mortar with normal strength and good mechanical properties. Moreover, owing to their fragility, they could not be grinded when sent to SEM to be analysed. Nonetheless, their phases can still be identified, but their microstructure should be different from what is expected of a normal mortar.

The SEM micrograph of the silica compensated mortars can be seen in figure 4.5, where the micro silica is present, as well as the typical C-H-S + CH phases.

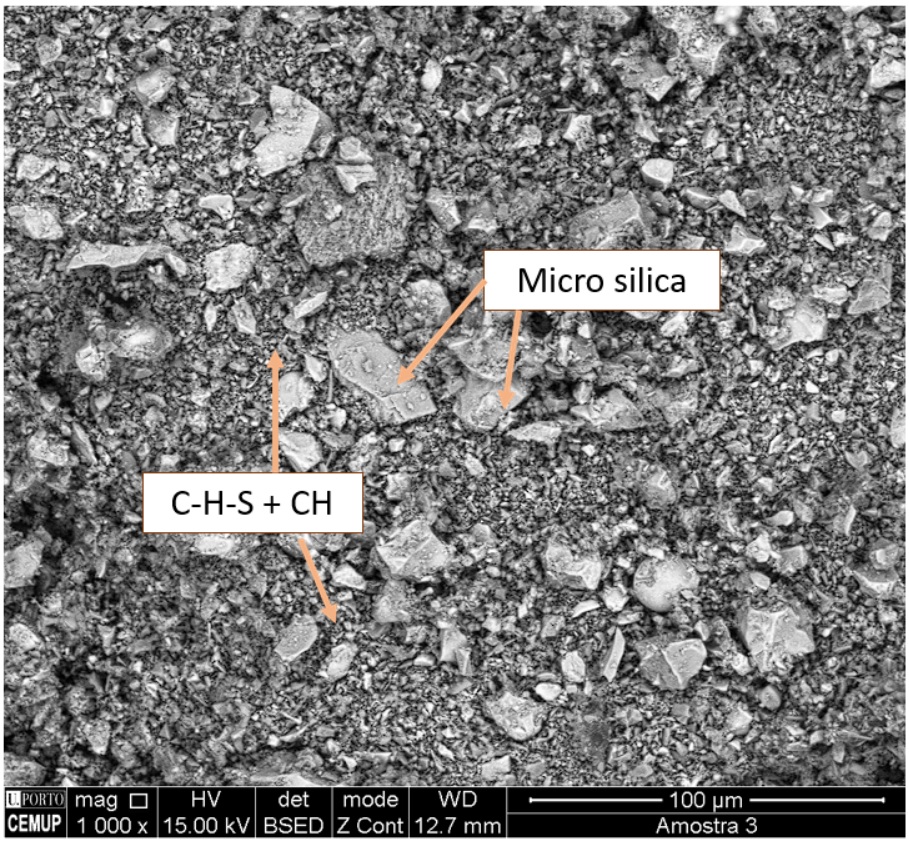


FIGURE 4.5: SEM micrograph of the silica compensated mortar. Taken with a magnification of 1000x (lower left corner) using BSE data.

4.1.5 LaFeSi compensated mortar

More detailed information about the mechanical and magnetic properties of the LaFeSi-based compound used in this work are present in [37]. The $LaFe_{11.9}Mn_{0.27}Si_{1.29}H_x$ alloy was produced via arc-melting followed by hydrogenation, and the final powder used was prepared by ball milling as described in section 3.6.

Through EDS, the atomic percentage of each chemical element present in the mortar was obtained, and the stoichiometry matched that of the powder. However, because of the hydrogen's low z number, its presence could not be detected via EDS. To study the occurrence of spontaneous (de)hydrogenation or segregation that could happen during mortar hydration [88], the magnetic properties of the compensated mortar were examined in a Superconducting Quantum Interference Device (SQUID) magnetometer (MPMS3, by Quantum Design), but no meaningful changes were observed from the original LaFeSi powder.

Through the SEM micrograph in figure 4.6, we determined that the particles had around 0.4 μm in size, similar to what was obtained by [37] (0.4 μm), thereby verifying the reproducibility of the ball milling method. We can verify again the differences in the microstructure of the non-grinded superficial layer of the mortar after curing, with the more representative interior sectional area of figure 4.7. There, we can see the presence of some agglomeration, as the alloy is ferromagnetic, contrasting with the apparent homogeneity of figure 4.6. This should pose some anisotropic challenges in the composite and is a disadvantage of using LaFeSi. Apart from it, we can also observe the presence of the C-H-S and CH phases, calcite and quartz aggregates. This analysis proved useful not only to identify the individual phases present in the samples, but also their microstructure.

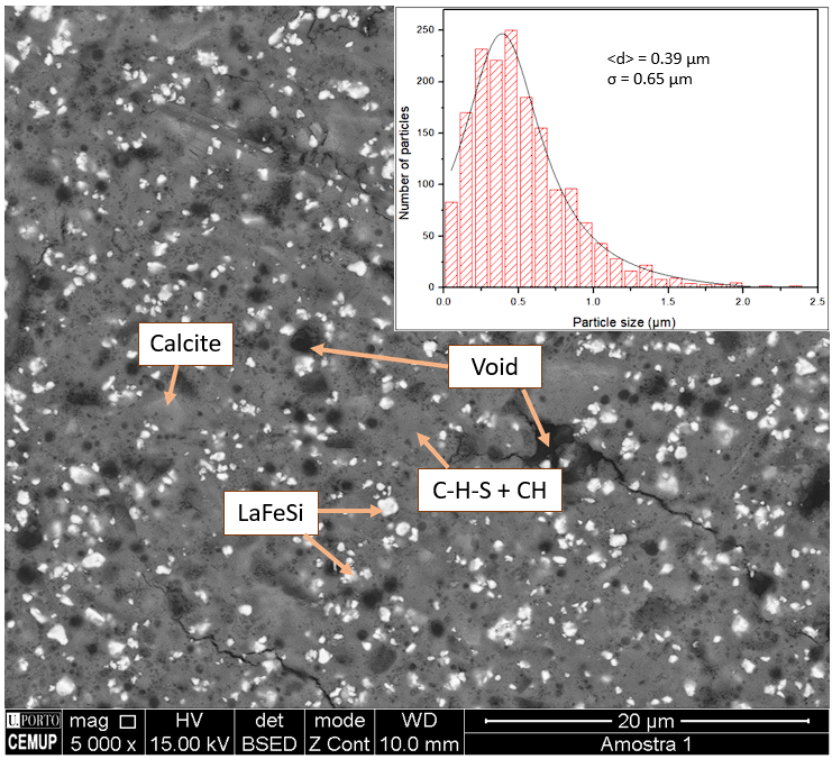


FIGURE 4.6: SEM micrograph of the non-grinded superficial layer of the LaFeSi compensated mortar and size distribution, with <d> being the average LaFeSi particle size, and σ the size standard deviation. Taken with a magnification of 5000x (lower left corner) using BSE data.

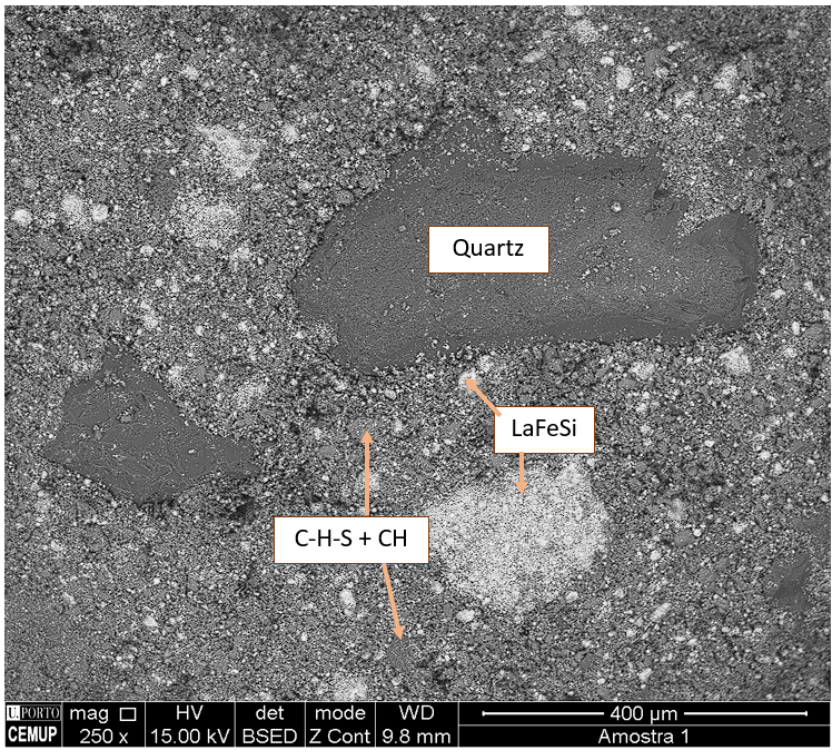


FIGURE 4.7: SEM micrograph of the LaFeSi compensated mortar, where some LaFeSi agglomeration can be seen. Taken with a magnification of 250x (lower left corner) using BSE data.

4.2 Finite element analysis

All the FEA results will be detailed in this section, including the analytical and numerical models comparison, the Taguchi study to ascertain the influence of some factors on the mortar's CTE, and a composite stress analysis.

4.2.1 Analytical model predictions and FEA simulations

In section 2.4.1 we presented the analytical models used to predict and simulate the CTE of the compensated mortars and the FEA method implementation was also thoroughly detailed in section 3.1. As was mentioned, the CTE of the composite's matrix used in these models was determined by the initial thermal expansion measurements (using strain gauges) of the mortar sample produced by 3D printing. The CTE was around 33 ppm/K and these results will be detailed in the next section.

Figure 4.8 shows the differences between models, with the Turner model giving a lower bound estimation, while the ROM model gives an upper bound. All FEA simulations yielded CTE results within these bounds.

The results of the models for the LaFeSi compensated mortars can be visualised in figure 4.8a. The CTE of LaFeSi used for the analytical models was the same as the CTE of the powder used experimentally (-112.4 ppm/K [37]). For the FEA simulations we also included other LaFeSi CTE values (-97.9 ppm/K , -104.9 ppm/K, and -112.4 ppm/K [37]), and we can clearly see the difference of using fillers with different CTEs. As expected, composites including fillers with smaller CTE have a lower CTE. From these results, it was expected that we could achieve a ZTE mortar by adding between 6.5% (Turner model) to 23% (ROM model) filler volume fractions. By relying on the FEA simulations, a ZTE composite would be achieved by adding 15% LaFeSi.

Looking at figure 4.8b, all models are closer together, given that the bulk modulus of silica (35.5 GPa) is closer to that of the mortar's (16.6 GPa). We can also observe that different amounts off particle inclusions yield similar composite CTE reductions. Increasing the particle amounts translates to smaller particle sizes to maintain the same filler volume fraction. We can then assess that the size off the particle inclusions have little effect on CTE reduction, but can have a hidden impact on CTE by factors that were not taken into account on the simulations (such as ITZs). However, they have an observable impact on the stress near the interface between the phases. This will be further elaborated later.

Given that the measured CTE of the 3D printed mortar was high (33 ppm/K), it would be hard to achieve a ZTE composite with ZrW_2O_8 inclusions, as can be seen in figure 4.8c. From figure 4.9 we can further observe this when comparing to the silica inclusions, that yield similar results. The large NTE of the LaFeSi enables the use of less filler to reduce the mortar's CTE, but can cause phase mismatch problems that lead to high stresses at the interface, as we will see later. The actual CTE value of the mortar is suspected to be much lower than was initially measured, so it could be possible to achieve a ZTE mortar with reasonable amounts of ZrW_2O_8. However, it was documented and predicted by Kofteros et al. [13] that 40% ZrW_2O_8 volume fraction would lead to a ZTE composite, which still represents a significantly high fraction. .

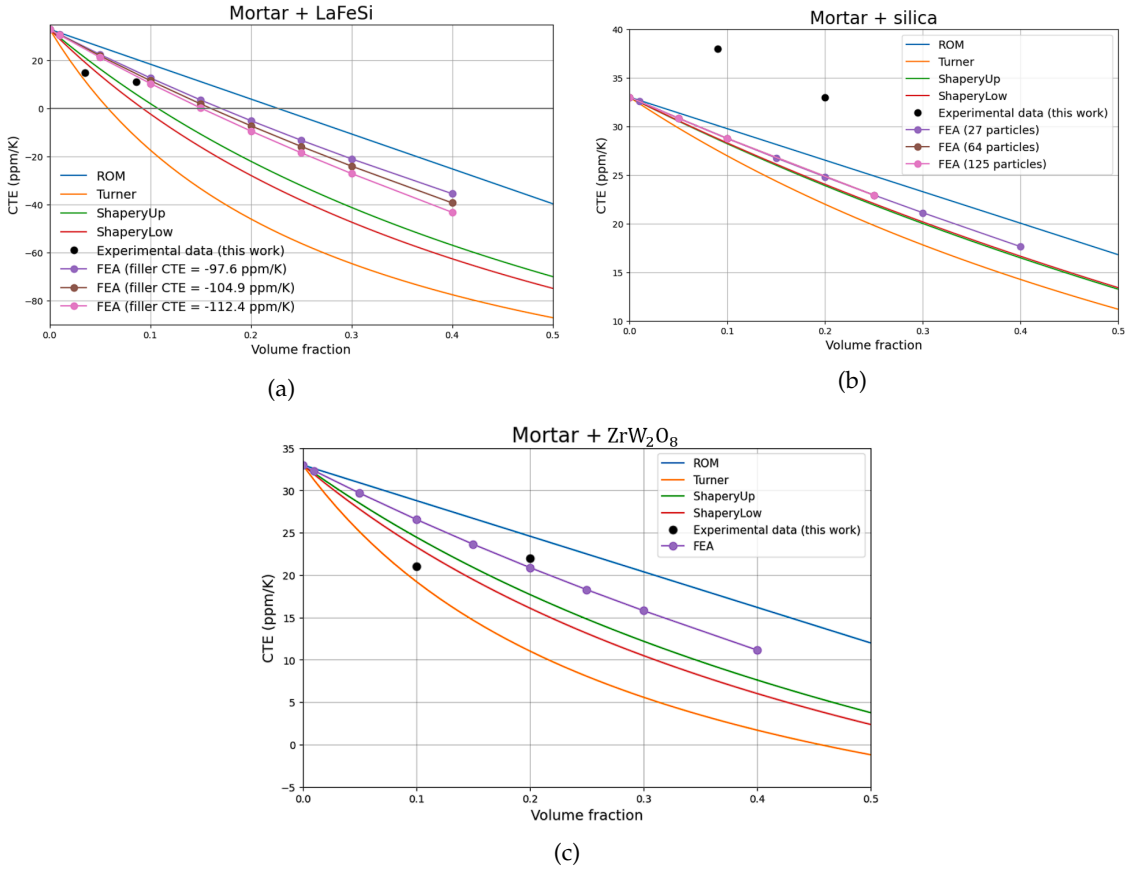


FIGURE 4.8: Analytical and numerical model comparison for the compensated mortars with a) LaFeSi, b) SiO_2, and c) ZrW_2O_8.

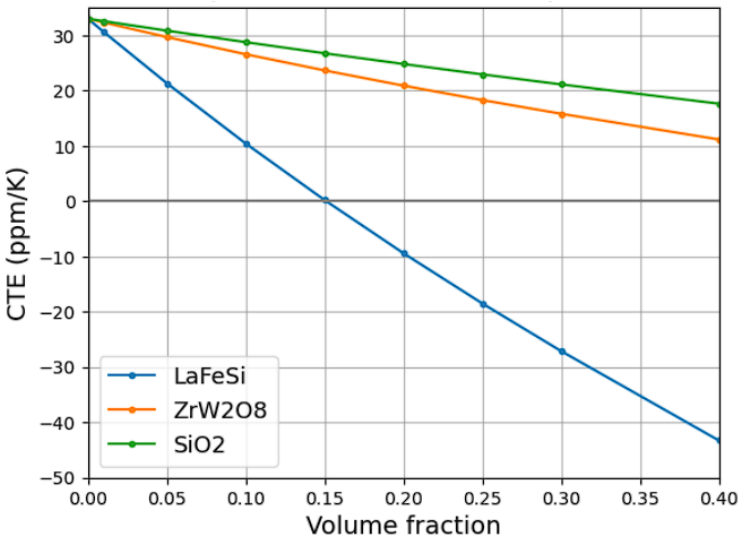


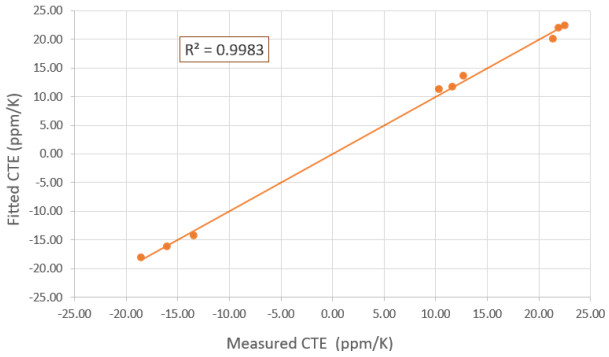
FIGURE 4.9: FEA comparison of different compensated mortar's CTE for different filler volume fractions.

4.2.2 Taguchi analysis on the mortar's CTE

Using the setup detailed in section 3.2, and simulating every experiment of the orthogonal array of figure 3.4 in COMSOL Multyphisics, we obtained the multivariate least square fitting in equation 4.1, giving a good linear relation between the results and the predicted CTE using the multivariate analysis (see figure 4.10). In equation 4.1, we can see the weight of each variable on the mortar's CTE. It can be used to determine which %filler should be added if we wanted a certain CTE in the mortar, given the CTE of the filler and the amount of particles.

$$\text{CTE} = 0.0104 \cdot \text{particle amount} + 0.1933 \cdot \text{filler CTE} - 1.8804 \cdot \%\text{filler} + 50.4607 \quad (4.1)$$

The volume fraction of filler has by far the largest impact, with higher %filler values giving lower mortar's CTE. This is also evident from the correlation matrix (see figure 4.10), where the amount of particles included and the filler's CTE both have little effect, with the latter having a slight more meaningful impact (as can also be seen from figure 4.8). As expected, the lower the filler's CTE, the higher the reduction on the mortar's CTE will be. Increasing the amount of particles, that can also be translated to decreasing the particle size in the matrix, also leads to a slight increase in the mortar's CTE.



Correlation matrix

	Particle amout	Filler CTE (ppm/K)	% filler
P	0.026	0.073	-0.996

FIGURE 4.10: Comparison between the multivariate least square fitting of the mortar's CTE and the measured CTE (left), and correlation matrix (right), where the P value ($\in [-1, 1]$) represents the correlation between the factors and the CTE of the mortar. Higher magnitudes represent stronger correlations and the sign indicates whether the variable decreases (negative P value) or increases (positive P value) the mortar's CTE.

4.2.3 Stress analysis

The factors included in the previous study not only affect the mortar's CTE, but also have an impact in other mechanical properties of the mortar. To better understand other influences of these factors on the composite, a simple stress analysis will be conducted in this section. This study provided more insight on the interactions between the phases, in particular in the interface between aggregate and matrix. Note that the von Mises stress scale is the same throughout this analysis.

First, a comparison between the different fillers used was made, by using the same amount of particle inclusions and a filler volume fraction of 15%. We can see from figure 4.11 that the LaFeSi compensated mortars have a more pronounced stress distribution compared to the other fillers, given its large CTE mismatch ($\text{CTE}_{mortar} = 33$ ppm/K and $\text{CTE}_{LaFeSi} = -112.4$ ppm/K). The more fragile areas are around the interface between the aggregate and the matrix as would be expected.

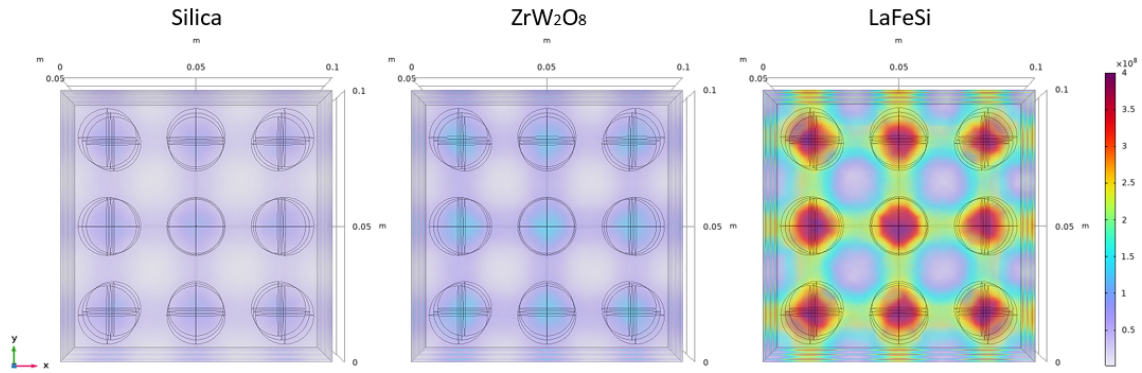


FIGURE 4.11: Stress comparison of different mortar compositions. 27 particles were included and the composites have 15% filler volume fraction.

From figure 4.12, we cannot observe significant differences from the amount of particles introduced, and the highest stress remains focused around the interface, however it is more uniformly distributed.

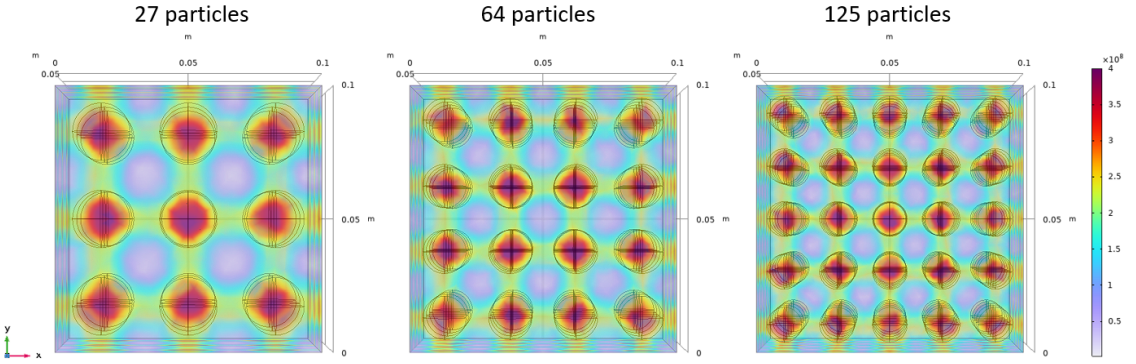


FIGURE 4.12: Stress comparison for different amount of particle inclusions in the 15% LaFeSi compensated mortar.

In figure 4.13 we can clearly see that increasing the filler volume fraction also increases the stress drastically. In order to ascertain if this would pose meaningful mechanical integrity problems in the composite, thorough mechanical properties measurements should be conducted.

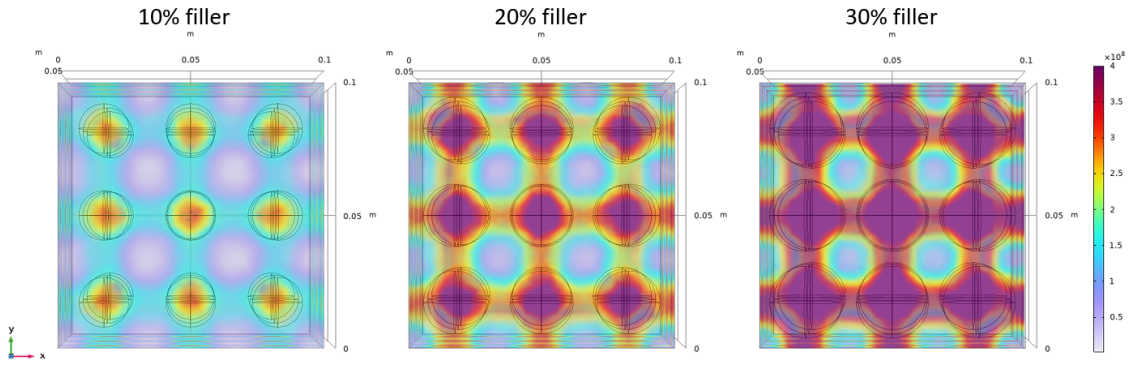


FIGURE 4.13: Stress comparison for different filler volume fractions in the LaFeSi compensated mortar with 27 particle inclusions.

From these simulations, conclusions cannot be made regarding the composite's mechanical properties. To further study them, strength and other mechanical measurements must be performed. Nonetheless, clear interactions between aggregate and matrix can be observed for different composite's configurations and properties.

4.3 Thermal expansion measurements

In this section, in order to better understand the thought process behind each thermal expansion measurement, each one will be presented in chronological order. It will start from the 3D printed mortar sample from which all the FEA was based on, continuing to each compensated mortar sample, and later to the dilatometry measurements. In the end, a discussion will be made in order to try to explain the observed results, as well as some suggestions to improve the thermal expansion measurement procedures. An image of some of the samples is present in figures A.3 and A.4.

4.3.1 Initial 3D printed mortar sample

As already mentioned, the first measured sample was a Saint-Gobain Weber 3D 160-1 pre dosed mortar. It was 3D printed on a SMART 3D printer in the structures laboratory on the Civil Engineering department of University of Porto. The CTE obtained from the thermal expansion measurements from this sample was the one considered in the FEA. Initially, it was a large piece (≈20 cm), similarly to what can be seen in figure 1.2. A smaller bit of the mortar was then taken from it, that was later grinded down to the desired shape (parallelepiped) and dimensions (≈10x8x4 mm) using a 120-grit silicone carbide grinding paper.

Thermal expansion could be determined by using different methods. The one that was considered is explained in appendix B and uses the slope of the linear curves of the strain as a function of temperature (see figure 4.14). One could consider only the variation of strain in the extremities of the curves (see figure 4.14) with the following equation:

$$\mathrm{CTE}_{Extremities} = \frac{\epsilon}{\Delta T} = \frac{L_{350} - L_{250}}{L_{250}} \cdot \frac{1}{100} \tag{4.2}$$

Additionally, a point by point calculation corresponding to the derivative of the curve (see equation 2.4) could be considered, where an average of the obtained values would determine the thermal expansion. These methods are compared in figure 4.14, with the slope method providing less variation and mean errors.

The results of the CTE of the mortar for different heating rates are summarised in figure 4.15. Heating cycles were the only ones considered to determine the CTE in this sample, because something happened during the cooling cycles, as can be seen in figure 4.15 by the example of the 3 K/min run. For future measurements this behaviour was

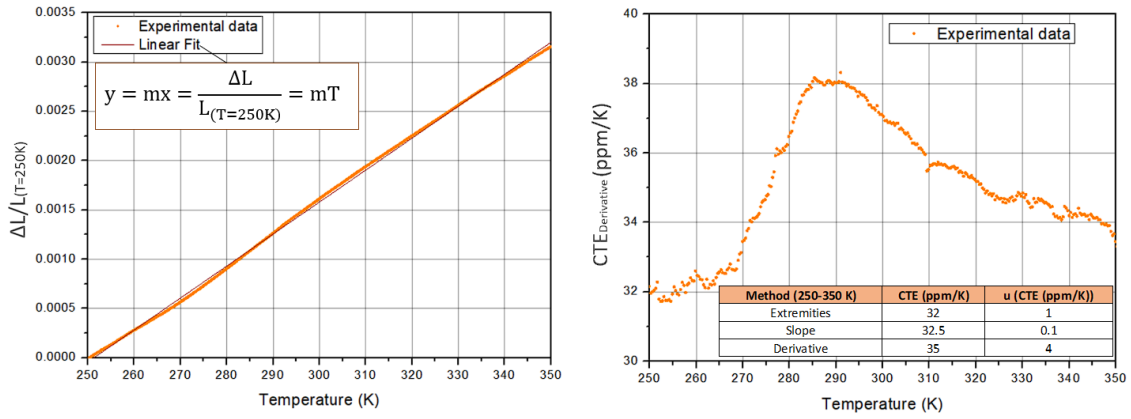


FIGURE 4.14: Strain as a function of temperature (left) and CTE (derivative method) as a function of temperature, with a comparison between the slope, extremities and derivative methods (right).

avoided, as it was likely a problem with the protocol implemented for cooling cycles during the initial measurements. Nonetheless, we can see a close agreement for different heating rates, with higher ones yielding slightly lower CTE values. The final CTE considered was an average of the CTE from these curves. The same protocol was followed for the rest of the samples.

It should be noted that a CTE of 33 ppm/K for mortar is quite high, in comparison with typical literature data where values ranging from 7 to 15 can be found [89–91]. There is no concrete explanation for these results, but some sort of error could have been made throughout the experiments, taking into account the complexity of the system and all the components involved. Some possible reasons will be further discussed in section 4.3.7.

4.3.2 Micro silica compensated mortars

A summary of the measurements conducted in the SiO_2 compensated mortars is presented in figure 4.16. As expected, the CTE for the composite with less silica volume fractions (9%) yield the highest mortar CTE (38% compared to 33% of the mortar with 20% SiO_2). However, it was expected that both had CTEs lower than the non-compensated mortar (33 ppm/K), but this was not the case. It would appear that adding silica content increases the CTE of the mortar, which is not in agreement with the analytical models nor the FEA (see figure 4.8b). The differences are relatively high, especially in the 9% compensated mortar. This could be explained by the different methods used to produce the mortars, between 3D printing and manually produced. Additionally, the measurements were conducted at different mortar ages. The ones compensated with silica were

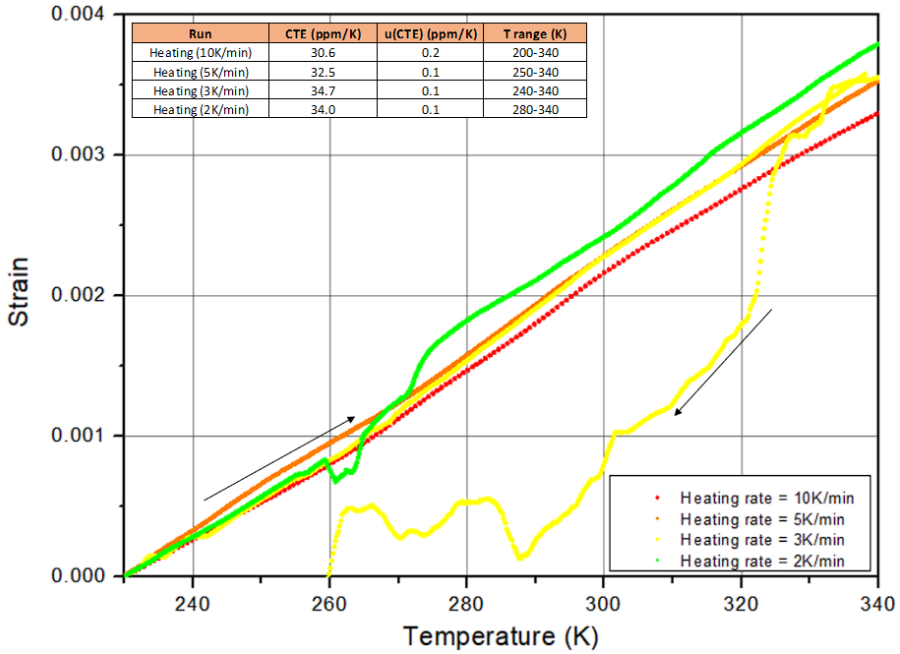


FIGURE 4.15: Strain versus temperature measurements of the original 3D printed mortar for different heating rates. Arrows indicate if the measurement was done on heating (pointing to the right) or on cooling (pointing to the left).

measured around 3 weeks after being produced, and the 3D printed mortar had over a month. As was mentioned, mortar continues to cure for long periods of time, and there is evidence that the CTE increases slightly at early stage ageing [92], but also the opposite has been reported [93]. Nonetheless, for old age samples, like the ones used, the change in CTE should have stabilised, but it is important to keep in mind that the age for the other compensated mortars was lower ($\approx$ 1 week). Moreover, the same ED-DY-031CF-350/LE strain gauge was used for the 3 samples. This could have not been the best choice, considering the size of the strain gauge (0.79 mm) compared to the aggregates in the composite (up to $\approx$1 mm). The aggregates could have been large enough that if the strain gauge was adhered to one larger particle, the measured CTE could be representative of a single particle and not the bulk material. This should not yield CTEs as high as the ones obtained (38 ppm/K and 33 ppm/K), because the CTE of the larger aggregates should be around 10 to 14 ppm/K [94], assuming that they are from some kind of quartzite rock. Nonetheless, this could have affected the results in some way. To circumvent this potential problem, larger strain gauges (3.18 mm) were chosen for the following experiments. Trying to maintain all the experimental variables the same throughout the experiments proved difficult with this setup. There were a lot of connections involved in the circuit, including wires that had a bit of leeway and could budge or move out of place when

exposed to low vibrations (see figure B.1), hindering the results.

In figure 4.16a we can see the differences of making the measurements on heating and cooling cycles. For that experiment in particular, there is a large hysteresis, in part developed by the relatively high heating rates applied, creating a temperature lag between the sample's actual temperature and the thermocouple controlled temperature. This behaviour is exemplified and explored in appendix D.1. Moreover, it seems that cooling cycles yielded lower CTE values.

In figure 4.16b we observe the opposite regarding the dependence of the CTE with the heating rate applied. Unlike the compensated mortar, these results show a slight increase in CTE for increasing heating rates.

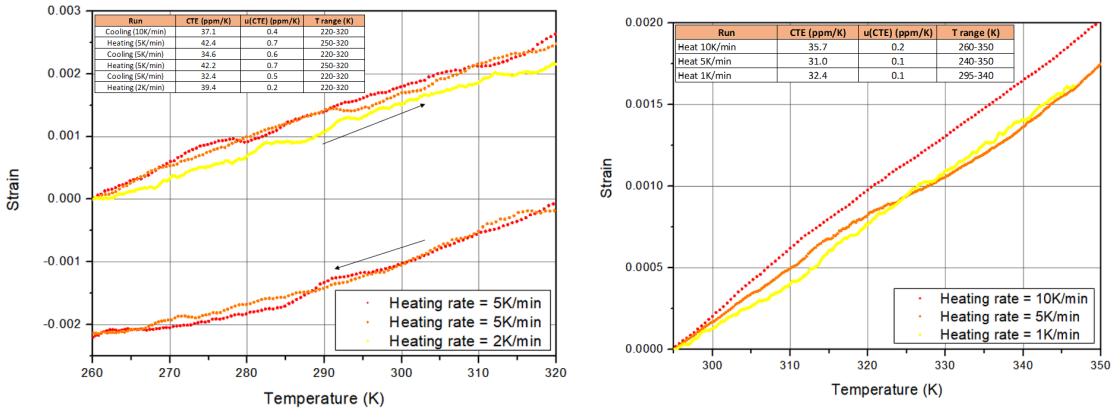


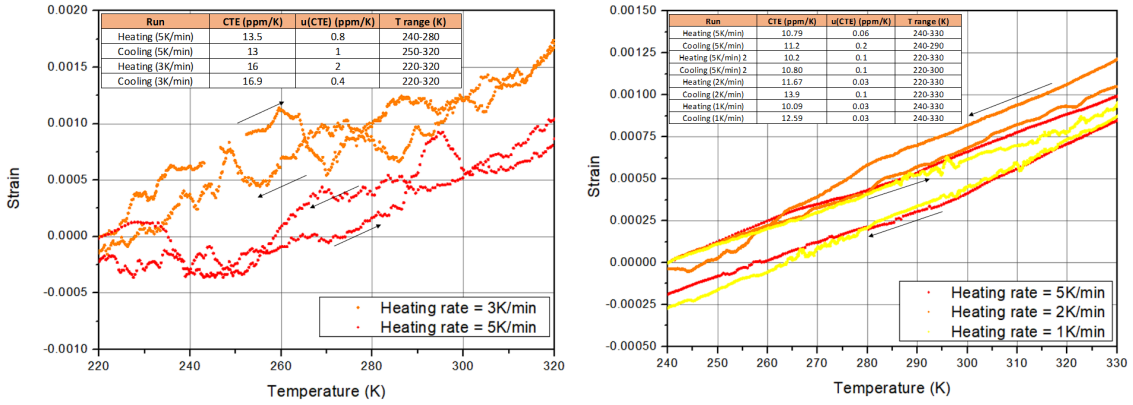
FIGURE 4.16: Strain versus temperature measurements of the a) 9% and b) 20% $Si0_2$ compensated mortars for different heating rates. Arrows indicate if the measurement was done on heating (pointing to the right) or on cooling (pointing to the left).

4.3.3 LaFeSi compensated mortars

For these samples, the strain gauge used had a larger grid size and was a CEA-06-125UNA-350/P2. Firstly, it should be noted that a few problems arose, prior to measuring, that could have impacted the results. For the 3.5% compensated mortar, the strain gauge appeared to have not adhered properly to the mortar's surface, as well as the copper reference. This may have occurred due to low applied pressure during curing of the adhesive, as the weights did not apply a uniform force throughout the surface. Strain could still be measured, but the signal had a lot of noise, as we can see in figure 4.17a. As for the 8.6% compensated mortar, it had week integrity and its surface could not be grinded and smoothed for strain gauge bonding. The solution was to place the sensor in

the smooth superficial layer formed during curing, which can be seen in figure A.5. This is not ideal, as this layer is not representative of the bulk material. However, from figure 4.17b, the results were consistent and showed low variation compared to the other sample. Additionally, the results (15 ppm/K for the 3.5% LaFeSi compensated mortar and 11 ppm/K for the 8.6% LaFeSi compensated mortar) agree relatively well with the predictive models (see figure 4.8a), assuming a non-compensated mortar CTE of 33 ppm/K.

The hysteresis is less predominant in these samples and doesn´t seem to relate to the heating rate applied. In figure 4.17b, cooling cycles show higher CTE values, as opposed to what was observed in figure 4.16a.



(a) (b)

FIGURE 4.17: Strain versus temperature measurements of the a) 3.5% and b) 8.6% LaFeSi compensated mortars for different heating rates. Arrows indicate if the measurement was done on heating (pointing to the right) or on cooling (pointing to the left).

4.3.4 Zirconium Tungstate compensated mortars

Both ZrW_2O_8 samples used for this study were made at the same time and were subjected to the same curing conditions (room temperatures with no humidity control). Moreover, their measurements were conducted less than a week apart from each other. This could have reflected the results obtained in figure 4.18. The 10% and 20% compensated mortars yielded similar CTE values (21 ppm/K and 22 ppm/K, respectively), and are within the bounds of the predicted simulations (see figure 4.8c). However, this should not be the case, as more filler should reflect more reduction in the mortar's CTE. The one with higher filler volume fraction exhibited a slightly larger CTE.

Regarding the dimensional relaxations that were already observed previously, the hysteresis seems to be more pronounced as the heating rate is increased, as we can see in

figure 4.18a. This correlation is less verifiable in figure 4.18b, and the run with 2 K/min exhibited a very low hysteresis. Apart from it, both samples had the lowest variation between runs of all other samples measured (less than 2 ppm/K). Again, this could be a reflection of both being subjected to the same treatment on the same period, adding the fact that both were mechanically stable and the strain gauges appeared to have adhered well to the mortar's surface.

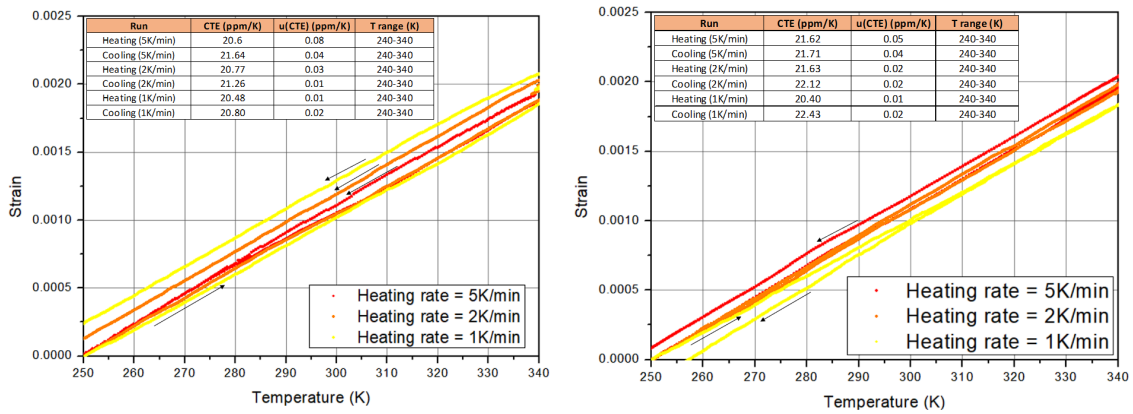


FIGURE 4.18: Strain versus temperature measurements of the a) 10% and b) 20% ZrW_2O_8 compensated mortars for different heating rates. Arrows indicate if the measurement was done on heating (pointing to the right) or on cooling (pointing to the left).

4.3.5 Manually produced (MP) mortars

In hopes of understanding if there were differences in the CTE of the 3D printed mortar and the manually produced (MP) mortar, it was decided to do the latter. Throughout this work, "MP mortar" will refer to the non-compensated manually produced mortar. Additionally, to study if there were differences in using different strain gauges with different sizes, two strain gauges, one larger (3.18 mm) than the other (0.79 mm), were used in the same sample.

From figure 4.19a, we obtained CTE values (10 ppm/K) close to what is excepted from the literature (between 7 ppm/K and 15 ppm/K), but which contrast the results obtained thus far. Different heating rates yield similar results, and there is little hysteresis, even for higher heating rates. From figure 4.19b, by comparing different installed strain gauges, the CTE values are similar (≈10 ppm/K) and show good agreement. The strain gauge SK-09-031DE-350 yielded less noisy results, but is not indicative that it is a superior strain gauge that yields more accurate strain values and increased sensitivity. The difference

is mostly related to the quality of adherence of the strain gauges to the surface, or if the measuring system was better assembled.

The difference in CTE from previous measurements is difficult to explain. These should be the expected CTE values of a mortar (≈10 ppm/K), as opposed to the 33 ppm/K obtained prior and used for the simulations. Nonetheless, even if the CTE was wrongly determined, the simulations on the influence that various factors would have on the mortar's CTE still provided insightful information, and should not be disregarded. While the results would be slightly different, the analysis and conclusions would be similar.

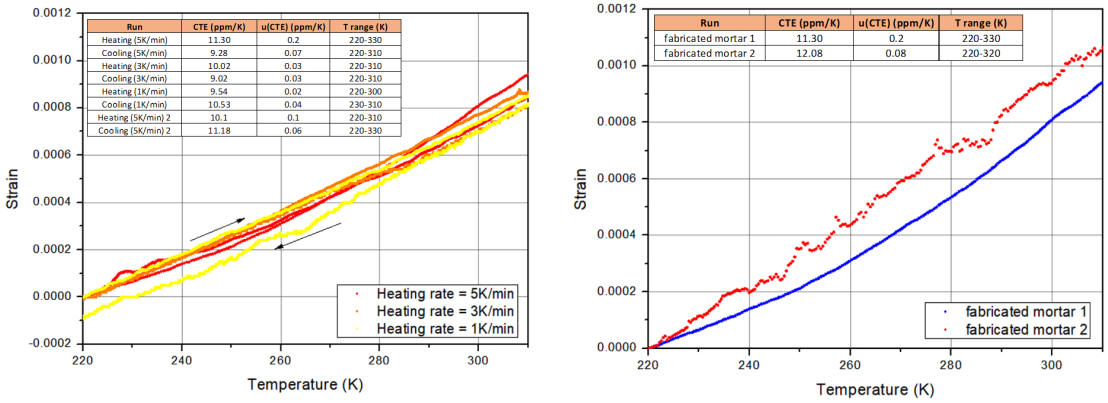


FIGURE 4.19: Strain versus temperature measurements of the MP mortar installed with a a) SK-09-031DE-350 strain gauge for different heating rates and b) a CTE comparison between the mortar installed with a SK-09-031DE-350 and CEA-06-125UNA-350/P2 strain gauges for a 5 K/min heating rate on a heating cycle. Arrows indicate if the measurement was done on heating (pointing to the right) or on cooling (pointing to the left).

4.3.6 Dilatometry measurements

To try to investigate further the impact of the measuring technique, dilatometry measurements were conducted on a few of the same samples used in the strain gauge measurements. 3 runs were made for each sample with a 1 K/min heating rate. The results are summarised in figure 4.20 and additional individual sample data is present in appendix D.2. Contrary to what was observed in the strain gauge measurements, all the samples exhibit similar CTE values (≈6.5 ppm/K), which is not to be expected. Even when comparing both the LaFeSi samples, the one with less volume fraction (3.5% compared to 8.6%) of LaFeSi has a lower CTE (6.30 ppm/K and 7.10 ppm/K, respectively). More filler should mean a more pronounced CTE reduction on the filler, and not the opposite, as all

the three compensated samples exhibit a larger CTE than both non-compensated mortars (>6.07 ppm/K). The overall CTE was around 6.5 ppm/K which is still slightly below the expected mortar CTE values found in the literature.

There is a clear hysteresis in the heating/cooling cycles for the samples. Moreover, something unusual happened during the first runs of all samples (see figure D.2), that does not correlate with the next two similar runs. No observable differences in the mortar structure were detected, but there could have been changes in the microstructure. These phenomena could have happened due to the prehistory of the samples, as all of them were subjected to previous thermal cycling, some reaching as low as 20 K [95]. The multiphase composition of the mortar could induce all kinds of complex behaviours and the microstructure of each sample can be very different. Moreover, some of them had weak integrity and were fragile, as was mentioned. However, all the samples show the exact same behaviour, which is quite odd. The measurement procedure could have originated these effects or even the mortar itself could have predominant properties that change very little when filler is included. More filler quantity could be added to generate more prevalent changes in the CTE values of the samples.

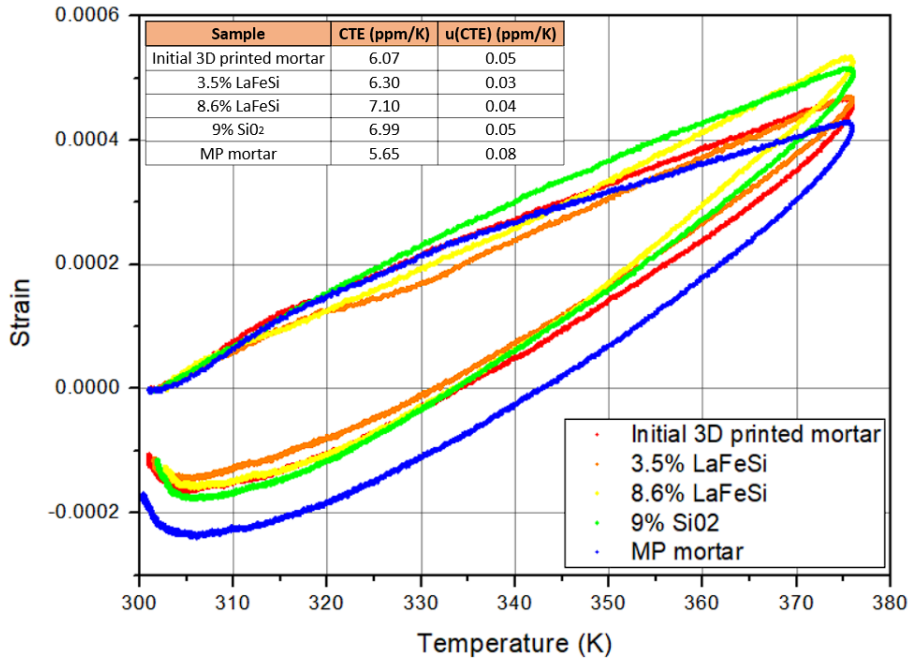


FIGURE 4.20: Strain versus temperature measurements using the dilatometry method.

4.3.7 Discussion

A summary of all the results obtained, as well as the strain gauge and thermal expansion method used for each case is present in figure 4.21. There is a slight coherency in the strain gauge results, assuming a mortar CTE of 33 ppm/K, which, by itself, is also a peculiar result, considering the usual mortar CTE values (from 7 ppm/K to 15 ppm/K). Moreover, looking at the strain gauge measurements of all three compensated mortars, the ones with lower CTE succeed more in reducing the mortar's CTE, as would be expected. However, the dilatometry measurements yield similar CTE values (≈6.5 ppm/K) between all samples (compensated and non-compensated mortars), and are not in agreement with the previous results.

The major factors that could have affected the results include the way the mortar was produced (regarding curing conditions, composition, and fabrication method), which is what determines the mortar's mechanical properties. Curing conditions such as time, temperature and relative humidity can impact the final mortar's strength [1, 27]. Guaranteeing a good homogeneity in the mixes is also paramount, as well as controlling the amount of air trapped within the mortar by vibrating the mould. The age of the mortar when making the measurements also affects the CTE value. Different methods of fabricating the mortar can impact the mortar's porosity. Producing the mortars manually and vibrating to expel trapped air bubbles, especially at low quantities, will naturally make the mix more compact and with less porosity, compared to 3D printing, which is a more autonomous method. It is reported that higher porosity decreases the CTE of mortars (from 11.7 ppm/K to 9.5 ppm/K for total porosity ranging from 26% to 32.5%) [26], so it would make sense that the CTE values obtained for the majority of the samples would be higher than the 3D printed mortar (33 ppm/K), as they were produced manually. This is true when comparing the higher CTE results (33 ppm/K and 38 ppm/K) in the silica compensated mortars, but all other results contradict this statement. However, porosity only contributes slightly to the CTE changes, assuming that the differences in porosity between the manual and 3D printed methods are also small, and do not explain the discrepancies between results.

Some samples were subjected to temperatures as low as 20 K for several hours. Extreme thermal cycling could also have impacted the performance of the mortar. At lower temperatures, the water contained in the mortar transforms into ice, which expands upon cooling. Conversely, upon thawing, the contraction is smaller and more rapid in relation

Sample	CTE (ppm/K)	u(CTE) (ppm/K)	T range (K)	Strain Gauge/method
Initial 3D printed mortar	33	3	240-340	ED-DY-031CF-350LE
3.5% LaFeSi	15	3	240-330	CEA-06-125UNA-350/P2
8.6% LaFeSi	11	2	240-330	CEA-06-125UNA-350/P2
9% SiO_2	38	8	260-320	ED-DY-031CF-350LE
20% SiO_2	33	4	240-340	ED-DY-031CF-350LE
10% ZrW_2O_8	21	1	240-340	CEA-06-125UWA-350/P2
20% ZrW_2O_8	22	1	240-340	CEA-06-125UWA-350/P2
MP mortar 1	10	2	220-320	SK-09-031DE-350
MP mortar 2	10	3	230-310	CEA-06-125UNA-350_P2
Initial 3D printed mortar (Dill)	6.07	0.05	300-370	Dillatometry
3.5% LaFeSi (Dill)	6.30	0.03	300-370	Dillatometry
8.6% LaFeSi (Dill)	7.10	0.04	300-370	Dillatometry
9% SiO_2 (Dill)	6.99	0.05	300-370	Dillatometry
MP mortar (Dill)	5.65	0.08	300-370	Dillatometry

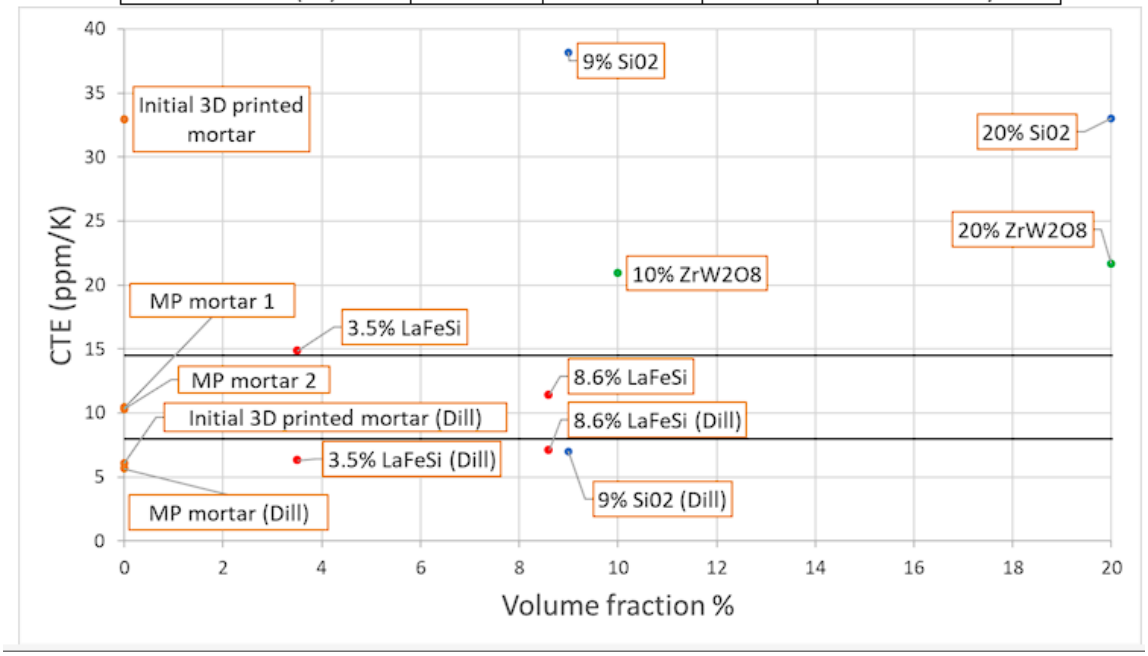


FIGURE 4.21: Summary of the thermal expansion measurements of all samples. The black lines in the graphic represent the literature range of reported mortar CTE values. The values differ depending on moisture, aggregate fractions and types, heating cycles, mortar age, amongst others [89–91]. Both MP mortars refer to the same sample, but the measurements were conducted with different strain gauges. Dilatometry measurements are tagged with "Dill" after the name of the sample

to the initial expansion, and may damage the mortar's microstructure [95, 96]. The effects of the damage also depends on heating the rates applied, the shape of the sample, and other curing and fabrication factors [95]. It has also been reported that the hysteresis obtained in the measurements could happen due to moisture distribution changes [97] and time dependent dimensional changes, such as creep and shrinkage [98]. The AASHTO protocol suggests that consecutive runs on cooling and heating cycles should be made, until values within 0.3 ppm/K are achieved between consecutive runs [99].

Additionally, the quality of the bond between the strain gauge and sample surface has

to be accounted for. Proper adhesion is crucial for reliable measurements, and requires some skill and experience. The surface of the sample also needs to be very smooth to ensure good bonding. It is suspected that the LaFeSi could have been affected by one of these reasons. Moreover, the choice in the strain gauge used, especially when it comes to its size should be accounted for. The ones that were used in this work may have been too small (from 0.79 to 3.18 mm) and comparable to the size of the individual aggregates in the mortar (up to ≈1 mm). The larger ones (3.18 mm) helped in preventing this issue, but could still be too small. This is not ideal, as the measured CTE could have been that of these aggregates and not the bulk composite.

Moreover, there are a few minor factors that could also have affected the results. Firstly, the complexity of the system could very easily originate some sort of error at some stage, be it an improper weld wire or a lose connection. External vibrations could have impacted the results in those cases.

Relative air humidity during measurements affects the CTE of mortars, from 11 ppm/K at 20% and 100% relative humidity, up to 20 ppm/K at 65% humidity [27]. The strain gauge measurements were conducted in vacuum, so this had little effect. However the dilatometric measurements were conducted with a stable air flow, and moisture could have impacted the results in some way.

Additionally, the CTE of mortar is different for different included coarse aggregate types [28, 100]. For example, 8.1 ppm/K in concrete with limestone aggregates, and 9.4 for concrete with gravel aggregates [28]. This is more relevant to concrete composites, as it includes coarser aggregates. In this work, the larger aggregate was assumed to be of a quartzite rock (from SEM and XRD analysis), which has CTEs around 10 to 14 ppm/K [94].

The dilatometry method is more simple and less complex to perform. It more accurately measures the strain of the bulk material, instead of only one surface, as is the case of the strain gauge method. However the latter is more versatile and accessible. It can be used to measure samples in cryostats capable of undergoing cryogenic temperatures, if needed. Nonetheless, the methodology detailed in this work, as well as the results obtained, may prove useful for future mortar CTE measurements.

Chapter 5

Conclusion and future work

This work is a preliminary study on creating a near zero thermal expansion (ZTE) mortar by introducing fillers with low coefficient of linear thermal expansion (CTE), to prevent microcracks induced by natural thermal cycles. Moreover, a procedure was provided to measure thermal expansion in mortars using strain gauges, that could be applied in all kinds of materials.

Characterisation methods including x-ray diffraction (XRD), scanning electron microscopy (SEM), and energy dispersive spectroscopy (EDS) were used to identify the morphology and composition of the mortars and some of the fillers. All the main phases were identified in the mortars, as well as the presence of microcracks that may have not originated from thermal cracking, but from some sort of phenomena during the curing process, such as autogenous shrinkage, or other external factors. Additionally, these microcracks were present in the interfacial transition zones (ITZs) between the larger aggregates and the cement paste, making their incorporation in finite element analysis (FEA) important to further study the influence of the mortar's microstructure on its CTE.

Analytical models, including the rule of mixtures (ROM), the Turner's model and a combined model based on the studies of Levin, Rosen and Hashim, and Schapery, were used to predict and establish bounds on the mortar's CTE, given the filler phase introduced in the composite. Complementary, FEA simulations were conducted to predict and study the influence of the amount of particles, CTE, and volume fraction of filler on the mortar's CTE. From these results, it was expected that we could achieve a ZTE mortar by adding between 6.5% (Turner model) to 23% (ROM model) LaFeSi volume fractions. Given that the measured CTE of the 3D printed mortar was high (33 ppm/K), it would be hard to achieve a ZTE composite with ZrW_2O_8 inclusions, but it can reduce the mortar's

CTE to 20 ppm/K with filler volume fractions between 9% (Turner model) to 31% (ROM model). Silica can reach similar mortar's CTE with volume fractions between 15% (Turner model) to 40% (ROM model).

Using the Taguchi method of design of experiments, it was concluded that both the amount of particles and the filler's CTE had little impact on the mortar's CTE, and decreasing both quantities leads to a greater reduction in the mortar's CTE. Increasing the amount of particles in the implemented method could also translate to decreasing their size, meaning that smaller particles do increase the mortar's CTE. However, this impact is negligible and more complex composite geometries should be implemented to further verify these results, by introducing other phases, or ITZs, for example. As expected, increasing the volume fraction of the filler dramatically contributes to reducing the mortar's CTE (assuming that the CTE of the filler is lower than that of the non-compensated mortar). In addition to introducing new phases and fillers, such as $Zn_{2-x}Mg_xP_2O_7$, different filler shapes (cubes, fibers), composite's geometries (cylindrical, parallelepiped), and randomly distributed inclusions should be simulated to further assess these results. Moreover, it could be interesting to simulate external factors, such as moisture, or the water-cement ratio, to evaluate such dependencies on the mortar's CTE.

From the stress analysis, it is clear that the mismatch between the filler and the cement paste causes irregular stress distributions in the composite, particularly high in the interfaces between phases, leading to microcracks. Therefore, including NTE fillers with very low CTEs (<-50 ppm/K) might increase the cracking problem we intend to avoid. As mortar is already a multiphase composite, these problems are already present, to a lower extent, and should be accounted for when evaluating microcracks.

As for the thermal expansion measurements, there were a few discrepancies and incoherence in the results between the strain gauge and dilatometry methods, as well as the ones predicted with the analytical models and FEA. The initial measured mortar CTE was about 33 ppm/K, which is higher than what is expected from the literature. Assuming this value, the experimental CTE results of the mortars compensated with LaFeSi and ZrW_2O_8 are within the bounds established in the analytical models, and are successful in the reduction of the mortar's CTE. The silica compensated mortars yield higher CTEs than the non-compensated mortar, which is not expected. Further non-compensated manually produced (MP) mortar strain gauge measurements contradict these previous results, as the CTE obtained was around 10 ppm/K, using two different strain gauge models, and

agree with the literature. The dilatometric measurements all yield similar results between compensated and non compensated mortars, and are around 6.5 ppm/K. These exhibited some strange dimensional relaxation phenomena.

There are a lot of factors that could have impacted the results, and it is clear that conducting these measurements in mortar is not trivial. Curing conditions, fabrication method, strain gauge adherence quality, and the complex strain gauge setup could have impacted the values in some way. The dilatometric measurements were conducted in the same samples that were subjected to systematic thermal cycling, and to extreme temperatures in some cases. It is then essential, for future measurements, that all the samples are produced at the same time, and that the curing conditions are regulated and standardised. For example, using AASHTO T 336-22, "Standard Method of Test for Coefficient of Thermal Expansion of Hydraulic Cement Concrete" [99]. The mortars should be made in the same curing conditions simultaneously, preferably using automated processes, such as 3D printing. In some cases, this could be difficult to perform at large scales, as the ammount of filler available could be too low compared to the 3D printing quantity demands, but should be possible to perform in smaller 3D printers.

In terms of applicability, at this stage in research, ZTE mortar composites may not be viable for building large scale constructions, as concrete and mortar are the most used material worldwide, and costs should remain low. NTE materials prices are orders of magnitude higher (>7 €/Kg, up to 890 €/Kg in case of ZrW_2O_8) than regular mortar bags ($\approx$ 0.12 €/Kg), meaning that the implementation of ZTEs in the construction sector is for more niche applications where thermal induced cracks are of greater concern, for example, to contain liquefied natural gas at cryogenic temperatures, where the differences from ambient temperatures might cause thermal cracking problems [101]. Nonetheless, with the scalability of this concept, and for cheaper NTE fillers, they should be possible to be implemented in infrastructure whose integrity is vital, for example in bridges or damns. Recently, in Lybia, the collapse of two damns resulted in the lost of many lives and assets, due, in part, to their degraded state, apparent from the presence of cracks and fissures [102]. In these cases, the study and introduction of ZTE concrete and mortar composites could help increasing the longevity of these infrastructures.

As was already mentioned, despite the incoherent results, the methodology discussed

and implemented could prove useful in providing a procedure to conduct thermal expansion measurements on mortars using strain gauges, that could be applied to other materials. Moreover, the results obtained shed some light to the properties and mechanical behaviour of mortars, and could help in better understanding this multiphase indispensable composite, and its applicability for ZTE applications.

Appendix A

Mortar fabrication process and samples

A.1 Fabrication process

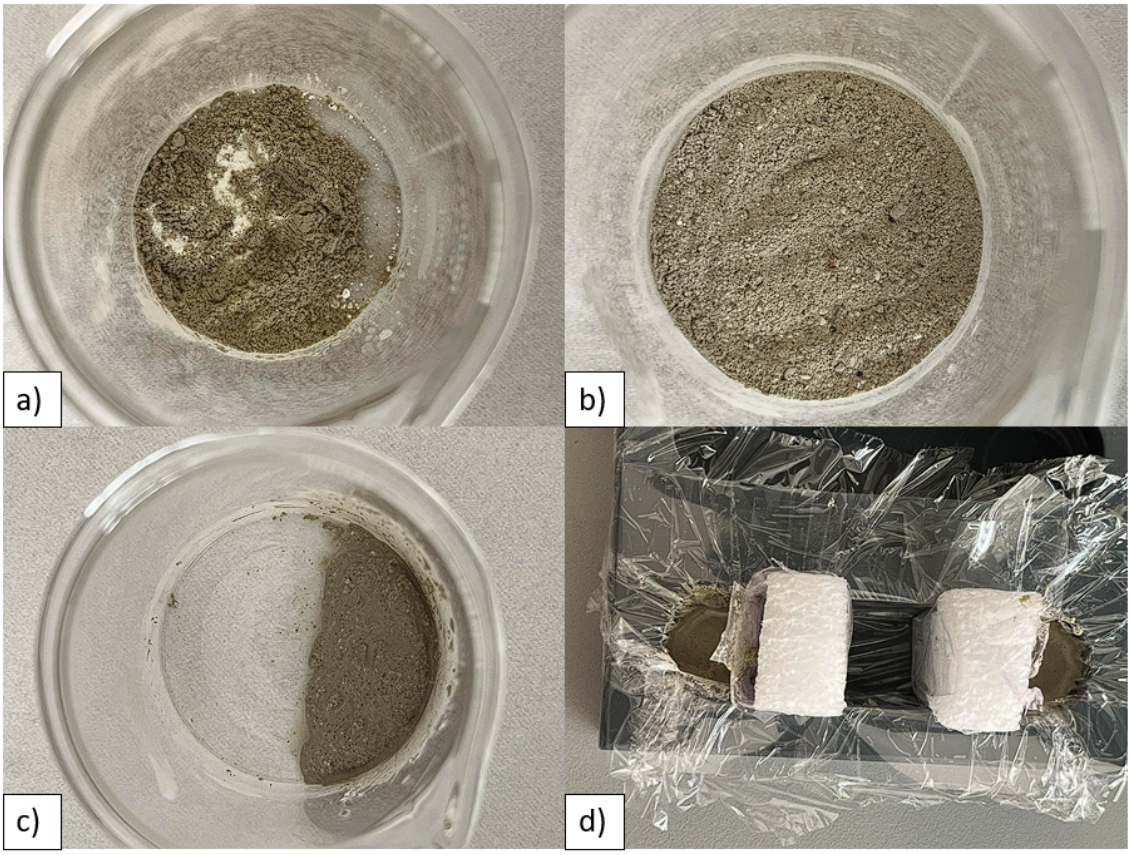


FIGURE A.1: Mortar fabrication process. a) Unmixed mortar and ZrW_2O_8 powder, b) mixed powder, c) desired mortar paste consistency after adding water, and d) mortar paste poured in the moulds, which were vibrated and tapped to release trapped air.

A.2 Fillers and manually produced samples

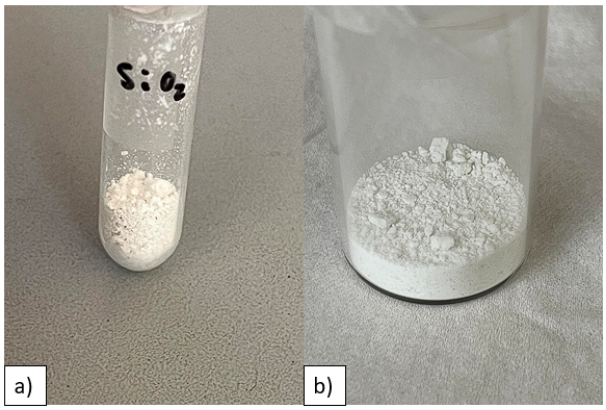


FIGURE A.2: a) SiO_2, and b) ZrW_2O_8 powder samples.

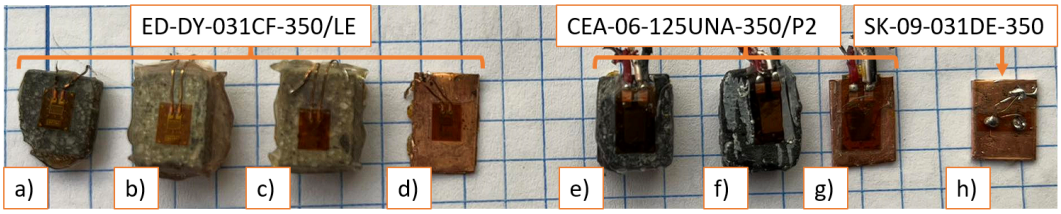


FIGURE A.3: a) Original 3D printed mortar, b) mortar + 9% silica, c) mortar + 20% silica, d) copper strip reference, e) mortar + 3.5% LaFeSi, f) mortar + 8.6% LaFeSi, and g) and h) copper strip reference. The strain gauges used in each case are also identified.

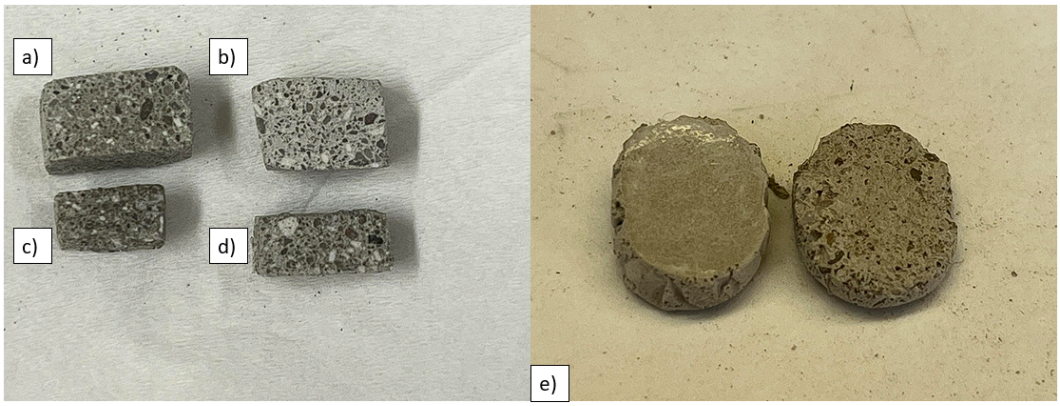


FIGURE A.4: mortars with a) 10% ZrW_2O_8 and b) 20% ZrW_2O_8 used in the strain gauge measurements, and c) and d) the ones used in dilatometry, with the same ZrW_2O_8 volume fractions, respectively. e) MP mortar samples with a superficial layer (left) and with a more representative structure (right).

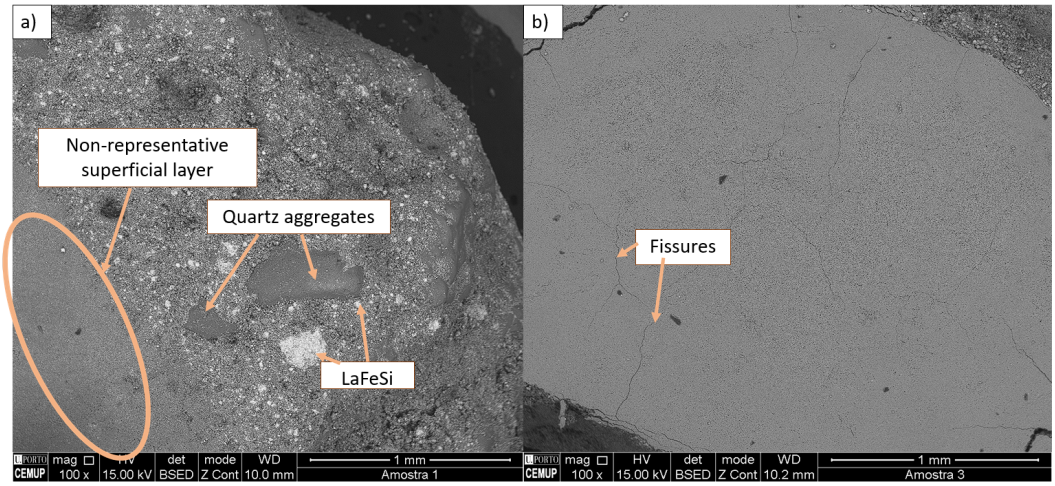


FIGURE A.5: SEM micrographs showing a) a comparison between the superficial layer and the bulk LaFeSi compensated mortar and b) superficial layer of the silica compensated mortar. Taken with magnifications of 100x (lower left corner) using BSE data.

Appendix B

Thermal expansion complementary calculations

Looking at figures 3.13 and B.1, firstly, it is important to note that the voltage between points C and D, V_{CD}, should be equal to the supplied voltage V_{in}. However, owing to internal resistance changes or changes in the environmental characteristics of the connecting wires, a slight deviation might be present. In order to have more accurate results, one could measure V_{CD} directly using a voltmeter as suggested by [103]. Nonetheless, the short wires used between voltage source and circuit made these differences negligible, so it was assumed that $V_{in} = V_{CD}$.

The relevant quantity to be measured is the potential difference between points A and B, V_{AB}. Using Kirchhoff´s current law, the total current supplied in the circuit I is equal to the sum of the currents I_1 and I_2. The voltage at each point is equal to V_{in} minus the voltage drop in the preceding resistor:

$$V_A = V_{in} - I_1 R_1 \qquad\qquad V_B = V_{in} - I_2 R_S \tag{B.1}$$

Similarly, the voltage drop between points A and D, and B and D is given by, respectively:

$$V_A - V_D = I_1 R_2 \qquad\qquad V_B - V_D = I_2 R_D \tag{B.2}$$

Given that $V_D = 0$, solving for I_1 and I_2 and plugging them into equations in B.1 gives:

$$V_A = V_{in}\frac{R_2}{R_1+R_2} \qquad V_B = V_{in}\frac{R_D}{R_S+R_D} \tag{B.3}$$

The resistances R_S and R_D will change according to equation 3.10, so we substitute R_S for $R_S + \Delta R_S$ and R_D for $R_D + \Delta R_D$ in B.3. The voltage difference between points A and B is then:

$$V_A - V_B = V_{AB} = V_{in}\frac{R_2}{R_1+R_2} - V_{in}\frac{R_D+\Delta R_D}{R_S+\Delta R_S+R_D+\Delta R_D} \tag{B.4}$$

Reducing to the same denominator and simplifying:

$$V_{AB} = V_{in}\frac{R_2R_S + R_2\Delta R_S - R_1R_D - R_1\Delta R_D}{R_2R_S + R_2R_D + R_1R_S + R_1R_D + R_1\Delta R_S + R_2\Delta R_S + R_1\Delta R_D + R_2\Delta R_D} \tag{B.5}$$

Since ΔR is very small compared to the other values, we can eliminate these factors from the denominator:

$$V_{AB} \approx V_{in}\frac{R_2R_S + R_2R_S\frac{\Delta R_S}{R_S} - R_1R_D - R_1R_D\frac{\Delta R_D}{R_D}}{R_2R_S + R_2R_D + R_1R_S + R_1R_D} \tag{B.6}$$

At bridge equilibrium (achieved by varying the rheostat resistance R_2), we have $\Delta R = 0$ and $V_A - V_B = 0$, so that $R_1R_D = R_2R_S$. Simplifying, we get:

$$V_{AB} = V_{in}\frac{R_SR_2\left(\frac{\Delta R_S}{R_S} - \frac{\Delta R_D}{R_D}\right)}{R_2R_S + R_2R_D + R_1R_S + R_1R_D} \tag{B.7}$$

We define α as:

$$\alpha = \frac{R_SR_2}{R_2R_S + R_2R_D + R_1R_S + R_1R_D} \tag{B.8}$$

Assuming that $R_D = R_S$ and using equation 3.10 we get:

$$V_{AB} = V_{in}\alpha\frac{\Delta R_{S,\,sample} + \Delta R_{S,\,strain\,gauge} - \Delta R_{D,\,sample} - \Delta R_{D,\,strain\,gauge}}{R_S} \tag{B.9}$$

Using equation 3.9, and assuming that $\Delta R_{D,T} = \Delta R_{S,T}$, we finally get the strain:

$$\epsilon_S = \frac{V_{AB}}{V_{in}\alpha GF} + \epsilon_D \tag{B.10}$$

The reference material used was copper and the strain data, ϵ_D, was taken from the National Institute of Standards and Technology (NIST) [104]. With this data and the measured V_{AB} and temperature, T, we can obtain the CTE of the sample by finding the slope of ϵ_S Vs T, corresponding to equation 2.5.

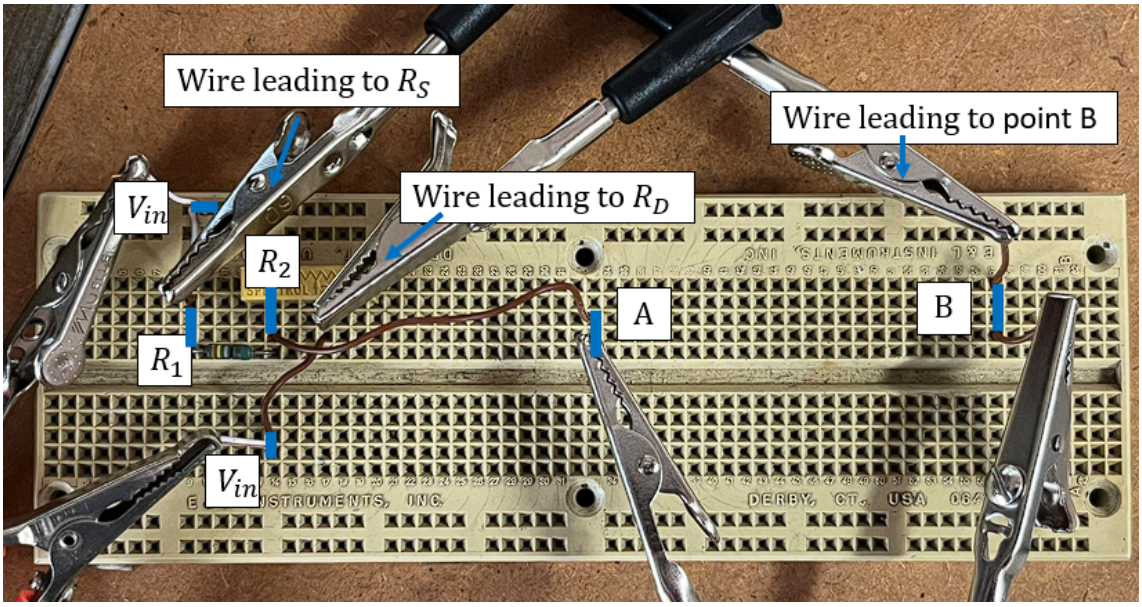


FIGURE B.1: Implemented Wheatstone bridge circuit. Blue lines represent connections between wires. See figure 3.13 for comparison.

Appendix C

EDS data examples

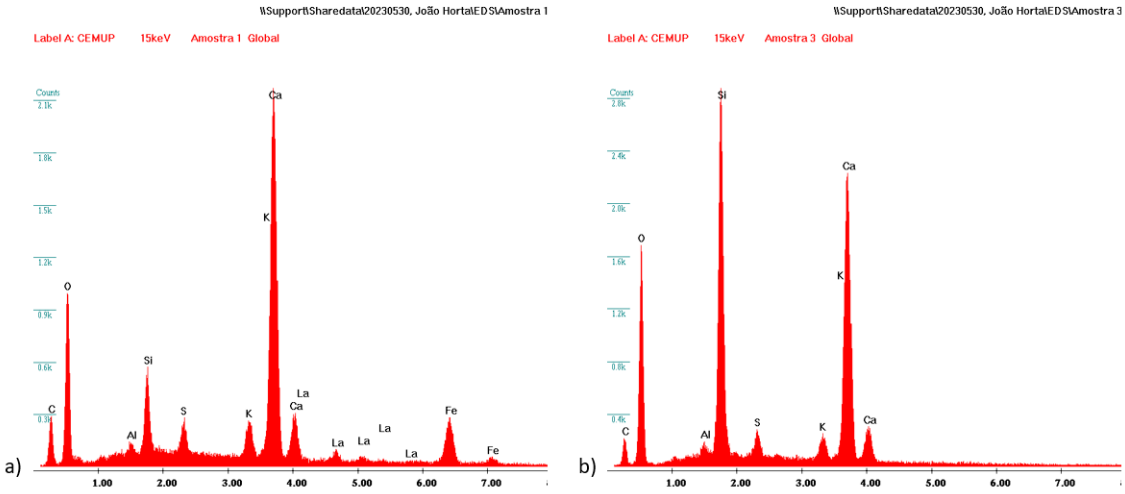


FIGURE C.1: EDS of a) LaFeSi compensated mortar and b) silica compensated mortar. In both cases we can see the presence of the elements found in clinker (Ca, Si, O, Al) and in gypsum (S), and in the case of the LaFeSi, the presence of La and Fe. As expected, the silica compensated mortar has and increased amount of O and Si.

Appendix D

Thermal expansion measurements additional information

D.1 Temperature lag between thermocouple readings and actual sample temperature

To verify the presence of a lag between thermocouple readings and actual sample temperature, a study was conducted where the temperature was increased in 10K steps with a 2 K/min heating rate and a 10 min stabilisation time between steps.

In some measurements of one of the silica compensated mortars, there was a noticeable lag between the thermocouple reading and the actual sample temperature. This is evident by the red spiral curve in figure D.1, where the strain measurements do not exhibit a somewhat linear dependence with temperature. The expected behaviour would be the one obtained by the blue line in one of the MP mortar measurements, where the same procedure was conducted.

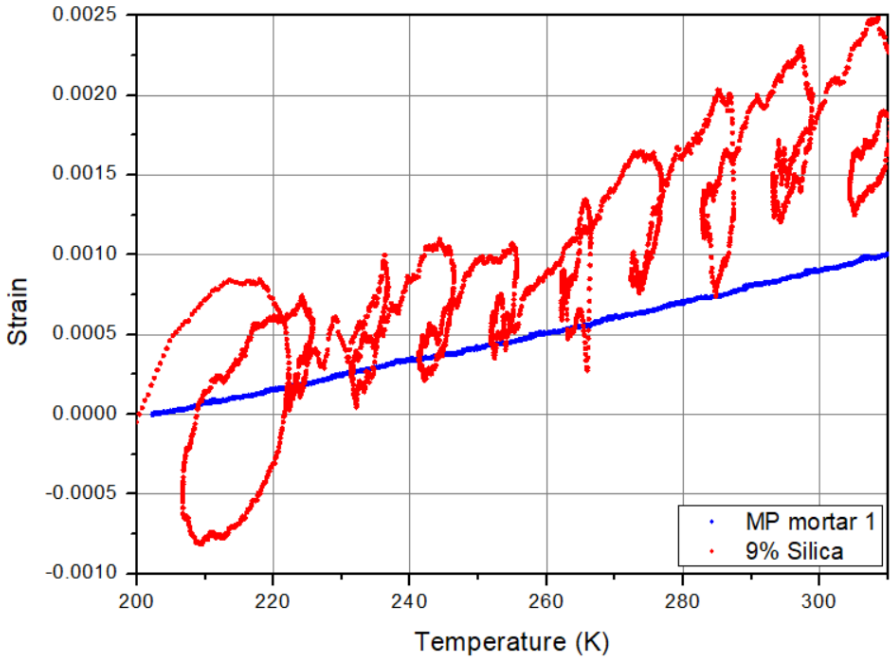


FIGURE D.1: Temperature lag between thermocouple readings and actual sample temperature for different samples. The temperature was increased in 10K steps with a 2 K/min heating rate and a 10 min stabilisation time between steps.

D.2 Dilatometry additional data

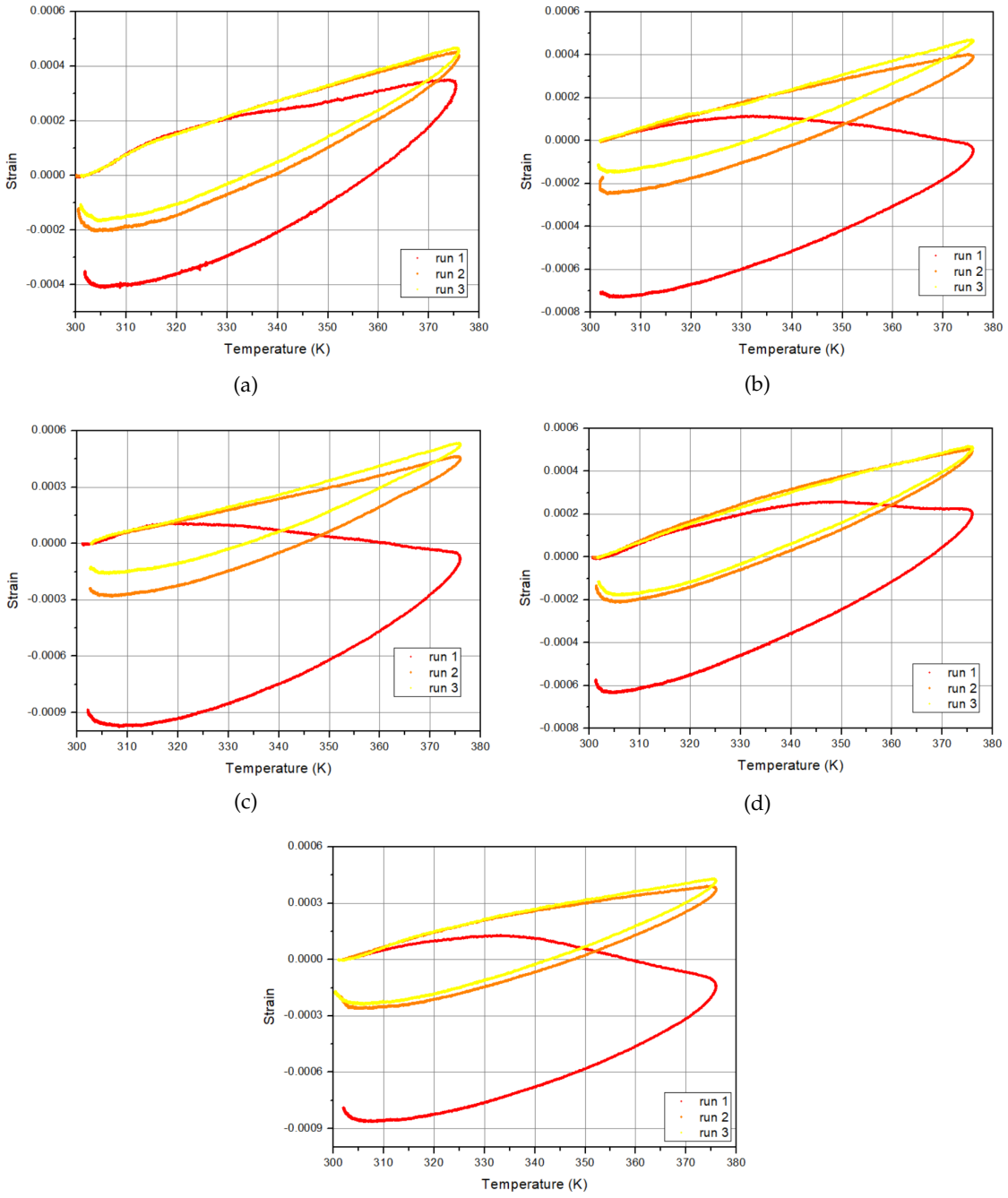


FIGURE D.2: Dilatometric CTE measurements for a) the initial 3D printed mortar, b) 3.5% LaFeSi compensated mortar, c) 8.6% LaFeSi compensated mortar, d) 9% SiO_2 compensated mortar, and e) MP mortar, with 1 K/min heating rate.

Bibliography

[1] P. K. Mehta and P. J. M. Monteiro, *Concrete: Microstructure, Properties, and Materials*. McGraw-Hill Education, 2014. [Cited on pages 1, 5, 6, 7, and 59.]

[2] H. Nakamura, T. Nanri, T. Miura, and S. Roy, "Experimental investigation of compressive strength and compressive fracture energy of longitudinally cracked concrete," *Cement and Concrete Composites*, vol. 93, pp. 1–18, 2018. [Cited on page 1.]

[3] N. S. Leitão and E. Castilho, "Heat transfer analysis of infrastructures subjected to environmental actions: A finite element solver pat," *Thermal Science and Engineering Progress*, vol. 34, 2022. [Cited on page 1.]

[4] N. Tamrakar, "Overview on causes of flexible pavement distresses," *Bulletin of Nepal Geological Society*, 2019.

[5] P. Gudipudi, S. Underwood, and A. Zalghout, "Impact of climate change on pavement structural performance in the united states," *Transportation Research Part D Transport and Environment*, vol. 57, pp. 172–184, 2017. [Cited on page 1.]

[6] R. Malm, R. Hellgren, and J. Enzell, "Lessons learned regarding cracking of a concrete arch dam due to seasonal temperature variations," *Infrastructures*, vol. 5, no. 2, 2020. [Cited on page 1.]

[7] J.-S. Fan, Y.-F. Liu, and C. Liu, "Experiment study and refined modeling of temperature field of steel-concrete composite beam bridges," *Engineering Structures*, vol. 240, 2021. [Cited on page 1.]

[8] The Burj Al-Arab. [Online]. Available: https://www.e-nsight.com/en/2020/11/17/the-burj-al-arab/ [Cited on page 2.]

[9] K. Takenaka, "Progress of research in negative thermal expansion materials: Paradigm shift in the control of thermal expansion," *Frontiers in Chemistry*, vol. 6, 2018. [Cited on pages 2, 8, 10, 11, and 12.]

[10] J. P. Attfield, "Mechanisms and materials for nte," *Frontiers in Chemistry*, vol. 6, no. 371, 2018. [Cited on pages 8, 10, and 12.]

[11] G. D. Barrera, J. A. O. Bruno, T. H. K. Barron, and N. L. Allan, "Negative thermal expansion," *Journal of Physics: Condensed Matter*, vol. 17, no. 4, 2005. [Cited on pages 11 and 12.]

[12] W. Miller, C. W. Smith, D. S. Mackenzie, and K. E. Evans, "Negative thermal expansion: a review," *Journal of Materials Science*, vol. 44, 2009. [Cited on pages 2, 8, 10, 11, and 12.]

[13] M. Kofteros, S. Rodriguez, V. Tandon, and L. Murr, "A preliminary study of thermal expansion compensation in cement by zrw2o8 additions," *Scripta Materialia*, vol. 45, no. 4, 2001. [Cited on pages 2, 15, and 47.]

[14] J. Ouyang, Y. Li, B. Chen, and D. Huang, "Macro-scale strength and microstructure of zrw2o8 cementitious composites with tunable low thermal expansion," *Materials*, vol. 11, no. 5, 2018. [Cited on pages 15 and 26.]

[15] V. P. Veedu, A. Kumar, and S. Thapa, "High temperature composites and their application," 2017, uS Patent 9,845,264. [Cited on page 2.]

[16] C. Harty, "Implementing innovation in construction: Contexts, relative boundedness and actor-network theory," *Construction Management & Economics*, vol. 26, pp. 1029–1041, 2008. [Cited on page 3.]

[17] J. de Brito and R. Kurda, "The past and future of sustainable concrete: A critical review and new strategies on cement-based materials," *Journal of Cleaner Production*, vol. 281, 2021. [Cited on page 3.]

[18] A. Mukherjee, Deepmala, P. Srivastava, and J. K. Sandhu, "Application of smart materials in civil engineering: A review," *Materials Today: Proceedings*, vol. 81, pp. 350–359, 2023. [Cited on page 3.]

[19] X. Xu, D. Cao, H. Yang, and M. He, "Application of piezoelectric transducer in energy harvesting in pavement," *International Journal of Pavement Research and Technology*, vol. 11, no. 4, pp. 388–395, 2018. [Cited on page 3.]

[20] R. Robayo-Salazar, R. Mejía de Gutiérrez, M. A. Villaquirán-Caicedo, and S. Delvasto Arjona, "3d printing with cementitious materials: Challenges and opportunities for the construction sector," *Automation in Construction*, vol. 146, 2023. [Cited on page 4.]

[21] S. Pessoa, A. Guimarães, S. Lucas, and N. Simões, "3d printing in the construction industry - a systematic review of the thermal performance in buildings," *Renewable and Sustainable Energy Reviews*, vol. 141, 2021.

[22] S. C. Paul, Y. W. D. Tay, B. Panda, and M. J. Tan, "Fresh and hardened properties of 3d printable cementitious materials for building and construction," *Archives of Civil and Mechanical Engineering*, vol. 18, no. 1, pp. 311–319, 2018. [Cited on page 4.]

[23] J. Radić, A. Kindij, and A. Mandić Ivanković, "History of concrete application in development of concrete and hybrid arch bridges," *Proc. of The Chinese-Croatian Joint Colloquium on Long Arch Bridges*, 2008. [Cited on page 6.]

[24] P. C. Aïtcin, "3 - portland cement," in *Science and Technology of Concrete Admixtures*, P.-C. Aïtcin and R. J. Flatt, Eds. Woodhead Publishing, 2016. [Cited on page 6.]

[25] N. Winter, *Understanding Cement: An Introduction to Cement Production, Cement Hydration and Deleterious Processes in Concrete*. Microanalysis Consultants, 2012. [Cited on pages 6 and 13.]

[26] Q. Zeng, K. Li, T. Fen-Chong, and P. Dangla, "Effect of porosity on thermal expansion coefficient of cement pastes and mortars," *Construction and Building Materials - CONSTR BUILD MATER*, vol. 28, 2012. [Cited on pages 7 and 59.]

[27] S. Yang, N. Kim, J. Kim, and J. Park, "Experimental measurement of concrete thermal expansion," *Journal of the Eastern Asia Society for Transportation Studies*, vol. 5, 2003. [Cited on pages 59 and 61.]

[28] U. J. Ndon and K. L. Bergeson, "Thermal expansion of concretes: Case study in iowa," *Journal of Materials in Civil Engineering*, vol. 7, no. 4, pp. 246–251, 1995. [Cited on pages 7 and 61.]

[29] J. Ollivier, J. Maso, and B. Bourdette, "Interfacial transition zone in concrete," *Advanced Cement Based Materials*, vol. 2, no. 1, pp. 30–38, 1995. [Cited on pages 7 and 18.]

[30] C. Lynam, *Growth and Movement in Portland Cement Concrete*. Oxford University Press, 1934. [Cited on page 7.]

[31] G. Bertagnoli, D. Gino, and E. Martinelli, "A simplified method for predicting early-age stresses in slabs of steel-concrete composite beams in partial interaction," *Engineering Structures*, vol. 140, pp. 286–297, 2017. [Cited on page 7.]

[32] K. Takenaka, "Negative thermal expansion materials: technological key for control of thermal expansion," *Science and Technology of Advanced Materials*, vol. 13, no. 1, 2012. [Cited on pages 8, 12, and 15.]

[33] M. T. Dove and H. Fang, "Negative thermal expansion and associated anomalous physical properties: review of the lattice dynamics theoretical foundation," *Reports on Progress in Physics*, vol. 79, no. 6, 2016. [Cited on pages 8, 10, and 11.]

[34] J. S. O. Evans, "Negative thermal expansion materials," *J. Chem. Soc., Dalton Trans.*, 1999. [Cited on pages 9, 10, 12, and 15.]

[35] J. Grima, V. Zammit, and R. Gatt, "Negative thermal expansion," *Xjenza*, vol. 11, 2006. [Cited on pages 8 and 12.]

[36] C. Lind, "Two decades of negative thermal expansion research: Where do we stand?" *Materials (Basel)*, vol. 5, no. 6, 2012. [Cited on pages 10 and 11.]

[37] R. O. Fleming, S. Gonçalves, A. Davarpanah, I. Radulov, L. Pfeuffer, B. Beckmann, K. Skokov, Y. Ren, T. Li, J. Evans, J. Amaral, R. Almeida, A. Lopes, G. Oliveira, J. P. Araújo, A. Apolinário, and J. H. Belo, "Tailoring negative thermal expansion via tunable induced strain in la–fe–si-based multifunctional material," *ACS Applied Materials & Interfaces*, vol. 14, no. 38, 2022. [Cited on pages 12, 14, 21, 24, 31, 44, and 46.]

[38] J. Chen, L. Hu, J. Deng, and X. Xing, "Negative thermal expansion in functional materials: controllable thermal expansion by chemical modifications," *Chem. Soc. Rev.*, vol. 44, pp. 3522–3567, 2015. [Cited on page 12.]

[39] J. a. H. Belo, A. L. Pires, I. T. Gomes, V. Andrade, J. a. B. Sousa, R. L. Hadimani, D. C. Jiles, Y. Ren, X. Zhang, J. a. P. Araújo, and A. M. Pereira, "Giant negative thermal expansion at the nanoscale in the multifunctional material $Gd_5(Si, Ge)_4$," *Phys. Rev. B*, vol. 100, 2019. [Cited on page 12.]

[40] W.-H. Li, S. Y. Wu, C. C. Yang, S. K. Lai, K. C. Lee, H. L. Huang, and H. D. Yang, "Thermal contraction of au nanoparticles," *Phys. Rev. Lett.*, vol. 89, no. 4, 2002. [Cited on page 12.]

[41] 'Sinoenergy'. [Online]. Available: http://www.sinosilica.com/eng/ [Cited on pages 13 and 16.]

[42] P. Dittanet and R. Pearson, "Effect of silica nanoparticle size on toughening mechanisms of filled epoxy," *Polymer*, vol. 53, no. 9, 2012. [Cited on page 13.]

[43] K. Shaker, Y. Nawab, A. Saouab, M. Ashraf, and A. N. Khan, "Effect of silica particle loading on shape distortion in glass/vinyl ester-laminated composite plates," *The Journal of The Textile Institute*, vol. 109, no. 5, 2018. [Cited on page 13.]

[44] B. Deng, Y. Shi, and F. Yuan, "Investigation on the structural origin of low thermal expansion coefficient of fused silica," *Materialia*, vol. 12, 2020. [Cited on page 13.]

[45] R.-S. Lin, X.-Y. Wang, and G.-Y. Zhang, "Effects of quartz powder on the microstructure and key properties of cement paste," *Sustainability*, vol. 10, no. 10, 2018. [Cited on page 13.]

[46] M. H. Zhang, S. Swaddiwudhipong, K. Y. Tay, and C. T. Tam, "Effect of silica fume on cement hydration and temperature rise of concrete in tropical environment," *The IES Journal Part A: Civil & Structural Engineering*, vol. 1, no. 2, 2008. [Cited on page 13.]

[47] F. Sanchez and K. Sobolev, "Nanotechnology in concrete – a review," *Construction and Building Materials*, vol. 24, no. 11, 2010.

[48] S. Abd.El.Aleem, M. Heikal, and W. Morsi, "Hydration characteristic, thermal expansion and microstructure of cement containing nano-silica," *Construction and Building Materials*, vol. 59, pp. 151–160, 2014. [Cited on page 13.]

[49] Y. Song, N. Shi, S. Deng, X. Xing, and J. Chen, "Negative thermal expansion in magnetic materials," *Progress in Materials Science*, vol. 121, 2021. [Cited on page 14.]

[50] H. Zhou, Y. Liu, R. Huang, B. Chen, M. Xia, Z. Yu, H. Chen, K. Qiao, J. Cong, S. Taskaev, K. Chu, and H. Zhang, "Tunable negative thermal expansion in la(fe, si)13/resin composites with high mechanical property and long-term cycle stability," *Microstructures*, vol. 121, 2022. [Cited on page 14.]

[51] T. A. Mary, J. S. O. Evans, T. Vogt, and A. W. Sleight, "Negative thermal expansion from 0.3 to 1050 kelvin in zrw_2o_8," *Science*, vol. 272, no. 5258, 1996. [Cited on page 15.]

[52] A. K. A. Pryde, M. T. Dove, and V. Heine, "Simulation studies of at high pressure," *Journal of Physics: Condensed Matter*, vol. 10, no. 38, 1998. [Cited on page 15.]

[53] Y. Kadowaki, R. Kasugai, Y. Yokoyama, N. Katayama, Y. Okamoto, and K. Takenaka, "Structural phase transition and giant negative thermal expansion in pyrophosphate Zn2–xMgxP2O7," *Applied Physics Letters*, vol. 119, no. 20, p. 201906, 2021. [Cited on pages 15 and 16.]

[54] R. Kasugai, Y. Kadowaki, Y. Yokoyama, N. Katayama, Y. Okamoto, and K. Takenaka, "Systematic Study on the Role of the Third Zn-Site Element in Zn2–xMgxP2O7 Showing Giant Negative Thermal Expansion," *MATERIALS TRANSACTIONS*, vol. 64, no. 3, pp. 638–642, 2023. [Cited on pages 15 and 16.]

[55] "Cement prices in the united states from 2010 to 2022 (in u.s. dollars per metric ton)." [Online]. Available: https://www.statista.com/statistics/219339/us-prices-of-cement/ [Cited on page 16.]

[56] S. L. Russek and C. B. Zimm, "Potential for cost effective magnetocaloric air conditioning systems," *International Journal of Refrigeration*, vol. 29, no. 8, pp. 1366–1373, 2006. [Cited on page 16.]

[57] C. Karch, "Micromechanical analysis of thermal expansion coefficients," *Modeling and Numerical Simulation of Material Science*, vol. 4, 2014. [Cited on page 17.]

[58] W. Voigt, "Ueber die beziehung zwischen den beiden elasticitätsconstanten isotroper körper," *Annalen der Physik*, vol. 38, 1889. [Cited on page 17.]

[59] A. Reuß, "Berechnung der fließgrenze von mischkristallen auf grund der plastizitätsbedingung für einkristalle." *Zamm-zeitschrift Fur Angewandte Mathematik Und Mechanik*, vol. 9, pp. 49–58, 1929. [Cited on page 17.]

[60] P. S. Turner, "Thermal-expansion stresses in reinforced plastics," *Journal of research of the National Bureau of Standards*, vol. 37, 1946. [Cited on page 17.]

[61] V. Levin, "Thermal expansion coefficients of heterogeneous materials," *Mechanics of Solids*, vol. 2, pp. 58–61, 1967. [Cited on page 17.]

[62] B. Rosen and Z. Hashin, "Effective thermal expansion coefficients and specific heats of composite materials," *International Journal of Engineering Science*, vol. 8, no. 2, pp. 157–173, 1970. [Cited on page 17.]

[63] R. Schapery, "Thermal expansion coefficients of composite materials based on energy principles," *Journal of Composite Materials*, vol. 2, no. 3, 1968. [Cited on page 17.]

[64] Z. Hashin and S. Shtrikman, "A variational approach to the theory of the elastic behaviour of multiphase materials," *Journal of Mechanics Physics of Solids*, vol. 11, no. 2, pp. 127–140, 1963. [Cited on page 18.]

[65] J. N. Reddy, *Introduction to the finite element method*. McGraw-Hill Education, 2019. [Cited on page 18.]

[66] C. Sun and R. Vaidya, "Prediction of composite properties from a representative volume element," *Composites Science and Technology*, vol. 56, no. 2, pp. 171–179, 1996. [Cited on page 18.]

[67] *COMSOL Multiphysics® v. 6.1*, COMSOL. AB, Stockholm, Sweden. [Online]. Available: https://www.comsol.com/ [Cited on page 19.]

[68] G. J. Tilton, "Finite element modeling of thermal expansion in polymer / zrw2o8 composites," Master's thesis, University of Toledo, 2018. [Cited on pages 19, 20, and 21.]

[69] F. Belabdelouahab, H. Trouzine, H. Hellal *et al.*, "Comparative analysis of estimated young's modulus of rubberized mortar and concrete," *Int J Civ Eng*, vol. 16, 2018. [Cited on page 21.]

[70] Silica properties. [Online]. Available: https://www.azom.com/article.aspx?ArticleID=1114 [Cited on page 21.]

[71] O. Glushko, A. Funk, V. Maier-Kiener, P. Kraker, M. Krautz, J. Eckert, and A. Waske, "Mechanical properties of the magnetocaloric intermetallic lafe11.2si1.8 alloy at different length scales," *Acta Materialia*, vol. 165, 2018. [Cited on page 21.]

[72] T. M. Project, "Materials data on lafesi by materials project," *United States: N. p.*, 2020. [Cited on page 21.]

[73] A. Pérez González, J. L. Iserte Vilar, and C. González Lluch, "Interpreting finite element results for brittle materials in endodontic restorations," *Biomedical engineering online*, vol. 10, 2011. [Cited on page 23.]

[74] R. Roy, *A Primer on the Taguchi Method*. Society of Manufacturing Engineers, 1990. [Cited on page 23.]

[75] Weber 3d 160-1 datasheet. [Online]. Available: https://www.3d.weber/materials/ [Cited on pages 26 and 40.]

[76] M. Lee, "X-ray diffraction for materials research: From fundamentals to applications (1st ed.)," *Apple Academic Press and CRC Press*, 2016. [Cited on page 27.]

[77] Britannica, T. Editors of Encyclopaedia, "Bragg law," *Encyclopedia Britannica*, 2022. [Cited on page 27.]

[78] Rigaku Corporation and its Global Subsidiaries. [Online]. Available: https://www.rigakuedxrf.com/?gclid=EAIaIQobChMIqWK16DBgQMVlFBBAh3hzwkLEAAYASAAEgIdnPD_BwE [Cited on page 28.]

[79] R. Schmitt, *Scanning Electron Microscope*. Springer Berlin Heidelberg, 2014. [Cited on page 29.]

[80] Looking at materials up close - The Scanning Electron Microscope. [Online]. Available: https://www.rrutc.msm.cam.ac.uk/outreach/articles/the-scanning-electron-microscope [Cited on page 29.]

[81] M.-M. V. P. Group. (2016) Precision strain gages and sensors - databook. [Online]. Available: https://micro-measurements.com/resources/knowledge-base/databooks [Cited on page 33.]

[82] I. V. b. 'Micro-Measurements, a Vishay Precision Group. [Online]. Available: https://www.micro-measurements.com/products [Cited on page 34.]

[83] ADVANCED RESEARCH SYSTEMS. [Online]. Available: https://www.arscryo.com/cryocooler-principles-of-operation [Cited on pages 35 and 36.]

[84] W. E. Gifford, "The gifford-mcmahon cycle," in *Advances in Cryogenic Engineering*, K. D. Timmerhaus, Ed. Springer US, 1966, pp. 152–159. [Cited on page 35.]

[85] *User's Manual Model 331 Temperature Controller*, Lake Shore Cryotronics, Inc., Westerville, Ohio. [Cited on page 36.]

[86] M. Hunkel, H. Surm, and M. Steinbacher, "Chapter 3 - dilatometry," in *Recent Advances, Techniques and Applications*, S. Vyazovkin, N. Koga, and C. Schick, Eds. Elsevier Science B.V., 2018. [Cited on page 37.]

[87] S. Kanagaraj and S. Pattanayak, "Measurement of the thermal expansion of metal and frps," *Cryogenics*, vol. 43, no. 7, pp. 399–424, 2003. [Cited on page 38.]

[88] O. L. Baumfeld, Z. Gercsi, M. Krautz, O. Gutfleisch, and K. G. Sandeman, "The dynamics of spontaneous hydrogen segregation in LaFe13-xSixHy," *Journal of Applied Physics*, vol. 115, no. 20, 2014. [Cited on page 44.]

[89] S. Yang and H. Lee, "Coefficient of thermal expansion of rca concrete made by equivalent mortar volume," *Applied Sciences*, vol. 11, no. 17, 2021. [Cited on pages 52 and 60.]

[90] E. Sellevold and O. Bjontegaard, "Coefficient of thermal expansion of cement paste and concrete: Mechanisms of moisture interaction," *Materials and Structures*, vol. 39, 2006.

[91] W. Feng, Y. Li, Q. Yuan, Z. Xie, G. Ding, and C. Ji, "Measurement and analysis of thermal expansion coefficients of mortar and limestone cooled to cryogenic temperatures," *Journal of Physics: Conference Series*, vol. 1549, no. 3, 2020. [Cited on pages 52 and 60.]

[92] D. Cusson and T. Hoogeveen, "New test method for determining coefficient of thermal expansion of high-performance concrete at early age," *National Research Council Canada*, vol. 98, pp. 14–28, 2023. [Cited on page 53.]

[93] S. N. Shoukry, G. W. William, B. Downie, and M. Y. Riad, "Effect of moisture and temperature on the mechanical properties of concrete," *Construction and Building Materials*, vol. 25, no. 2, pp. 688–696, 2011. [Cited on page 53.]

[94] Portland Cement Concrete Pavements Research. [Online]. Available: https://www.fhwa.dot.gov/publications/research/infrastructure/pavements/pccp/thermal.cfm [Cited on pages 53 and 61.]

[95] L. Dahmani, A. Khenane, and S. Kaci, "Behavior of the reinforced concrete at cryogenic temperatures," *Cryogenics*, vol. 47, no. 9, pp. 517–525, 2007. [Cited on pages 58 and 60.]

[96] E. Sicat, F. Gong, D. Zhang, and T. Ueda, "Change of the coefficient of thermal expansion of mortar due to damage by freeze thaw cycles," *Journal of Advanced Concrete Technology*, vol. 11, no. 12, pp. 333–346, 2013. [Cited on page 60.]

[97] R. Helmuth, *Dimensional Changes of Hardened Portland Cement Pastes Caused by Temperature Changes*, ser. Bulletin (Portland Cement Association. Research and Development Laboratories. Research Department). Highway Research Board, 1961, vol. 40. [Cited on page 60.]

[98] X. Fu and D. D. L. Chung, "Effect of admixtures on thermal and thermomechanical behavior of cement paste," *ACI Materials Journal*, vol. 96, 1999. [Cited on page 60.]

[99] "AASHTO T 336, Standard Method of Test for Coefficient of Thermal Expansion of Hydraulic Cement Concrete," 2022. [Cited on pages 60 and 65.]

[100] C. R. Cruz and M. Gillen, "Thermal expansion of portland cement paste, mortar and concrete at high temperatures," *Fire and Materials*, vol. 4, no. 2, pp. 66–70, 1980. [Cited on page 61.]

[101] R. B. Kogbara, S. R. Iyengar, Z. C. Grasley, E. A. Masad, and D. G. Zollinger, "A review of concrete properties at cryogenic temperatures: Towards direct lng containment," *Construction and Building Materials*, vol. 47, pp. 760–770, 2013. [Cited on page 65.]

[102] S. MAGDY, "Libya was mired in chaos and corruption. for years, warnings the derna dams may burst went unheeded," *Associated Press*, 2023. [Online]. Available: https://apnews.com/article/libya-derna-dams-collapse-floods-corruption-neglect-chaos-45f76d2ac76be634865539a27b518adahttps://apnews.com/article/libya-derna-dams-collapse-floods-corruption-neglect-chaos-45f76d2ac76be634865539a27b518ada [Cited on page 65.]

[103] M. Ohashi *et al.*, "New bridge-circuit-type detector to measure precise resistance change of strain gauge at low temperature and magnetic field," *Jpn. J. Appl. Phys.*, vol. 55, no. 4, 2016. [Cited on page 71.]

[104] F. C. Nix and D. MacNair, "The thermal expansion of pure metals: Copper, gold, aluminum, nickel, and iron," *Phys. Rev.*, vol. 60, pp. 597–605, 1941. [Cited on page 73.]